Leaflet dependent localization and diffusion of molecules within membranes using metal-induced energy transfer

Akshita Sharma

Leaflet-resolved localization and diffusion of molecules within membranes using metal-induced energy transfer

Dissertation

for the award of the degree

"Doctor rerum naturalium"

of the Georg-August-Universität Göttingen

within the doctoral program

Physics of Biological and Complex Systems

of the Göttingen Graduate School

of Neurosciences, Biophysics,

and Molecular Biosciences (GGNB)

of the Georg August University School of Science (GAUSS)

submitted by

Akshita Sharma

from Delhi, India

Göttingen 2021

30.06.2021

Members of the Examination Board:

Prof. Dr. Jörg Enderlein (Reviewer)

Third Institute of Physics - Biophysics, Faculty of Physics,

Georg August University Göttingen

Prof. Dr. Claudia Steinem (Reviewer)

Institute for Organic and Biomolecular Chemistry

Max Planck Institute for Dynamics and Self-Organization

Prof. Dr. Marcus Müller

Institute for Theoretical Physics

Georg August University Göttingen

Prof. Bert de Groot

Max Planck Institute for Biophysical Chemistry

Dr. Sebastian Kruss

Institute for Physical Chemistry

Georg August University Göttingen

Prof. Dr. Ralph Kehlenbach

Department of Molecular Biology

University Medical Center, Göttingen

Affidavit

Hereby, I declare that the presented thesis has been written independently and with no other sources and aids than quoted. The parts of this dissertation and some figures have been published in the articles listed below.

List of related publications:

Arindam Ghosh, **Akshita Sharma**, Alexey I Chizhik, Sebastian Isbaner, Daja Ruhlandt, Roman Tsukanov, Ingo Gregor, Narain Karedla, and Jörg Enderlein. Graphene-based metal-induced energy transfer for sub-nanometre optical localization. *Nature Photonics*, 13(12):860865, 2019.

Martin Kloos, **Akshita Sharma**, Jörg Enderlein and Ulf Diederichsen. Transmembrane β-peptide helices as molecular rulers at the membrane surface. *Journal of Peptide Science*, e3355, 2021.

Göttingen, 30.06.2021

Acknowledgement

This work is carried out at III Institute of Biophysics., University of Göttingen, Germany during years 2017-2021. These years might have been the most demanding, frustrating and stressful of my life but at the same time, these years have been the most rewarding exciting and unforgettable. During this journey, I have met a lot of great people, who I want to express my sincere gratitude.

First and foremost, I want to express my deepest gratitude to my supervisor, Professor Jörg Enderlein, for the opportunity to work in his group and introducing me into the exciting world of advanced microscopy. This thesis would not have been possible without the tremendous support and motivation in all possible ways from Jörg Enderlein. I thank him for supervising my doctoral thesis, for exposing me to a multitude of projects and ideas, believed in me and gave me the freedom at work which immensely helped in my development as a researcher.

I am also grateful to Professor Claudia Steinem and Professor Marcus Müller for all the guidance and encouragement throughout these years. I sincerely thank them for their input and support whenever I required, and taking their precious time out to regularly monitor and discuss the progress of my work.

Professor Ulf Diederichsen and Professor Daniel B. Werz are warmly thanked for the collaboration projects during my thesis work.

I would like to thank Dr. Ingo Gregor for constantly providing me with his invaluable experience for all the experiments presented in this thesis. I would specially like to thank Narain for helping me build concepts, technical knowledge and giving his valuable suggestions. More than that his motivation that helped me even through stressful times. Many thanks to all my colleagues, former and present, for all the fruitful discussions and technical support, especially Sebastian and Arindam for the endless patience and valuable suggestions in work. I have learnt from all of them, immensely. I would also like to thank my office mates Nazar and Hongje for the fun memories of the office. I am highly grateful to all the secretaries for managing and handling the official paperwork for every conference trip, also guiding me through the official processes during my stay in Germany.

I acknowledge the financial support from SFB 803 (DFG) and also from GGNB bridging fund.
I thank all my friends including Narain, Praveen, and Dwayne, not only for making my stay in Göttingen memorable and fun, but they, more than anything, were the main reason for my sanity, especially during my writing days. Last but not the least, I am grateful to my parents for all their love, moral support, sacrifices all along the way, and for being the light and guide in my life.

“ Three things cannot be long hidden: the sun, the moon, and the truth "

Buddha

To my parents

Rajni Sharma and Adesh Kumar Sharma

Abstract

Diffusion is the most fundamental process of molecular transport in cell membranes and an important factor in maintaining its fluidity, controlling the dynamics and functioning of the membrane. In-depth knowledge of membrane dynamics and its structure is essential for understanding the functional role of membranes and all processes involving them. Therefore, a precise quantitative characterisation of diffusion in membranes is important. While Many different techniques have given insight into this matter, but they fail in addressing the dual-leaflet nature of a membrane. The experimental challenge is the extremely small distance of $\sim$5 nm between the leaflets which is by two orders of magnitude smaller than the diffraction-limited optical resolution of a microscope (ca. 500 nm along the optical axis, for a well-adjusted confocal microscope). In this thesis, I present a new method of super-resolution microscopy that allows me to distinguish between individual leaflets of a Supported lipid bilayer (SLB) and to measure axial distances with nanometer accuracy.

Moreover, it allows me to measure the diffusion of lipids in an SLB with a leaflet-resolved manner. Such SLBs serve as simple model systems to study membrane dynamics, and our method will allow me to see interaction between the leaflets and the effect of an SLBs proximity to the substrate. For this purpose, I combine Metal-induced energy transfer (MIET) with scanning Fluorescence Lifetime Correlation Spectroscopy (sFLCS). MIET exploits the strongly distance-dependent quenching of a fluorophores by a nearby metal(or graphene) layer. On replacing the metal layer with a single sheet of graphene, the axial resolution of this method can be pushed down to sub-nanometers, due to the much more localized quenching of fluorescence by graphene. This thesis will mainly focus on MIET/GIET and its application to studying membranes. In combination with FLCS, I am able to determine leaflet-specific diffusion coefficients. A major part of this thesis involves leaflet-resolved diffusion studies on model SLBs.

Contents

CHAPTER 1

Introduction

Biological membranes are complex systems which do not only separate the interior of a cell from its exterior environment but do also selectively regulate the passage of ions, water and various nutrients through them. Thus, biological membranes are semipermeable barriers that envelope all cells but also intracellular organelles such as nuclei, mitochondria, the cytoplasmic reticulum, or lysosomes.

A cell membrane does mainly consist of phospholipids forming a bilayer, into which cholesterol and various different proteins are embedded that are important for various cellular functions. For example, they help in maintaining the acidity of the intracellular and extracellular environment, thus controlling the pH. They serve as a catalysts in the translocation of ions, nutrients, neurotransmitters and numerous drugs across a membrane [108, 40]. They do also play a vital role in the controlled flux of molecules through ligand-gated ion channels, in signalling and in regulating the membrane curvature and cell deformability through spectrin-actin attached membrane skeleton [49, 112, 134, 81]. These crucial processes require interactions of both lipids and proteins through binding-unbinding mechanisms, vesicle fusions, or through diffusion [97, 55, 128]. Diffusion is the most fundamental process of molecular transport in cell membranes and an important factor in maintaining its fluidity, controlling the dynamics and functioning of the mem-

brane [61, 109]. In-depth knowledge of membrane dynamics and its structure is essential for understanding the functional role of membranes and all processes involving them. Therefore, a precise quantitative characterisation of diffusion in membranes is important information.

In 1972, Singer and Nicolson introduced the fluid mosaic model of a cellular membrane, which became a pioneering concept for all future models of cellular membranes, presenting a heuristic picture of membrane structure and organization [133]. In particular, it introduced the idea of a random membrane organisation that is governed by free diffusion. It proposed that the cellular membrane represents a two-dimensional fluid of lipids that is densely decorated with proteins. The model emphasised the importance of diffusion as transport mechanism. The model asserts that the lipids and proteins in a membrane are in constant lateral motion, thus enabling the interaction between different components over time. Following the work of Singer and Nicolson, Saffman and Delbrück developed a model that gives a quantitative description of the translational diffusion of membrane components [118]. The model applies the idea of Brownian motion to a membrane that is considered to be a two-dimensional fluid sheet. It describes proteins as cylinders diffusing in an infinitely extended viscous sheet of lipids. The model has been highly successful for thin liquid crystal films [95, 37] and isolated cylindrical molecules embedded in a homogeneous film [22, 106], but it has some significant limitations which become relevant when moving from homogeneous to heterogeneous membrane systems. Real biological membranes consist of a huge number of different kinds of lipids and thousands of proteins, and they are highly asymmetric and heterogeneous in nature [14, 145]. The distributions of lipids and proteins across the two leaflets of a bilayer is highly variable [115].

Another shortcoming of the Saffman-Delbrück model is its inability to capture the dual-leaflet nature of a membrane, which becomes particularly important when studying supported lipid bilayers (SLBs). The direct contact of the solid support with the proximal leaflet of the bilayer is not accounted for by model. How does the solid support influence the membrane dynamics and structure? How do the leaflets interact with each other? The model does not incorporate details such as the different lipid mobility in the inner and outer leaflets of a membrane [150, 123, 129, 82]. While many theoretical

studies and molecular dynamics simulations have addressed the above topic, comprehensive experimental data is still lacking. The experimental challenge is the extremely small distance of ∼5 nm between the leaflets which is by two orders of magnitude smaller than the diffraction-limited optical resolution of a microscope (ca. 500 nm along the optical axis, for a well-adjusted confocal microscope).

The last three decades have seen a revolution in optical microscopy, leading to a variety of new methods called super-resolution microscopy that overcome the resolution limit of a conventional optical microscope. The first of these techniques was stimulated emission depletion microscopy (STED)[50]. STED uses a donut-shaped beam that de-excites fluorescent molecules that were before excited by a diffraction-limited excitation beam into their first excited state, and in this way it reduces the volume out of which fluorescence is generated. This results in an improved spatial resolution when using this tandem of diffraction-limited excitation plus donut-beam induced de-excitation for scanning a sample, as in conventional laser-scanning confocal microscopy (LSCM). A few years after the introduction of STED microscopy, another class of super-resolution microscopy, single molecule localization microscopy (SMLM), was introduced. The most prominent representatives of this class are Stochastic Optical Reconstruction Microscopy (STORM) [117] and Photo-Activated Localization Microscopy (PALM) [10]. Both methods utilise photo-switchable fluorophores and the fact that the image of an isolated single molecule can be localized with much higher accuracy than the width of this image itself. By labeling a sample with photo-switchable fluorophores and then taking many images where in each image, only a few well-isolated molecules are visible, one can sequentially build up a map of all single-molecule localizations which delivers eventually a super-resolved image of a sample. While all these methods provide a lateral resolution that can be more than two orders of magnitude better than what is achievable by a conventional microscope, it was not so simple to extend this resolution improvement to the third dimension.

For SMLM, several techniques have been invented for achieving also super-resolution along the optical axis. Among them are astigmatic imaging [56], bi-plane Fluorescence photoactivation localization microscopy (fPALM) imaging [60], or wavefront shaping [104]. But all these techniques deliver an axial

resolution that is still 3 to 5 times worse than their lateral resolution, far from what would be necessary to resolve the two leaflets in a bilayer. Moreover, these methods have a low temporal resolution and are often technically complex. When it comes to measuring distance on the molecular length scale, Förster resonance energy transfer (FRET) has become an efficient and widely used method [116, 78]. However, the working range of FRET is limited to ca. 10 nm and it requires the labelling of the two leaflets with two different dyes, a donor and an acceptor, which can be a nontrivial task by itself. For measuring diffusion coefficients in membranes, Nuclear magnetic resonance (NMR) has occurred to be a powerful method [53]. Unfortunately, it requires large amounts of sample, and the requirement to measure in deuterated solvents can skew the value of the obtained diffusion coefficient (diffusion time ratios between measurements in D_2O and H_2O can be as much as 1.24, see ref. [86]). Moreover, its application to biological samples can be challenging and complex due to the usually small amount of available sample and the difficulties of isotopic labelling.

In this thesis, I present a new method of super-resolution microscopy that allows me to distinguish between individual leaflets of a Supported lipid bilayer (SLB) and to measure axial distances with nanometer accuracy. Moreover, it allows me to measure the diffusion of lipids in an SLB with a leaflet-resolved manner. Such SLBs serve as simple model systems to study membrane dynamics, and our method will allow me to see interaction between the leaflets and the effect of an SLB's proximity to the substrate. For this purpose, I combine Metal-induced energy transfer (MIET) with scanning Fluorescence Lifetime Correlation Spectroscopy (sFLCS). MIET exploits the strongly distance-dependent quenching of a fluorophores by a nearby metal (or graphene) layer. It is based on the electromagnetic coupling of the excited state of a fluorescent molecule to surface plasmons in the metal. This coupling takes place on the length scale of 100-200 nm, where the fluorescence lifetime and intensity are monotonous functions of distance. Thus, by measuring the fluorescence lifetime of a molecule, one can convert the measured lifetime value into a distance value form the metal surface. When replacing the metal layer with a single sheet of graphene, the axial resolution of this method can be pushed down to sub-nanometers, due to the much more localized quenching of fluorescence by graphene. Thus, Graphene-Induced

Energy Transfer (GIET) imaging yields a ca. tenfold better resolution than MIET. This thesis will mainly focus on MIET/GIET and its application to studying membranes. In combination with FLCS, I am able to determine leaflet-specific diffusion coefficients. A major part of this thesis involves leaflet-resolved diffusion studies on model SLBs.

The next section will give an overview of the used membrane system and will give a brief description of lipid diffusion as required for understanding the later results presented in this thesis.

1 Membrane structure and organisation

In recent decades, many membrane models have been proposed for investigating the structure, properties, and function of biological membranes. The famous Singer and Nicolson model [133] brought a paradigm shift to membrane research by suggesting new ways of thinking about membrane function and membrane-related phenomena. They proposed a fluid-mosaic model which views membranes as a two-dimensional viscous solution (matrix of phospholipids) densely decorated with fully or partially embedded proteins. It served as the starting point for the development of many subsequent, more refined models.

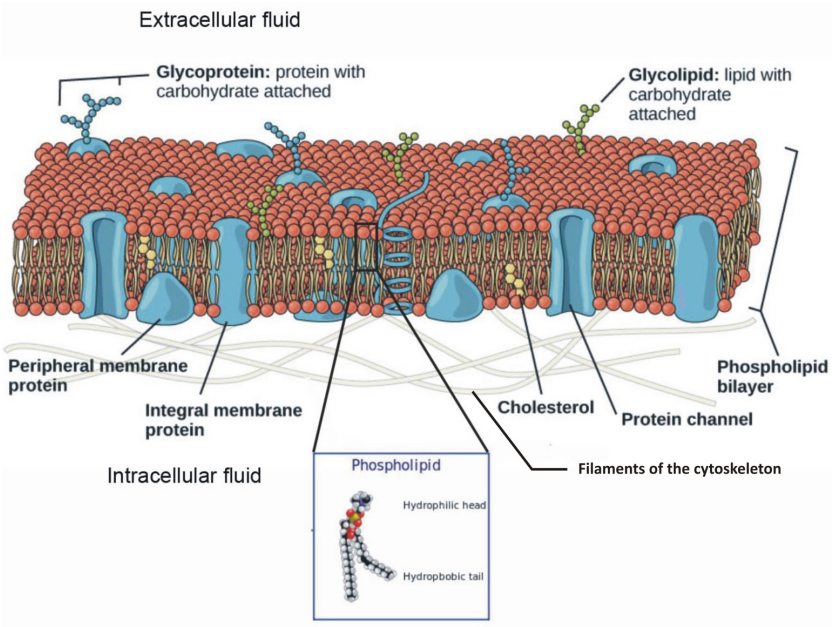

Abb. 1.1: Model view of membrane with all its components.

Following the mosaic model and with new experimental results from electron microscopy, Henderson and Unwin introduced a membrane theory which pictures a membrane as a 3-dimensional structure [51]. The membrane is thought to be a bilayer, with some proteins protruding both leaflets, and some covalently linked to lipid head groups. These proteins in membranes play a significant role in cellular membrane function. The lipid bilayer itself can exist in different phases, in a gel-like phase, a liquid ordered phase, or a liquid disordered phase, leading to the formation of micrometer-sized islands called lipid rafts.

The lipid bilayer has the ability to self-organise in aqueous solutions, due to the amphiphilic nature of lipids. The hydrophilic headgroups of lipids have the strong tendency to face water molecules, whereas the hydrophobic fatty acid tails assemble into a bilayer, minimising the interaction energy of the system by hiding the hydrophobic core from the surrounding aqueous environment. There exists a wide diversity of lipids in biological membranes, which consist lipids of different fatty acid chain length, degree of saturation, or headgroup charge. Figure 1.2 shows the structure of the lipids that were used in this thesis work.

Biological membranes are highly heterogeneous in their composition. The difference in membrane composition plays a significant role in the functionality of membranes. For instance, the lipid bilayer of the endoplasmic reticulum (ER) of a eukaryotic cell has lower cholesterol content than the bilayer of Golgi or other cell organelles. The ER synthesizes cholesterol which is transported to other organelles, thus allowing the insertion of freshly synthesized membrane material into less rigid membranes [145]. Membrane heterogeneity is even seen across leaflets: In mammalian cells, the outer leaflet is predominantly enriched with phosphocholine (PC) and sphingomyelin, whereas the PS and PE are predominantly present on the inner leaflet of the membrane [14]. Even proteins associated with the outer and inner leaflets are performing different functions. For example, in epithelial cells, chloride ion channel play an important role in maintaining the viscosity of mucus on the outer surface.

In connection with heterogeneity of membrane composition, there exists also evidence for membrane thickness fluctuations on the order of few angstroms [149]. Membrane thickness and membrane fluidity are primarily defined by its constituting lipid acyl chains and their saturation [87]. For example, increasing hydrophobic acyl chain length from 12 to 14 or 16 carbon atoms increases membrane thickness from D_H = 29.6 Å to 32.2 Å and eventually 38.6 Å, respectively [69]. Moreover, the presence of double bonds in acyl chains leads to bilayer thinning. Another important parameter that influences the structure and fluidity of a membrane is temperature.

Temperature changes have long been associated with phase changes. Increasing the temperature results in lipid conformational changes that, at a critical temperature T_m, lead to the formation of isomers [48, 76], which increases the

Lipid	**Critical temperature,** T_m(deg **C**)
DOPC	-17
POPC	-2
DMPC	24
DPPE	63
DLPC	-2
DLPE	29

Table 1.1: Summary of critical transition temperatures of the lipids used in this thesis. Reference taken from "Avanti Polar Lipids" website.

lateral diffusion of lipid molecules [38] and leads to a significant expansion of the area per lipid [69]. At temperatures below the critical temperature, bilayers exist in an solid/gel phase where Van-der-Waals interactions lead to tighter, ordered lipid packings. At temperatures above the critical temperature, fluid disordered bilayers exist. A list of lipids with their critical temperatures is shown in table 1.1. Typically, biological samples have constant temperatures, but changes in ionic strength or pH, or the presence of mono- and divalent cations show a strong influence on a bilayer's phase [141]. In summary, cellular membranes are intricate systems of strongly heterogeneous composition that perform important cellular functions. Studying the dynamics of these membranes *in vivo* is a huge challenge, therefore we employ model bilayer systems for simplification.

2 Artificial membranes

As opposed to the native cell membranes which are influenced by many different external parameters, artificial membrane systems are well-defined and can be perfectly controlled, which has made them a favorite system for many biophysical studies. Among them, Supported lipid bilayer (SLB)s are most widely used as model systems that mimic a cell membrane. SLBs are planar bilayers deposited on a solid support. SLBs are formed by fusing vesicles onto a solid substrate, or by covering a substrate in a Langmuir trough. Due to the support, SLBs are highly stable. A bilayer's ability to withstand vibrations and even the presence of holes does not affect its integrity, which

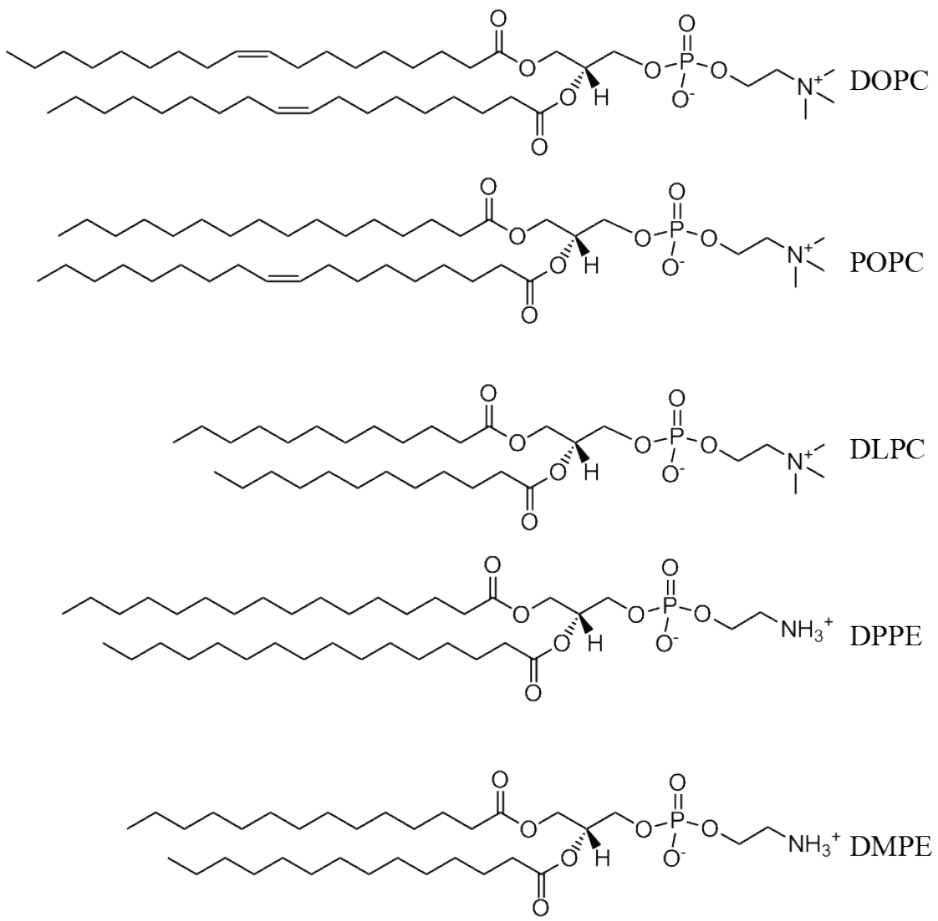

Abb. 1.2: Glycerophospholipds with different fatty acid chain lengths and degree of saturation.

makes it a perfect choice for characterisation techniques that require a solid support.

The most common example of such a technique is Atomic force microscopy (AFM) which is widely used for studying membrane topography. It allows the imaging of lipid phase separation and to study protein lipid-interactions [140, 75]. Another scanning probe technique that would be impossible to use on membranes without support is Quartz crystal microbalance (QCM) which contributed in studying adsorption kinetics at a surface [32]. Evidently, it has been found that the proximity induces membrane-support interactions [84], although there exists a thin water layer (hydration layer) of typically of 1 - 2 nm thickness that separates an SLB from the solid support [68, 15]. Despite this thin hydration layer, there exists an hydrodynamic coupling of an SLB to the support resulting in slower lateral diffusion of lipids as

compared to that in a free-standing bilayer of the same composition [72]. Groves and coworkers observed inhibition of lateral diffusion of lipids on ITO and chrome supports [47]. Another study of SLBs suggests that the dynamic behavior is predominantly governed by lipid/substrate interactions [84]. It reports the presence of a less mobile fraction of lipids on alumina as compared to silica, as a result of the presence of a viscous hydration layer and of immobilised defects. Therefore, the effect of a support needs to be taken into account when interpreting results obtained from SLBs. In this thesis, a so-called sticking model will be used that takes into account reversible adsorption/desorption of lipid molecule to and from the support when modeling their lateral diffusion.

3 Membrane localisation techniques and translational diffusion with fluorescence microscopy

Two-dimensional membrane models have always assumed that the translational diffusion of lipids in the top and bottom leaflets is equal. This has been set as a fundamental principle behind all diffusion studies of membranes so far. This assumption simplifies the modeling of membrane diffusion and is due to the difficulty to resolve the diffusion in a leaflet-resolving manner. For SLBs, this may not be a correct assumption anymore, because the bottom leaflet is separated from the solid support by only an approximately 1-2 nm thick hydration layer, which may impact the mobility of its lipids. In contrast to the top leaflet, which is not bordering to such a hydration layer plus support, this difference in the local environment may lead to strongly different diffusion behavior.

To quantify the diffusion of lipids in a SLB in a leaflet-resolving manner, one needs a technique that can distinguish between the two leaflets. The most common techniques measure density profiles across a lipid membrane with angstrom resolution are Small-Angle X-ray Scattering (SAXS) and neutron scattering. Both methods are very efficient in determining a bilayer's structural parameters, even though both methods cannot be directly compared with each other. In SAXS, the distance between peaks in the electron density profile is determined, i.e the distance between the phosphate groups of the lipid head groups, whereas neutron scattering utilises the high contrast between the protonated lipids and deuterated water to obtain the bilayer thickness [69]. Both SAXS as well as neutron scattering are technically challenging and highly complex. Other techniques that are based on NMR are also challenging due to spectral crowding, thus requiring non-trivial isotopic labelling. Moreover, sample heterogeneity and sample dynamics lead to additional line width broadening [73] which complicates data evaluation. Fluorescence-based techniques such as FRET have been widely used in membrane studies, for investigating membrane heterogeneity [24], lipid-protein interaction [101], or for localizing proteins in membranes [46]. However, implementing FRET for leaflet-resolving studies is a difficult task, since it requires careful labeling of both leaflets with either donor or accep-

tor. Moreover, one flip-flop of lipids between leaflets that can happen on timescales of minutes can potentially change the distribution of donor and acceptor molecules between leaflets [90]. In this thesis, I will use MIET for localizing lipids and proteins in SLBs with leaflet-resolving resolution [63]. This method is simple and reliable, and achieves nanometer axial localisation accuracy. Similar to FRET, MIET is based on the energy transfer from a fluorescent molecule (donor) to a thin metal film (acceptor), which induces the lifetime-to-distance dependence. Compared to FRET, MIET does not require acceptor labeling, because the metal film serves here as the acceptor. For the conversion of lifetime values into corresponding distance values (distance from metal film), one needs only knowledge about the free space lifetime of the used fluorophore (in the absence of metal film), its quantum yield, and its three-dimensional orientation. The physics behind MIET will be explained in a subsequent section.

Although all these techniques are efficient in delivering information about structure and organisation of a membrane, complementing them with dynamic studies can shed more light on the complete membrane structure-function relationship [35]. In this respect, optical methods such as fluorescence recovery after photobleaching (FRAP)[136] Single particle tracking (SPT) and Fluorescence correlation spectroscopy (FCS) are the most prominent techniques [119]. In FRAP, a small region of the sample is bleached, and the time course of fluorescence recovery is measured. This recovery depends on how quickly fluorescent molecules diffuse laterally within a bilayer. In practice, FRAP requires a high intensity laser beam focused into a small excitation area of the sample for efficiently bleaching all fluorescent molecules in this area. A second low intensity laser beam is then used to excite the full field of view and to watch the diffusion of fluorophores back into the bleached area. The recorded recovery curve is fitted with an appropriate model to obtain a diffusion coefficient. The shape and characteristic time of the recovery curve is determined by the mobility of the fluorescently labeled molecules and by the size of the bleached spot. FRAP works well for long timescales, typically from seconds to minutes, and the obtained efficient diffusion coefficient is a combination of both diffusion and potential binding kinetics [25]. FRAP requires densely labelled samples, unlike FCS or Single Particle Tracking (SPT) that both work at extremely low fluorophore concentration. When

using FRAP, care must be taken to prevent localized heating by the bleaching laser. While data evaluation in FRAP is straightforward when studying planar system such as SLBs, the method requires additional attention when applied to complex biological systems (such as wrinkled cellular membranes). In these cases, all parameters that can potentially influence the fluorescence recovery have to be fully taken into account [93]. For non-planar membranes in three dimensions, axial motion of labeled molecules is difficult to consider when modeling the recovery curve. Moreover, for multiple diffusing species or rapid diffusion, FRAP fitting becomes challenging. When the size of the bleached area is reduced to the diffraction limit, FRAP results become less reliable. Moreover, FRAP is an ensemble technique that lacks single molecule sensitivity.

An alternative methods for studying the mobility of molecules in lipid bilayers is Single particle tracking (SPT). In this method, the motion of fluorescently labelled single molecules (or particles) is recorded. This is done by imaging and identifying single molecules (or particles) in each frame of a recorded wide-field microscopy movie, and then to reconstruct their trajectories by connecting individual localizations across subsequent frames. These trajectories show the random walk of the observed molecules, and one can calculate the mean-squared displacement (MSD) of these trajectories. For purely Brownian motion, the MSD is proportional to $2dDt$, where D is the diffusion coefficient, t the time from start of a trajectory, and d the dimensionality of the motion (usually $d = 2$ for membranes). One can calculate the MSD for a single trajectory, or compound it over many trajectories of different molecules, thus resulting in an ensemble-averaged MSD and diffusion coefficient. Similar to SMLM, in SPT one uses the fact that one can determine a single molecule's position with much higher accuracy than the optical resolution of the used microscope. Thus, SPT accomplishes exceptionally high spatial resolution, provided one deals with sufficiently bright samples. SPT has been commonly used to quantify dynamics of lipids and proteins in membranes, which has led to the discovery of non-Brownian motion in plasma membranes due to obstructive diffusion caused by the presence of traps or obstacles that bind the mobile species, or due to confined diffusion or directed motion of molecules [120]. The disadvantage of SPT is the requirement of extremely low labelling concentrations. But SPT is an excel-

lent tool for studying lipid diffusion in SLBs and has been used for control experiments in this thesis.

Unlike FRAP and SPT, Fluorescence correlation spectroscopy (FCS) is based on correlating temporal fluctuations of a fluorescence signal recorded from a small sample area or volume. It has been widely used to characterize membrane fluidity and phases in lipid bilayers [43], but it is also capable of studying inter- or intramolecular reactions [6]. Although FCS is intrinsically a single-molecule technique (only temporal correlations of the fluorescence signal from one and the same molecule contribute to an FCS curve), it needs averaging over many molecules. For obtaining maximum FCS curve amplitude, there should be ideally only one emitter in the detection volume (area) at any time. Taking into account that a diffraction-limited detection volume is typically on the order of one femtolitre, the optimum concentration for FCS measurements is on the order of pico- to nanomoles per liter. This sensitivity makes FCS an ideal technique for studying sample inhomogeneities on a micrometer length scale. Moreover, FCS gives real-time access to a multitude of parameters such as diffusion coefficients, concentrations, or binding/unbinding kinetics, provided the timescales of the different process are well separated. Although FCS allows for precise determination of diffusion coefficients, it requires precise knowledge of the detection volume which can pose problems in membrane measurements where slight changes of the in axial position of the exciting laser beam with respect to the membrane can dramatically change the diameter of the excitation spot (due to the strong divergence of a tightly focused laser beam). For this purpose, FCS modifications such as Dual Focus Fluorescence Correlation Spectroscopy (2fFCS) [28] or scanning FCS [105] were introduced. This methods provide an intrinsic length scale calibration that allows for determining a precise value of the detection volume (area) and thus of diffusion coefficients. However, the spatial resolution of FCS is still limited by the diffraction-limited focal size. Thus, quantifying lipid diffusion in a leaflet-resolving manner is still out of reach. Therefore, in this thesis, I combine MIET with Fluorescence Lifetime Correlation Spectroscopy (FLCS) [44] to enable diffusion measurements in a leaflet-specific manner. In the following chapter, I will describe and discuss the fundamental principles of these techniques in detail.

CHAPTER 2

Fundamentals

1 Principles of Fluorescence

Fluorescence is the process when a molecule absorbs light of a specific wavelength and re-emits light of a different wavelength. Fluorescence has been an intriguing phenomenon since several centuries. The natural occurrence of fluorescent species has only ignited the curiosity since the beginning of times and has led to many fascinating new discoveries. One such example is a recently found shark species that skin of which shows fluorescence as shown in figure 2.1 along with the moiety of molecules responsible for its color [102]. As we know, not all species illuminate under the UV excitation. Molecules that emit fluorescence are termed fluorophores. The energy of light emitted by a fluorophore depends on its chemical composition and its environment.
As we know from quantum mechanics, light is quantized. A quantum of light is called a photon. A fluorescent emitter can be depicted by a two state energy diagram as shown in figure 2.2. The electronic states of a molecule shown there are the ground and first excited singlet (S_0 and S_1) states and and the lowest-energy triplet (T_1) state. Here, all valence electrons of the molecule are in a spin-paired state. These electronic states are subdivided into vibronic sub-states. The vertical arrows depict transitions between different states. The transitions between electronic states are governed by the

Franck-Condon principle which states that electronic transitions take place much faster than any nuclear motions. When exciting a molecule with light of suitable wavelength, it can absorb ($\leq 10^{-15}$s) a photon and jumps into the higher energetic state, the first excited singlet state, S_1. The molecule may end up in any of the many vibrational levels of this state (see Jablonski diagram in figure 2.2). The chance that the molecule is excited into any of the higher electronic states depends on the excitation wavelength and the transition probabilities. In the first excited singlet state, the molecule undergoes fast vibrational relaxation that typically occurs on a timescale of $10^{-10} - 10^{-12}$s, so that it reaches after this time the lowest vibrational state of this state ($S_{1,v=0}$) (Kasha's rule). The energy which is freed by this relaxation is dissipated into heat via molecular collisions.

To depopulate the first electronic state (S_1), the molecule can take alternative paths. It can radiatively decay to the ground state (S_0) through fluorescence. This fluorescence transition happens on timescales of 10^{-9} s. Due to the non-radiative vibronic relaxation in the excited state, and the possibility to jump to a higher vibronic level in the ground state, the energy of the emission is typically smaller than that of excitation. This is observed as a spectral shift of the emission spectrum with respect to the absorption spectrum and is called Stokes shift. As seen in figure 2.3, the emission spectrum of the dye Atto655 is red-shifted with respect to its absorption spectrum. This spectral shift is exploited in fluorescence applications for separating fluorescence emission from excitation light. Because transitions between S_0 and S_1 can take place between different vibronic levels in these states, both absorption and

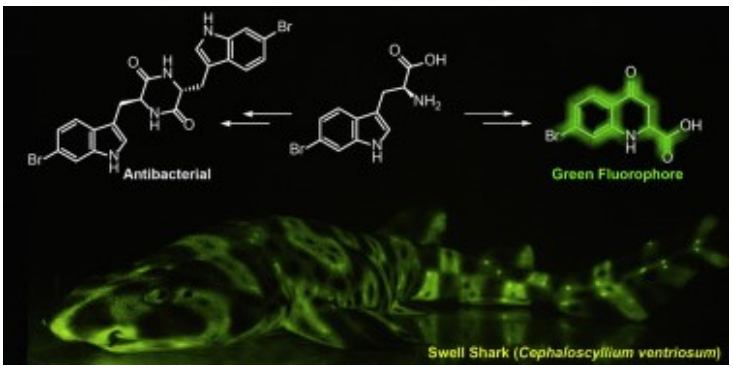

Abb. 2.1: Fluorescent imaging of shark (Cephaloscyllium ventriosum) and the fluorophore responsible for its fluorescence

emission spectra are broadened. Furthermore, every vibrational level has energetic sub-levels corresponding to different rotational states, which further broadens the spectra. Finally, due to Kasha's rule, emission spectra are usually independent on the excitation wavelength. This rule states that emission does always occur from the lowest vibronic level in the lowest electronically excited singlet state $S_{1,v=0}$. Both Kasha's rule and the Franck-Condon principle apply both to absorption and emission, resulting in mirror-symmetric spectra, as clearly visible in the absorption/emission spectra of Atto655.

Alternatively, the transition from S_1 to S_0 state can also happen non-radiatively with a transition rate k_{nr}, which is similar to the radiative transition rate k_r. This non-radiative transition involves the release of energy in the form of heat to the environment. Processes such as internal conversion, intersystem crossing, and intra- and inter-molecule quenching contribute to the non-radiative transitions. The average time a molecule spends in its first

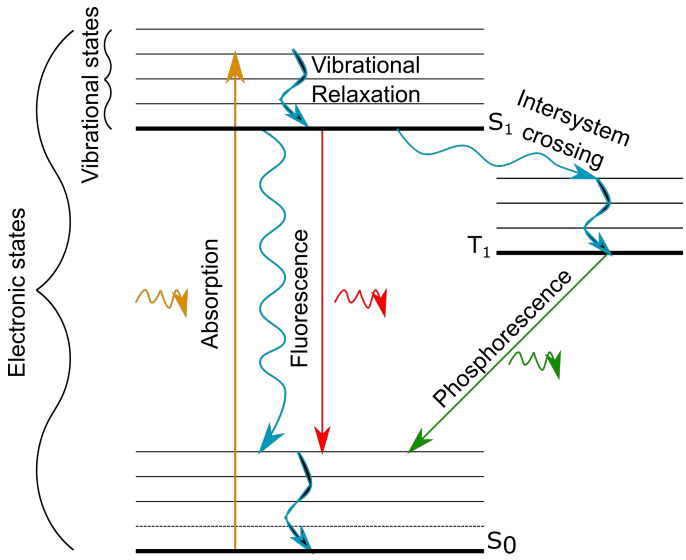

Abb. 2.2: Simplified Jablonski diagram depicting the electronic and vibrational states of an organic molecule (horizontal lines) and the possible transitions between them (vertical arrows). A fluorophore absorbs light of a suitable wavelength and jumps from the ground state S_0 to the first excited electronic state S_1, as shown by the brown arrow. Then, it undergoes vibrational relaxation before coming back to the ground state through fluorescence (shown in red) or through a non-radiative process shown in blue. Alternatively, the molecule can follow a forbidden transition and returns to the ground state by phosphorescence through a triplet state (shown in green)

excited state (S_1) is called the fluorescence lifetime (τ). It is a characteristic property of the molecule and is given by

$$\tau = \frac{1}{k_r + k_{nr}} \tag{2.1}$$

Values of fluorescence lifetime are usually on timescales of nanoseconds (10^{-9} s). Considering fluorescence as a two-step process, the fluorescence lifetime can be modeled by equation 2.2. Knowing that the momentary fluorescence intensity is proportional to the number of excited fluorophore, this results in an exponential decay of fluorescence intensity $I(t)$ with decay time τ, as described by equation 2.2

$$\frac{I(t)}{I_0} = \exp\left(-\frac{t}{\tau}\right) \tag{2.2}$$

where $I(t)$ is the fluorescence intensity at time t and τ is the fluorescence lifetime. The fluorescence lifetime of a fluorophore is sensitive to various environmental changes such as pH, solvent viscosity, or interactions with the local environment. This parameter is hence an important asset for probing the local environment in many studies. For a mixture of fluorophores, or in the presence of multiple intermolecular interactions between a fluorophore and its environment, the fluorescence decay may become multi-exponential.

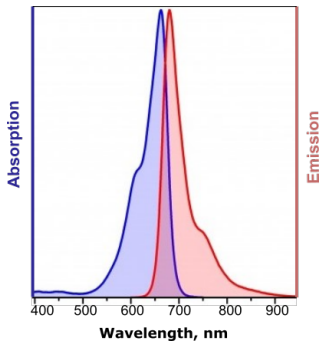

Abb. 2.3: Absorption and fluorescence emission spectra of the dye Atto655, shown in blue and red, respectively. Emission occurs at longer wavelengths than absorption, as depicted in the figure, and which is known as Stokes shift. Figure taken from ATTO-TEC GmbH.

$$I(t) = \sum_i a_i \exp\left(-\frac{t}{\tau_i}\right) \tag{2.3}$$
$$\sum_i a_i = 1$$

In such multi-exponential decays, each fluorescent component with lifetime τ_i contributes with a certain amplitude a_i to the total signal. A detailed explanation of how to measure fluorescence lifetimes is given in section 2.
Another characteristic parameter of fluorescence is its quantum yield (ϕ), expressed by

$$\phi = \frac{k_r}{k_r + k_{nr}} \tag{2.4}$$

The quantum yield is a measure of how well a molecule emits fluorescence when transiting from its excited to its ground state. In other words, ϕ is the fraction/ratio of emitted photons to the total number of absorbed photons. To ensure maximum fluorescence quantum yield, the non-radiative transition rate k_{nr} should be as small as possible. This can be achieved when taking several aspects of the molecular structure of a dye into account. Non-radiative transitions can be minimized by ensuring that the dye exhibits a rigid molecular structure, which minimises the loss of energy due to rotations or vibrations. Moreover, one can reduce the intersystem crossing rate by reducing the spin-orbit coupling that makes the theoretically forbidden transitions between singlet and triplet states possible. Additionally, the chances for any possible charge transfer transitions should be kept low. These criteria govern the selection of dye molecules for fluorescence microscopy.
Another path that a molecule can when returning from the first excited singlet to the ground state involves a transition to the triplet state (T_1) (intersystem crossing). This transition involves the flip of the electron spin. Generally, the probability of such a transition is fairly low, because spin flips are theoretically forbidden processes (angular momentum conservation). However, from time to time such transitions can take place due to spin-orbit coupling, and when the vibrational levels of the singlet and triplet states overlap. In the triplet state, the molecule undergoes vibrational relaxation to reach the lowest vibrational state of T_1. Since the transition to the triplet state is a spin-forbidden transition, it takes place on timescales of approximately 100 s.

Similar to the singlet state, a molecule can decay from the triplet to the singlet ground state radiatively or non-radiatively. The radiative decay from the triplet to the singlet state is termed phosphorescence. Usually, phosphorescence is observed at low temperatures or in a highly viscous medium. Triplet state lifetimes can be as long as several seconds. These long lifetimes enhance the chances of a second photon absorption while being in the triplet state, which leads to significant photobleaching. Photobleaching is the permanent loss of fluorescence of the dye due to light-induced structural changes. Therefore, for applications of fluorescence, an important selection criterion is dye photostability, besides fluorescence lifetime and quantum yield.
Experimentally, fluorescence lifetime measurements are carried out by Time correlated single photon counting (TCSPC) and will be explained in the next section, taking into account factors such as background or the instrument response function of the full detection system.

2 Time-correlated single-photon counting

Time-correlated single-photon counting (TCSPC) is a powerful technique used for measuring fast discrete processes in fundamental physics, chemistry, and the life sciences. It requires advanced pulsed lasers and single-photon sensitive detectors. This spectroscopic technique works in the time domain and measures the delay, with picosecond temporal resolution, between detected fluorescence photons and short excitation pulses of a periodically pulsing excitation laser. Typical organic fluorophores exhibit fluorescence lifetimes in the time range from hundreds of picoseconds to tens of nanoseconds. This requires a high temporal resolution of the measurement system to be able to measure with picosecond resolution, which is challenging with traditional photodiodes and electronic amplifiers. TCSPC solves this problem by maximally timing only one photon detection event per excitation cycle. By repeating this timing of many million excitation cycles, one accumulates a complete fluorescence decay curve.

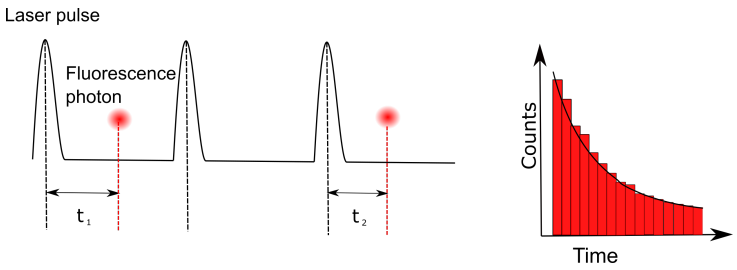

Abb. 2.4: Schematics of a TCSPC measurement. A pulsed laser excites the fluorophores, and the detection time of each detected fluorescence photon (red dots) is recorded with respect to the last excitation laser pulse. These delay times between photon detections and excitation laser pulses are then histogrammed, the histogram showing the fluorescence intensity decay with time.

Thus, the technique relies on the repetitive and precise timing of single photon detection events in each excitation cycle. Figure 2.4 depicts the working principle of TCSPC. A stream of laser pulses excites the sample to induce fluorescence photon emission (red dots). The time difference (t_1 and t_2) between excitation and detection of each photon is recorded with the help of an electronics that works like a stopwatch. A large number of such events is recorded and histogrammed to obtain a TCSPC decay curve. The detection times can be timed with respect to the excitation pulses with a temporal res-

olution down to picoseconds. However, to prevent so-called pileup artifacts in TCSPC, the excitation and detection conditions are adjusted in such a way that one photon is detected only once over dozens or hundreds of excitation pulses (there will be actually no photons in many of the excitation cycles). The cause of pileup is the dead time of the detectors and the electronics after a photon detection event. The processing time for one photon detection event is at least a few nanoseconds. During this time, the detector and electronics cannot detect and register another photon. Therefore, the count rate is typically adjusted to $< 1\%$ of the laser repetition rate.

2.1 TCSPC Setup and schemes

A TCSPC setup consists of a pulsed excitation laser and a single photon counting detector connected to a TCSPC electronics. Typically, the excitation laser provides a timing signal for the TCSPC electronics. This reference signal is also known as the sync signal. The detector produces an electrical pulse for each photon detection. The arrival times of the photons with respect to the laser pulses (sync) are measured and processed by the electronics, and the data is eventually stored in a computer.

An ideal photon detector generates an electrical signal upon each photon detection. However, real detectors such as photo-multiplier tubes (PMT) or single-photon avalanche photo diodes (SPADs) deviate from this ideal behavior (not every photon that hits the detector generates a detection event). Both PMTs and SPADs have their advantages and disadvantages. For example, the quantum efficiency of detection of a PMT is about 25% in the blue-green spectral region. In contrast, SPADs can reach a quantum efficiency of up to 80% in the same spectral region, but for the price of a much smaller active area of detection, which makes optical alignment challenging. Apart from the limitations of the single-photon counting detectors, the excitation source does also contribute to artifacts of TCSPC systems. For example, pulsed laser diodes (PDL) as often used for TCSPC have typically pulse widths of ca. 50-100 ps, which widens the the temporal instrument response function.

TCSPC records the arrival time of each detected photon t_{photon} with respect to the sync time t_{sync}. The time difference is recorded. In very old TCSPC

systems, this timing was done by starting the timer with the each sync and to stop it by a photon detection event ("forward start-stop TCSPC"). This concept was given up with the development of advanced high-repetition laser sources, because then most excitation cycles will not detect a photon, and the timer has to be reset at each sync signal. To avoid this continuous resetting of the timer, modern TCSPC systems adopt the so-called reverse start-stop mode. Here, the timing starts with a photon detection event, and stops with the next sync. Finally, data recorded by TCSPC is fitted using equation (2.2). When the duration of the laser pulses cannot be neglected, one has to record as well an instrument response function $G(t)$ (IRF), which is then used in a deconvolution of the recorded TCSPC fluorescence decay histogram $R(t)$ for extracting the true exponential fluorescence decay curve $F(t)$ using the equation

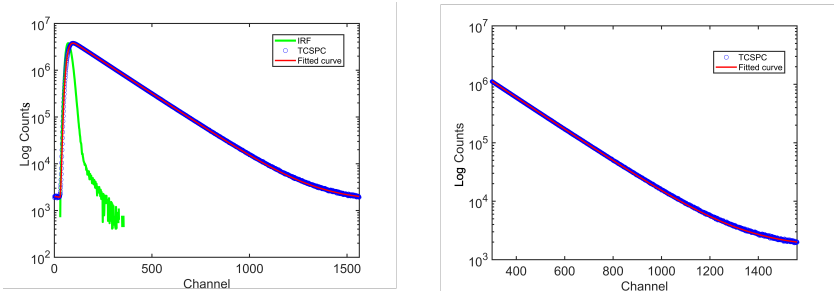

Abb. 2.5: The two figures display the two fitting methods that can be used for fluorescence decay time determination: deconvolution using IRF (left), and tail fitting (right). A recorded fluorescent decay is shown in blue and is fitted with a maximum likelihood estimator (MLE). The first fitting method requires an IRF which was recorded using gold coated coverslip (Green), while in tail fitting a cutoff of 0.3 ns was taken to eliminate the TCSPC channels having a contribution from IRF. The TCSPC resolution is 16 ps.

$$R(t) = \int_0^t G(t')F(t-t')dt' \tag{2.5}$$

The IRF $G(t)$ contains the full information about the temporal response of the complete TCSPC hardware. In order to extract the fluorescence decay time, the recorded data is iteratively fitted with a sum of exponential decay functions convolved with the IRF. The IRF $G(t)$ can be recorded by taking a highly light-scattering solution (LUDOX) and recording a TCSPC decay histogram at the same wavelengths as used for fluorescence detection, and the

same alignment and optical filters. Another way is to use a reflective surface and to reflect the laser into the detector using the same optical alignment as used for the fluorescence TCSPC measurement. Figure 2.6 shows a gold coated glass coverslip that is used to record the IRF.

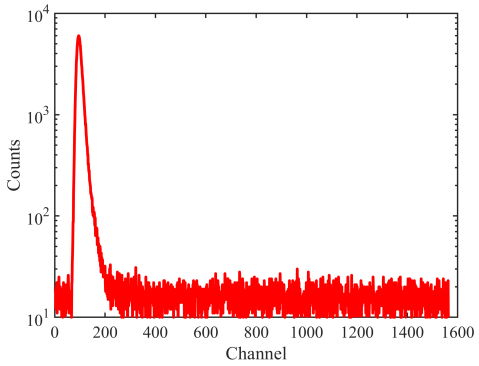

Abb. 2.6: IRF recorded by using a Gold coated glass surface. It has a width of ca. 200-300 TCSPC channels. The excitation laser has a wavelength of 640 nm and a repetition rate of 40 MHz, the TCSPC resolution is 16 ps.

In the case of an IRF with negligible temporal width, tail fitting of the recorded TCSPC histogram can be performed as shown in figure 2.5, where an exponential fitting is carried out after excluding the first $\approx 200 - 300$ TCSPC channels. These initial channels have IRF contributions and are thus discarded from analysis. When measuring the fluorescence from single molecules, only a few photons are collected which poses quiet a challenge to data fitting. In order to obtain precise decay times, one needs a sufficient large number of photon detection events. For such weak signal as single molecule fluorescence, statistical estimator methods have best dealt with the fluorescence decay analysis, the most commonly used being MLE or least squares minimization. With maximum likelihood estimators (MLE), one can even efficiently analyse TCSPC decay data with less than 200 counts [36]. For low intensity signals, also pattern matching algorithms have shown to be extremely efficient in fluorescence lifetime data analysis and will be used in this work.

2.2 Time-Tagged Time-Resolved

Not only the photon arrival times with respect to the last pulse laser are important, but also the photon arrival times on a global time axis starting with the beginning of an experiment. This global arrival time can also be referred as the macro time. This time information can be used for studying fluorescence dynamics on time scales much longer than the laser repetition time, one such example is the measurement of translational diffusion in membranes which typically takes place on a millisecond timescale. As compared to TCSPC which operates on much faster timescales (picoseconds to nanoseconds), for the measurement of much slower intensity fluctuations one needs data recording on timescales from microseconds to seconds.
For recording both the micro- and the macro-times, ones uses time-tagged time-resolved (TTTR) data recording. Modern TCSPC systems record each fluorescence photon detection with a time tag that includes the whole time range of seconds to minutes. Recorded photon detection events are stored with two timings (TCSPC micro-time and the macro-time or macro-time tag). The macro-time records detection times with a temporal resolution equal to the sync time t_{sync}. Therefore, the TTTR data stream comprises of two time values, for each photon arrival, the TCSPC time and the macro time with resolution t_{sync}, together with an additional tag telling in which detection channel a photon was recorded (see figure 2.7).

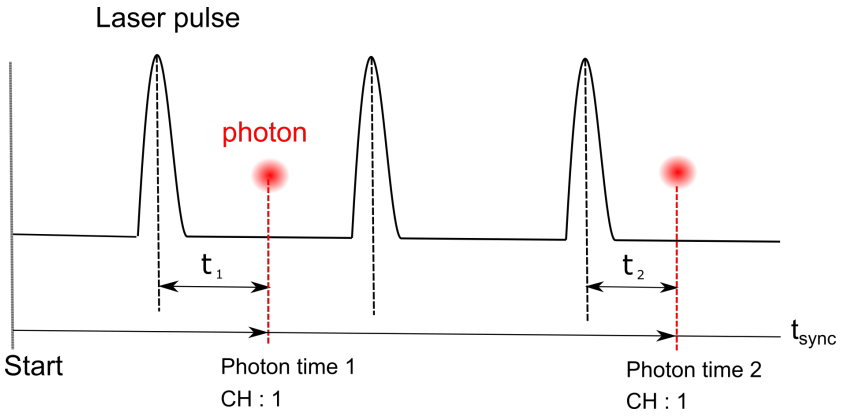

Abb. 2.7: TTTR scheme. The data stream contains the macro- and micro-times. When using more than one detector, the detection channel is also stored in an additional tag.

Additional markers can be added to the TTTR stream which help to syn-

chronise the data stream with spatial scanning when recording fluorescence lifetime scan images using a beam or stage scanner. These markers can contain information of the piezo scanner which is an essential part of a scanning confocal microscope. Here, each photon is associated with a scan line and scan position along the line that can be used to reconstruct the scan image. Moreover, for each virtual pixel in such a scan image, one can pool together all the corresponding photon detection events to obtain spatially resolved TCSPC histograms of each pixel, which can be used to generate a fluorescence lifetime image. Besides that, TTTR is a valuable technique for applications such as fluorescence correlation spectroscopy (FCS), fluorescence lifetime correlation spectroscopy (FLCS), scanning fluorescence correlation spectroscopy, and many others. All these techniques are essential for this thesis, and therefore, they are discussed in much detail in later sections.

3 Single-molecule metal-induced energy transfer (smMIET)

The presence of a metal surface in the vicinity of a fluorophore alters its fluorescence lifetime. This modulation is the physical basis of metal-induced energy transfer (MIET) imaging and spectroscopy. In the late 1960s, experiments conducted by Schäfer and co-workers observed a remarkable variation of the fluorescence lifetime of europium dibenzoylmethane complexes in close distance to a reflecting metal mirror. They described this effect using a classical interference model, which says that a molecule's emitted electromagnetic field is back-reflected from the mirror and modulates the emission of that molecule (interference of primary with back-reflected emission) [31, 71, 30, 139]. The experiments were later put into the framework of a more general theory developed by Chance, Prock and Silbey which does also take near-field effects into account (relevant for short distances where energy transfer between metal and the emitter is crucial) [16]. The theory perfectly fits experimental data at all distances. Following the above research work, a series of papers focused on the modulation of fluorescence emission properties when placing a fluorophore into different solvents or dielectric media [80, 79]. The idea was to alter the radiative transition rate by changing the dielectric environment of a dye.

In the beginning, this concept did not find many applications, but with advancements in fluorescence microscopy, it gained interest again. The ability to detect and to investigate the fluorescence emission of single molecules made possible to observe the emission properties of a single fluorophore and also its modulation by the environment. Unlike ensemble measurements where small fluorescence fluctuations are usually averaged out, with single molecule spectroscopy and imaging it is possible to study the behaviour of individual fluorophores in much detail. One such behaviour of a single fluorophore is the so-called blinking. Here, the molecules transits between and "on" state (active fluorescent state) and an "off" state (non-fluorescent dark state). In MIET, one places fluorescent emitters close to a metal film and measures the changed fluorescence lifetime, which is then converted into a precise distance of the emitter from the metal. This allows one to measure axial distances

with an accuracy of a few nanometers. The excellent performance of this methods has been demonstrated in several recent publications of our group [64, 63, 57]. In the following section, I will briefly explain the semi-classical model of the interaction of a dipole emitter with a metal surface, and how it can be used to calculate theoretical curves for the fluorescence lifetime and brightness as a function of distance from the metal.

3.1 Free dipole emission

Most fluorescent molecules can be excellently modeled as ideal electric dipole oscillators, where two opposite charges $+q$ and $-q$ oscillate along the dipole axis with some oscillation frequency ν and amplitude d. The corresponding dipole moment amplitude is then given by $p = qd$. In a Cartesian coordinate system with the z-axis perpendicular to the metal surface, let the angle between the dipole axis and the z-axis be θ, and we denote the dipole position vector by $\mathbf{r}$. The fluorescent molecule should be surrounded by a homogeneous medium with refractive index n (i.e. dielectric constant $\epsilon = n^2$). In such a homogeneous environment, the electric field around such an oscillating electric dipole is given by

$$\mathbf{E}(\mathbf{r},t) = \frac{1}{n^2}\left\{\frac{k_0^2}{r}\left[\mathbf{p}-\hat{\mathbf{r}}(\hat{\mathbf{r}}\cdot\mathbf{p})\right] + \left(\frac{ik_0}{r^2}-\frac{1}{r^3}\right)\left[\mathbf{p}-3\hat{\mathbf{r}}\left(\hat{\mathbf{r}}\cdot\mathbf{p}\right)\right]\right\} e^{ikr-i\omega t} \quad (2.6)$$

where $\hat{\mathbf{r}}$ denotes a unit vector form the dipole position to the point $\mathbf{r}$ where the electric field is calculated, $\mathbf{p}$ is dipole moment, r is the absolute distance between dipole and electric field position $\mathbf{r}$, ω is the angular frequency of oscillation, and we have $k_0 = k/n$. Note that for $k = 0$ and $\omega = 0$ one recovers the well-known electric field around a static dipole. The r^{-1} term in the above expression is called the far field of the dipole, because only this term is connected with energy transport from the emitter towards infinity. The r^{-2} and r^{-3} terms are correspondingly called the near field and they do not partake in far field energy emission.

Thus to calculate the angular distribution of energy radiated by an oscillating dipole, one can neglect the near field components (because they do not contribute to the far field emission) and calculates the time-averaged Poynting vector $\mathbf{P} = (cn/8\pi)\left|\mathbf{E}\right|^2$ for the far field component. The absolute value

P of this Poynting vector (which always points radially away from the dipole position) then gives the angular distribution of emission which reads

$$P(r,\theta) = \frac{cnk_0^4 p^2}{8\pi r^2}\sin^2\theta \tag{2.7}$$

where θ is the angle between the dipole axis and the direction of emission. This result allow us to find the power radiated per solid angle $\mathrm{d}\Omega^2 = \sin\theta d\theta d\phi$ as

$$\frac{d^2S}{d\Omega^2} = r^2 P(r,\theta) = \frac{cnk_0^4 p^2}{8\pi}\sin^2\theta \tag{2.8}$$

Thus, the angular distribution of radiation of an oscillating dipole follows a $\sin^2\theta$ law, and the total power S emitted by the oscillating dipole can be calculated by integrating over the solid angle $d\Omega^2$.

$$S = \int_0^{2\pi} d\phi \int_0^{\pi} d\theta \sin\theta \frac{d^2S}{d\Omega^2} = \frac{cnk_0^4 p^2}{3} \tag{2.9}$$

This shows that for a dipole placed into a medium with refractive index n, the emission power is n-times larger than in vacuum.

3.2 Dipole near a metal surface

The radiative power of a free oscillating dipole in a homogeneous environment was the topic of the previous section, let us now consider the situation of a dipole emitter in front of an dielectric or metal surface.

Thus, consider a dipole with dipole moment p at position $\mathbf{r}_0$ above a planar interface in medium 1 (See figure 2.8). The interface is the $z = 0$ plane and divides medium 1 with refractive index n_1 above from medium 2 with refractive index n_2 below. The core idea for describing the electromagnetic interaction of the emitting dipole with this interface is to represent the dipole emission as a plane wave expansion. Then, each plane wave component with wave vector $\mathbf{k}_1^+$ traveling towards the interface undergoes reflection and transmission, where the reflected wave has vector $\mathbf{k}_1^-$, and the transmitted wave has $\mathbf{k}_2^+$, respectively. The axial components of these vectors along the z-direction will be denoted by $\pm w_1$ and w_2, and their horizontal component is denoted by $\mathbf{q}$. The boundary conditions for the electric and magnetic fields at the interface impose that the vector $\mathbf{q}$ is the same for incident, reflected

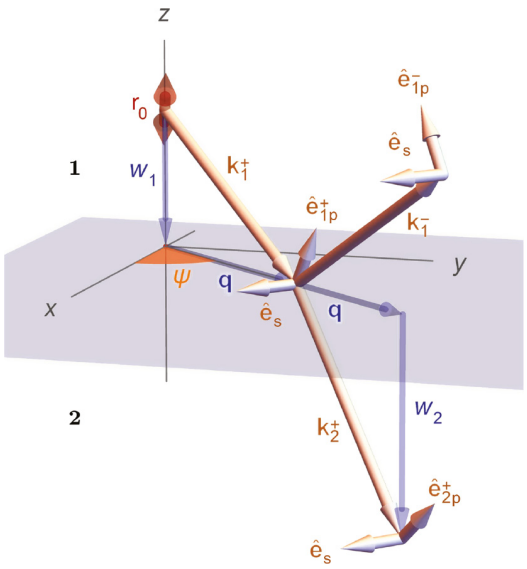

Abb. 2.8: Geometric representation of dipole above an interface. An oscillating electric dipole is present in medium 1 at position $\mathbf{r}_0$ *(shown by double headed red arrow). The dipole's plane wave vector* $\mathbf{k}_1^+$ *is directly emitted by the dipole,* $\mathbf{k}_1^-$ *is the wave vector of reflection from the interface. The unit vector for p and s polarization of the electric field is denoted by* $\hat{\mathbf{e}}_{1p}^{\pm}$ *and* $\hat{\mathbf{e}}_s$ *respectively. Also shown is the wave vector of transmitted wave into medium 2 along with the p- and s-polarization vectors. The projection of all wave vectors onto the horizontal axis is denoted by* $\mathbf{q}$ *while the projection on the vertical axis are* $\pm w_1$ *and* w_2*.* ψ *shows the angle between the horizontal projection on the interface and the x-axis. Reference from [64]*

and transmitted wave. Additionally, one has to consider the polarization of the plane waves. The two principal polarization directions of the incident wave are along unit vector $\hat{\mathbf{e}}_{1p}^{\pm}$ (p-polarization) or along unit vector $\hat{\mathbf{e}}_s$ (s-polarization). The p-polarization unit vector $\hat{\mathbf{e}}_{1p}^{\pm}$ lies in the plane formed by $\mathbf{k}_1^+$ and $\mathbf{k}_1^-$ (incidence plane), where as the s-polarization unit $\hat{\mathbf{e}}_s$ lies parallel to the interface. With all these notations, the primary electric field of an electric dipole emitter at position $\mathbf{r} = \{\boldsymbol{\rho}_0, z_0\}$ is given as follows (Weyl representation):

$$\mathbf{E}(\mathbf{r}) = \frac{ik_0^2}{2\pi} \int\int \frac{d^2\mathbf{q}}{w_1} [\hat{\mathbf{e}}_{1p}^{\pm}(\hat{\mathbf{e}}_{1p}^{\pm} \cdot \mathbf{p}) + \hat{\mathbf{e}}_s(\hat{\mathbf{e}}_s \cdot \mathbf{p})] e^{i\mathbf{q}\cdot(\boldsymbol{\rho}-\boldsymbol{\rho}_0)+iw_1|z-z_0|} \tag{2.10}$$

where the integration extends over the whole two-dimensional $\mathbf{q}$-plane, and the connection between w_1 and $\mathbf{q}$ is given by $w_1^2 + q^2 = k_1^2$. Now, using

Fresnel's theory for the reflection and transmission of plane waves at an planar interface, the reflected and transmitted electric fields $\mathbf{E}_R$ and $\mathbf{E}_T$ are given by the following expressions

$$\mathbf{E}_R(\mathbf{r}) = \frac{ik_0^2}{2\pi}\int\int \frac{d^2\mathbf{q}}{w_1}[\hat{\mathbf{e}}_{1p}^- R_p(\hat{\mathbf{e}}_{1p}^+\cdot\mathbf{p}) + \hat{\mathbf{e}}_s R_s(\hat{\mathbf{e}}_s\cdot\mathbf{p})]e^{i[\mathbf{q}\cdot(\boldsymbol{\rho}-\boldsymbol{\rho}_0)+w_1(z_0+z)]} \quad (2.11)$$

and

$$\mathbf{E}_T(\mathbf{r}) = \frac{ik_0^2}{2\pi}\int\int \frac{d^2\mathbf{q}}{w_2}[\hat{\mathbf{e}}_{2p}^+ T_p(\hat{\mathbf{e}}_{1p}^+\cdot\mathbf{p}) + \hat{\mathbf{e}}_s T_s(\hat{\mathbf{e}}_s\cdot\mathbf{p})]e^{i[\mathbf{q}\cdot(\boldsymbol{\rho}-\boldsymbol{\rho}_0)+w_1 z_0 - w_2 z]} \quad (2.12)$$

where we have $w_2 = \sqrt{k_2^2 - q^2}$, and the $R_{s,p}(\mathbf{q})$ and $T_{s,p}(\mathbf{q})$ are the Fresnel reflection and transmission coefficients for plane p- ans s-waves with lateral wave vector component $\mathbf{q}$, respectively.
The total field in the upper half space ($z > 0$) is given by the sum of $\mathbf{E}$, eq. (2.10), and $\mathbf{E}_R$, eq. (2.12). Using these expressions, the emission power into a solid angle $d\Omega^2$ in the lower half-space can be computed as

$$\frac{d^2S_2}{d\Omega^2} = \frac{ck_0^4 n_2}{8\pi}\left[|T_p|^2\left(\hat{\mathbf{e}}_{1p}^+\cdot\mathbf{p}\right)^2 + |T_s|^2\left(\hat{\mathbf{e}}_s\cdot\mathbf{p}\right)^2\right]\left|\frac{w_2}{w_1}\right|^2 e^{-2\mathrm{Im}(w_1)z_0} \quad (2.13)$$

and similarly for the upper half-space as

$$\begin{aligned}\frac{d^2S_1}{d\Omega^2} = \frac{ck_0^4 n_1}{8\pi}\Big[&\left|\left(\hat{\mathbf{e}}_{1p}^- + R_p\hat{\mathbf{e}}_{1p}^+ e^{2iw_1z_0}\right)\cdot\mathbf{p}\right|^2 \\ &+ \left|\left(1 + R_s e^{2iw_1z_0}\right)\left(\hat{\mathbf{e}}_s\cdot\mathbf{p}\right)\right|^2\Big]\end{aligned} \quad (2.14)$$

where the polar angle θ between the vertical z-axis and the wave vector is defined by $\sin\theta = q/k_1$ in the upper half space and by $\sin\theta = q/k_2$ in the lower half space, and the azimuthal angle ϕ is the angle between the horizontal projection of the wave vector $\mathbf{q}$ and the x-axis. Thus the total emission power S of a dipole at a distance z_0 above the interface is computed as

$$S(\alpha, z_0) = \int_0^{\pi/2} d\theta\sin\theta\int_0^{2\pi} d\phi\left(\frac{d^2S_1}{d\Omega^2} + \frac{d^2S_2}{d\Omega^2}\right) \quad (2.15)$$

where α is the the angle between the dipole vector $\mathbf{p}$ and the vertical z-axis. Interestingly, the α-dependence of this emission power can be expressed more simply by

$$S(\alpha, z_0) = S_\perp(z_0)\cos^2\alpha + S_\parallel(z_0)\sin^2\alpha \tag{2.16}$$

The above model is quite general and can be applied to the dipole emission above any planar system, for examples also a metal layer deposited on the surface of a glass slide. The whole physics of the system is absorbed in the Fresnel reflection and transmission coefficients, which explicitly depend on the specific planar system that is studied. In contrast to a purely dielectric interface or layered system, the interaction of the EM wave with the metal surface results also in partial absorption of radiation in the metal. The absorbed energy is transferred to surface plasmons in the metal and eventually dissipated into heat. We can now use the calculated emission power above for determining the change of the fluorescence lifetime of a fluorescent molecule in the vicinity of an interface/planar system by postulating that the lifetime is inversely proportional to the emission rate. Thus, the ratio of the lifetime in the presence of a (metal) surface τ_{fl} to the lifetime of in free space τ_0 (without interface) is given by

$$\frac{\tau_{fl}(\alpha, z)}{\tau_0} = \frac{S_0}{\Phi S(\alpha, z) + (1-\Phi)S_0} \tag{2.17}$$

where we have now also introduced the quantum yield of fluorescence Φ which tells us which part of the excited state energy of a molecule is indeed radiated away in the form of electromagnetic radiation (and thus influenced by the presence of the interface), and how much is dissipated non-radiatively.
As can be seen, this ratio depends on the orientation of the dipole emitter, more specifically, on the angle α between the dipole axis and the vertical z-axis. However, in most cases of practical interest, fluorescent molecules undergo rotational diffusion that is much faster than the fluorescence lifetime. In that case, we can average out the orientation in the above equation and obtain

$$S(z_0) = \frac{1}{3}S_\perp(z_0) + \frac{2}{3}S_\parallel(z_0) \tag{2.18}$$

In addition to the fluorescence lifetime, also the brightness of an emitter will be changed by the presence of an interface − it will be proportional to the emission power (radiative rate) of the dipole. However, the actual amount of fluorescence that is detected by a microscope will also depend on the angular

distribution of emission (which is also changed in the presence of an interface) and by the half angle Θ of the cone of light detection of the used objective, i.e. by numerical aperture $\mathrm{NA} = n \sin \Theta$. Let the corresponding fraction of detected light be L, then the collection efficiency η of detecting a photon with the objective is expressed as

$$\eta(\alpha, z_0) \propto \frac{L(\alpha, z_0) S_2(\alpha, z_0)}{S(\alpha, z_0)} \tag{2.19}$$

where the α- and z_0-dependence of L accounts for the complex angular distribution of emission that depends on the orientation and distance of the emitter above the interface, and where we have assumed that detection is done from below. When using these equations in calculations for modeling the dipole emission above a thin metal layer on a glass surface, it is found that the collection efficiency drastically decreases with smaller distance of the emitter from the surface, while the radiative rate proportionally increases (i.e. lifetime decreases). In MIET, we exploit this lifetime-distance dependence of a dipole near a metal layer for converting a measured fluorescence lifetime into a distance value. As I will show in the experimental sections later, this allows us to resolve even the $\sim$5 nm axial distance between two leaflets of a SLB. In the next chapter, I will discuss in detail the optical resolution of optical microscopes and in particular their axial resolution.

4 Optical resolution of a fluorescence microscope

Imaging techniques have always been of enormous importance in all fields of research. With the advancement of optical microscopy, many biological processes and functions have been studied in detail and in living cells. One of the most widely used techniques here is fluorescence microscopy, where one uses specific labeling with fluorescent dyes for visualizing specific targets. Nowadays, we have a wide variety of organic dyes and fluorescent proteins across the whole visible spectrum available for specific labelling of all possible targets in cells and tissue. This is usually achieved by using antibody-based immunostaining (organic dyes) or genetic engineering (fusing fluorescent protein to protein of interest).

In conventional fluorescence microscopy, two adjacent fluorescent emitters can be resolved if their distance is not much smaller than the wavelength of the emitted light. The so-called diffraction limit of the spatial resolution is due to the diffraction and interference properties of light, and an exact quantitative expression of this diffraction-limited resolution was first formulated by Abbe [1]. He found that two point sources that are placed at a distance smaller than

$$d_{min} = \frac{\lambda}{2n \sin \Theta} = \frac{\lambda}{2\mathrm{NA}} \tag{2.20}$$

cannot be resolved by a light microscopy. Here, λ denotes the wavelength of light, and n is the refractive index of the sample medium (ideally also immersion medium of the microscope objective). The numerical aperture $\mathrm{NA} = n \sin \Theta$ was already mentioned earlier, where Θ is the half angle of light collection of the objective (see figure 2.9).

NA values of modern objectives can achieve values of up to 1.6 when using sapphire cover slides and special objectives. But even then, the achievable resolution is limited by ~ 150 nm at visible wavelengths in the range of 400-700 nm. For example, assuming a wavelength of 500 nm and a NA of 1, the Abbe limit is ≈ 250 nm for the lateral resolution.

For the axial resolution of an optical microscope, one can derive an expression very similar to the lateral resolution limit of Abbe:

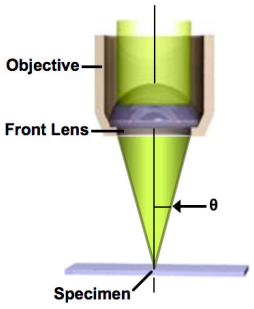

Abb. 2.9: Simple schematic of the objective. Excitation laser beam fills the back aperture of the objective where the light is then focused onto the sample (diffraction-limited).(Source nikon website)

$$z_{min} = \frac{\lambda}{n\,(1 - \cos\Theta)} \tag{2.21}$$

which gives of our example values a resolution of approximately 700 nm, roughly three times worse than the lateral resolution.

The past 30 years have seen a revolution of optical microscopy with the invention of super-resolution microscopy that dramatically overcomes the diffraction limit or optical resolution. These super-resolution techniques have increased the lateral and axial resolution by orders of magnitude beyond the diffraction limit. Among them is the family of methods called single-molecule localization microscopy (SMLM), in particular photoactivation localization microscopy (PALM) [10], stochastic optical resolution microscopy (STORM) [117], fluorescence PALM (fPALM) [52], direct STORM (dSTORM) [143], or points accumulation for imaging in nanoscale topography (PAINT) [127]. SMLM uses the fact that the center position of a single molecule's image can be determined with much higher accuracy than the size of that image (point spread function) itself. However, a big challenge of SMLM is to achieve super-resolution also along the optical axis (three-dimensional imaging), i.e. to localize an emitter not only laterally but also along the optical axis. Various techniques have been invented for doing this, the most popular being astigmatic imaging [56], bi-plane imaging [60], or helical wave-front shaping [104]. However, all these methods yield an axial localization accuracy that is typically by a factor 3 to 5 worse than their lateral counterpart. The only exceptions are interference-based methods [130, 4], but for the prize of an elevated technical complexity of the required setup.

An alternative and relatively simple approach for achieving superior axial resolution is MIET, which provides exceptional axial resolution using fundamental physics [21, 45]. The localization accuracy of MIET depends on how precisely the fluorescence lifetime τ can be measured. In the ideal case of a background-free measurement, this accuracy $\Delta\tau$ is inversely proportional to the square root of the number N of detected photons, or more precisely it is given by

$$\Delta\tau = \frac{\tau}{\sqrt{N}} \tag{2.22}$$

A second important factor of the achievable axial resolution in MIET is how steep the dependence between lifetime and distance is. For metals (gold, silver), the lifetime will increase from zero to roughly its free-space value over a distance of 150-200 nm. When replacing the metal layer with a single sheet of graphene, this distance range is reduced to $\sim$20 nm, yielding a ca. ten-fold improvement in axial resolution.

After having presented in this chapter a brief overview and discussion of the optical resolution in fluorescence microscopy, I will discuss in the next chapter the method of fluorescence correlation spectroscopy (FCS) which will be used for measuring lipid diffusion in SLBs.

5 Fluorescence correlation spectroscopy

Fluorescence correlation spectroscopy (FCS) is a highly sensitive fluorescence-spectroscopic technique that works at picomolar to nanomolar fluorescent sample concentrations. This technique was first experimentally introduced by Magde, Elson and Webb in 1972 [83] for studying the reversible binding of ethidium bromide (EtBr) with DNA. In their publication, they used FCS to measure diffusion of the fluorescent species and the kinetics of this reaction. The technique was further developed for quantitative measurements diffusion, biochemical interactions, and absolute concentrations. But it was not until the early 1990 that the technique attracted again considerable attention and found wide application in the life sciences, chemistry and physics. This was initiated by the work of Rigler et al. in 1993 [111], which created quite an impact and pushed the technique to the single molecule level. Introduction of confocal microscopy to this technique led to a number of improvements: it provided better signal-to-noise ratio, and smaller and better defined detection volume.

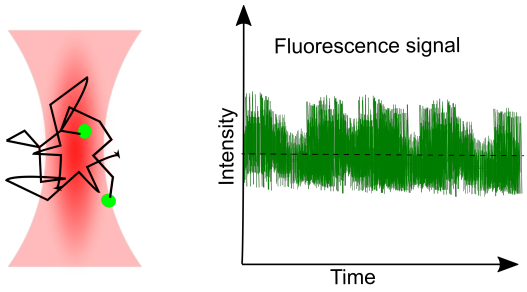

Abb. 2.10: Schematic of a typical FCS experiment. Fluorescent molecules (green dots) diffuse in and out of the small detection volume (deep-red region) of a confocal microscope. Due to the changing number of fluorescent molecules in the detection volume, the fluorescent intensity exhibits significant fluctuation if the concentration of fluorescent molecules is sufficiently small.

In FCS, one records fluorescent intensity fluctuations caused by the diffusion of fluorescent molecules in and out of the detection volume of a confocal microscope, as illustrated by figure 2.10. The detection volume is the region in the sample where fluorescence is efficiently excited and detected. Any process that induces fluorescence intensity fluctuation such as the diffusion of molecules, chemical reactions, photophysical transitions, or conformational

changes, can be observed with this technique. Interestingly, the amplitude of the fluorescence signal fluctuation is inversely proportional to the sample concentration. From the measured intensity time traces, one then calculates the so-called Autocorrelation Function (ACF) $g(\tau)$ which is the correlation of the recorded fluorescence intensity time trace with a time-shifted replica of itself, computed at all possible time shift values τ (lag times):

$$g(\tau) = \langle I(t)I(t+\tau)\rangle_t \tag{2.23}$$

where $I(t)$ and $I(t+\tau)$ are the fluorescence intensities at time t and $t+\tau$, respectively. The brackets denote averaging over all time values t. The physical interpretation of the 2.23 is that the autocorrelation function $g(\tau)$ describes the probability of detecting a photon at time $t+\tau$ if there was a photon detection at time t. This implies two possibilities: (1) the photons detected at time t and $t+\tau$ originate from the same fluorescing molecule; or (2) the photons originate from two different molecules. Only in the first case there can be a physical correlation between the photons. Photons obtained from two different molecules will only contribute a constant offset to the ACF.

The measured signal $I(t)$ has contributions from the fluorescence of the molecules as well as from uncorrelated background I_{bg}, the background including electronic noise or light scattering. Thus, the total intensity reads

$$I(t) = I_{bg} + \sum_j I_j(t) \tag{2.24}$$

where I_j refers to the fluorescence of the j^{th} molecule, and the summation extends of all N molecules in a sample. Using this relation, the autocorrelation function is calculated as

$$\begin{aligned} g(\tau) &= \sum_j \langle I_j(t)I_j(t+\tau)\rangle \\ &= N\langle I_1(t)I_1(t+\tau)\rangle + N(N-1)\langle I_1\rangle^2 + 2N\langle I_{bg}\rangle\langle I_1\rangle + \langle I_{bg}\rangle^2 \\ &= N\langle I_1(t)I_1(t+\tau)\rangle + N(N-1)\langle I_1\rangle^2 \end{aligned} \tag{2.25}$$

where we have taken into account that the fluorescence of all molecules is statistically similar (denoted by I_1 in the second and third line of the above equation) and independent from each other.

As an example, consider an example that a molecule at some time t at the centre of the detection volume. Then, the probability to detect photons from this molecule is high. This corresponds to a highly correlated fluorescence signal over time. When the molecule gradually diffuses out of the detection volume, this probability will continuously decrease, and the correlation is eventually lost when the molecule exits the detection volume. This loss of correlation will depend on the diffusion speed of the molecule, i.e the faster the diffusion speed of a molecule, the faster the correlation decays. Thus, a faster correlation decay of an ACF indicates a larger diffusion coefficient.

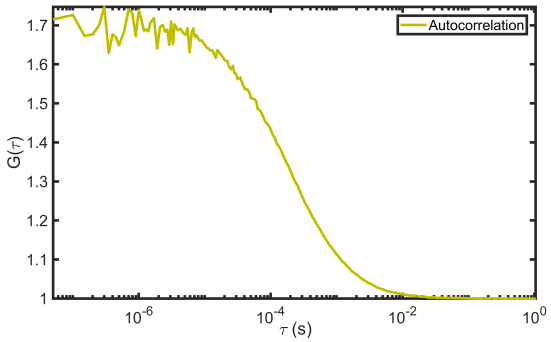

Abb. 2.11: Normalized autocorrelation curve of the dye Atto655 in aqueous solution. The ACF decay is due to translational diffusion.

An autocorrelation curve provides several information about fluorescent molecules in a sample. Firstly, the amplitude of an ACF is inversely proportional to the concentration of fluorescing molecules (average number of molecule within the detection volume). Secondly, the temporal decay of the ACF provides information about different properties of the fluorescent sample. On the nanosecond timescale, photon antibunching and rotational diffusion dynamics can be observed. The anti-correlation of an ACF at timescales of the fluorescence lifetime is due to the delay between photon emission and re-excitation of a fluorescent molecule and is termed photon antibunching. It is observed as a steep decrease in $g(\tau)$ on the nanosecond timescale. If the experiments are performed with polarised excitation and/or detection using polarization filters, the rotational diffusion will be visible in the ACF as a partial correlation decay on the nanosecond timescale. Next, fast photophysical transitions such as intersystem crossing to the triplet state or fast intramolecular structural dynamics contribute to the microsecond temporal

decay of $g(\tau)$. On a millisecond to the second timescale, the temporal decay of the autocorrelation function is due to the translational diffusion of the molecules moving out of the detection volume, see also figure 2.11.

Over time, FCS has become an important tool for studying binding interactions, enzymatic activities, chemical kinetics, cis-trans isomerizations, or conformational dynamics. Most other methods that are used for measuring diffusion coefficients such as dynamic light scattering (DLS), pulsed field gradient NMR (nuclear magnetic resonance), or size exclusion electrophoresis, have to work at high sample concentration. This poses a challenge for many biological applications such as measurement of protein samples that are prone to aggregation.

However, for precise measurements of diffusion coefficients with FCS, a precise knowledge of the shape and size of the detection volume, or more precisely of the molecule detection function (MDF), is required. The MDF is a three-dimensional function of molecule position which describes how well fluorescence is excited and detected for a molecule at a given position. In conventional FCS, the detection volume can be determined by calibrating a setup with a standard dye solution of known diffusion. Many advanced versions of FCS has been proposed that introduce an external ruler, which precisely defines the detection volume of a setup. Among these methods are dual-focus FCS (2fFCS) and scanning FCS, which both come with an internal length calibration.

In 2fFCS, two laterally shifted excitation/detection volumes are generated with a well-defined distance between them. The MDFs of these excitation/detection volumes are well defined using a simple two-parameter model. The *a priori* knowledge of the distance between the volumes allows for determining absolute values diffusion coefficients without any further calibration. Additionally, this technique is robust against variations of refractive index, cover-slip thickness, optical saturation effects, or laser beam astigmatism. Another important FCS variant as the above mentioned scanning FCS which I explain in detail in section 2.35. Here, the detection volume is moved over the sample, and knowledge of the speed motion introduces an external length scale into the FCS measurement. Additionally, scanning increases the statistics of an FCS measurement and thus improves the signal-to-noise ratio of an ACF.

Another extension of FCS that is important to mention here is fluorescence lifetime correlation spectroscopy (FLCS). FLCS combines fluorescence lifetime measurements with FCS to calculate lifetime-specific ACFs. This technique will be explained in detail in the next section 5.1. It will be crucial for calculating ACFs for the lipid diffusion in supported lipid bilayer in a leaflet-specific manner.

5.1 Fluorescence lifetime correlation spectroscopy (FLCS)

Fluorescence lifetime correlation technique is another sophisticated variant of FCS, which uses the fluorescence lifetime to obtain ACFs of individual fluorophore populations form a mixture of fluorophores that have distinct lifetimes [44, 13, 62]. In this method, each collected photon is weighted with a statistical filter function before calculating an ACF. This filter function is calculated from the nanosecond detection times of the photons relative to the excitation pulses of the laser (thus, FLCS requires a pulsed excitation source).

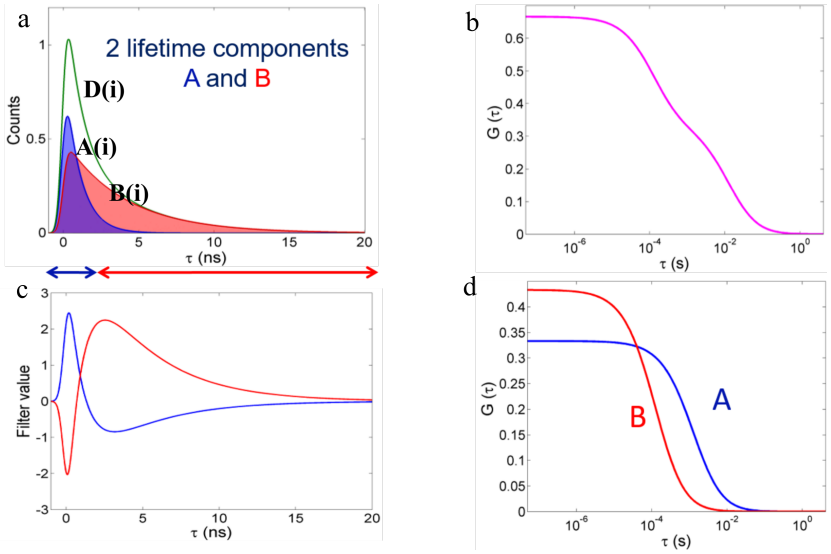

Abb. 2.12: ***(a)*** *D(i) is the measured TCSPC decay curve of a sample containing two distinct lifetime decay A and B (green). D(i) includes lifetime signature of both the components. The pure components A and B TCSPC histogram are shown by the decay curve A(i)(blue) and B(i)(red) respectively.* ***(b)*** *ACF obtained with standard FCS shows linear combination of the contributions from both the components A and B.* ***(c)*** *Filter function calculated for the component A(blue) and B(red). The positive value of filter function A shows its photons contribution in the initial channels is dominant whereas the positive value of B in later time scales depicts component B contribution in longer lifetime.* ***(d)*** *Lifetime specific ACFs calculated for the component A and B by weighing each photon with the values of these filter functions according to their TCSPC channel number.*

As a simple example, consider a sample containing a mixture of two distinct fluorescent decay components, A and B. When using standard FCS, the

resulting ACF is a linear combination of the contributions from both the components. Figure 2.12 shows the fluorescence TCSPC decay histograms, where component A decays within the first 200 TCSPC channels (short fluorescence lifetime), while component B extends over a longer time range (long fluorescence lifetime). Let us denote the probabilities to detect a photon in the i^{th} TCSPC channel for components and A and B by $A(i)$ and $B(i)$. Typically, i ranges from 1 to N, where N is on the order of 100-1000. A measured TCSPC decay of such a sample has contributions from both the components, shown a decay $D(i)$ in figure 2.12. To separate these contributions of each component, one needs to deconvolve the measured histogram. In order to deconvolve $D(i)$, one needs *prior* knowledge of the characteristic decay curve of the individual components ($A(i)$ and $B(i)$ in the figure). This knowledge can be obtained either from separate TCSPC measurement of the pure components, or from a $D(i)$ decay curve analysis. The normalized decay curves $a(i)$ and $b(i)$ are given by

$$a(i) = \frac{A(i)}{\sum A(i)} \qquad b(i) = \frac{B(i)}{\sum B(i)} \tag{2.26}$$

are named the decay patterns. Thus, the measured signal $I(i,t)$ at macrotime t in TCSPC channel i decay curve $D(i)$ of the mixture is expressed by

$$I(i,t) = w_a(t)a(i) + w_b(t)b(i) \tag{2.27}$$

where $w_a(t)$ and $w_b(t)$ are the relative fluorescence intensities from component A and B at macrotime t, respectively, and the index i refers to the i^{th} TCSPC channel. In the above equation, two different time scales are involved: macroscopic time scale t that determines the global arrival times of the photon with respect to the start of the experiment, and the microscopic time scales i that tells a photon's detection time with respect to the last excitation laser pulse. Both times are recorded by the TTTR mode of photon registration, while the microtime i (TCSPC channel) is used for calculating fluorescence decay histograms, whereas the macrotime t is used for the calculation of the auto- and cross-correlation functions (ACFs and CCFs). The ACF/CCF of and between the individual lifetime components are then defined as

$$g_{ab}(t) = \langle w_a(t_0)w_b(t_0+t)\rangle_{t_0} \tag{2.28}$$

The question is how to extract the individual intensities $w_{a,b}(t)$ from the compound signal. Rewriting equation 2.27 in matrix notation we get

$$\mathbf{I}(t) = \hat{\mathbf{M}} \cdot \mathbf{w}(t) \tag{2.29}$$

where $\mathbf{I}$ is the column vector of the combined decay curve with elements $I(i,t)$, and $w(t)$ is the column vector with elements w_a. The matrix M is given by $M_{ia} = a(i)$ for component A and $M_{ia} = b(i)$ for component B, and it has as much columns as there are TCSPC channels i, and as much rows as there are different decay components (in our equations above, there are only two decay components, but the concept can be generalized to arbitrary many). The values of $w_a(t)$ and $w_b(t)$ are then found by minimizing the quadratic form

$$(\mathbf{I} - \hat{\mathbf{M}} \cdot \mathbf{w})^\top \cdot \hat{\mathbf{V}}^{-1} \cdot (\mathbf{I} - \hat{\mathbf{M}} \cdot \mathbf{w}) \tag{2.30}$$

where $^\top$ denotes matrix (vector) tranposition, and V is the covariance matrix

$$\begin{aligned} \hat{\mathbf{V}} &= \left\langle (\mathbf{I} - \hat{\mathbf{M}} \cdot \mathbf{w}) \cdot (\mathbf{I} - \hat{\mathbf{M}} \cdot \mathbf{w})^\top \right\rangle - \left\langle \mathbf{I} - \hat{\mathbf{M}} \cdot \mathbf{w} \right\rangle \cdot \left\langle \mathbf{I} - \hat{\mathbf{M}} \cdot \mathbf{w} \right\rangle^\top \\ &= \operatorname{diag} \langle \mathbf{I} \rangle \end{aligned} \tag{2.31}$$

The angular brackets denote time averaging over an infinitely long measurement, and the last line in the last equation results from the Poissonian statistics of photon detection in each TCSPC channel. When minimizing the last equation, one finds an expression for the vector $\mathbf{w}$ via a weighted quasi-inverse matrix as

$$\mathbf{w} = \left(\hat{\mathbf{M}}^\top \cdot \operatorname{diag} \langle \mathbf{D} \rangle^{-1} \cdot \hat{\mathbf{M}} \right)^{-1} \cdot \hat{\mathbf{M}}^\top \cdot \operatorname{diag} \langle \mathbf{D} \rangle^{-1} \cdot \mathbf{D} = \hat{\mathbf{F}} \cdot \mathbf{D} \tag{2.32}$$

where $\hat{\mathbf{F}} = \left(\hat{\mathbf{M}}^\top \cdot \operatorname{diag} \langle \mathbf{D} \rangle^{-1} \cdot \hat{\mathbf{M}} \right)^{-1} \cdot \hat{\mathbf{M}}^\top \cdot \operatorname{diag} \langle \mathbf{D} \rangle^{-1}$ is the filter function that can now be used to calculate the contributions $w_a(t)$,$w_b(t)$ of the different component's intensity to each TCSPC channel $D(i)$,

$$w_a(t) = \sum_{i=1}^{N} F_a(i) D(i)(t) \tag{2.33}$$

Here, $\hat{\mathbf{F}}$ is a $2 \times N$ matrix, with elements $F_a(i)$ and $F_b(i)$. These calculated filter functions form a dual orthogonal basis to the decay patterns (see figure 2.12).

Using these filter functions, the auto- and cross-correlations are calculated as

$$g_{ab}(t) = \sum_{i=1}^{N} \sum_{j=1}^{N} F_a(i) F_b(j) \langle D_i(t_0 + t) D_j(t_0) \rangle_{t_0} \tag{2.34}$$

FLCS has several advanced applications where changes in biomolecular conformation induce lifetime changes. FLCS is an important technique for this thesis where I use it in conjunction with MIET for the calculation of leaflet-dependent autocorrelation functions.

5.2 Line scanning-FLCS

Line-scanning fluorescence lifetime correlation spectroscopy combines line-scanning FCS with FLCS. FLCS has been already discussed in detail in the previous section. Here, I will focus on line-scanning FCS. As mentioned earlier, scanning FCS is a calibration-free technique, i.e it does not require a separate quantification of the detection volume. Additionally, this technique solves many other problems associated with conventional single-focus FCS, such as statistical inaccuracies, long measurement times for slow diffusing molecules, photobleaching, or the impact of optical aberrations.

Measuring the lateral diffusion of fluorophores in a membrane by using conventional FCS has become quiet challenging due to the slow diffusion times which can reach several milliseconds. In contrast, fluorophores in solution exhibit diffusion times of ~ 150 μs. That the diffusion in membranes is one to two orders of magnitude slower than in solution poses problems for acquiring sufficient signal for obtaining a decent FCS curve, because there are not enough fluctuations sampled within reasonable measurement times. In order to improve the signal-to-noise ratio of the acquired data, long measurement times have to be employed. This does dependent further on the stability of the optical setup. The option of using higher excitation power is should be avoided to reduce the chances of photobleaching.

The above mentioned problems can be solved by moving the detection volume across the sample. This results in a reduction of the residence time of a fluorophore, but also increases the sampling statistics. Instead of a point measurement, an array of points along the line is measured. The additional knowledge of the scan parameter provides an external ruler for the detection volume (area) calibration. Moreover, higher laser power can be used without risking photobleaching artifacts, because the laser power is distributed over the entire scan line.

A moving detection volume can be achieved by using a laser scan unit. For example, the state-of-the art FLIMbee galvo scanner of PicoQuant GmbH (Berlin) provides maximum scan speeds of 2 kHz. For line-scan FCS, the detection volume is moved linearly across a membrane with a constant velocity v. As demonstrated in the figure, the detection volume is sequentially scanned along a line. On stacking the line scans i vertically, a pseudo image

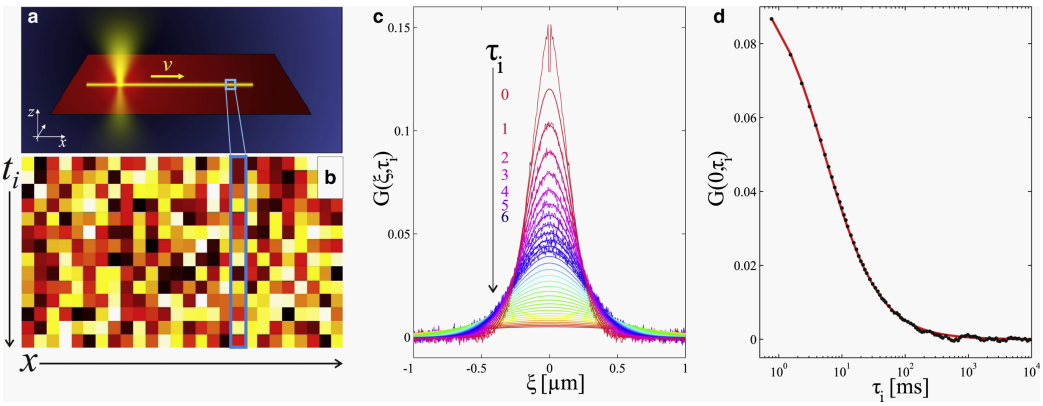

Abb. 2.13: Schematic of line-scan FCS. ***(a)*** *A horizontal line is scanned repeatedly with scan velocity v.* ***(b)*** *Pseudo-image depicting all the scanned lines where the vertical axis shows the time and the horizontal axis represents the length of line consisting of N pixels.* ***(c)*** *The two-dimensional plot shows the spatial and temporal correlation curve $G(\xi, \tau_i)$. The spatial correlation is shown along the horizontal axis and the temporal correlation is coded by color (see color bar).* ***(d)*** *The temporal correlation obtained from a column of the pseudo image. Figure from ref. [110]*

$F(x, t_i)$ can be constructed (see figure 2.13b where the horizontal axis is the scan position along a single line scan, and along the vertical axis different line scans are stacked). The position of the laser focus in the sample runs along the horizontal axis. Moreover, the vertical axis can be given in time $t_i = i \cdot T$, where T is the scan period. A conventional FCS temporal correlation curve $G(0, \tau_i)$ is obtained by correlating the intensity at the same position (horizontal axis) over different lag times (vertical axis in the pseudo image). Due to the scanning, the intensity $F(x, t_i)$ is recorded at time $t_i + x/v$, where v is the scan speed and x denotes the position in the sample. This includes information about the diffusion times and the photophysics of the fluorophore. Additionally, one can correlate pixel intensities between adjacent positions along the horizontal line, which results spatial correlations. Most generally, one obtains the two-dimensional spatio-temporal correlation function as

$$G(\xi, \tau) = \frac{\langle \delta F(x, t_i) \delta F(x + \xi, t_i + \tau) \rangle}{\langle F(x, t_i) \rangle^2} \tag{2.35}$$

where ξ is the spatial lag and τ the the time lag of the correlation.

5.3 Membrane adsorption/desorption model

In this subsection, I will briefly describe the model used in this thesis for fitting the autocorrelation functions obtained from measurements of lipid diffusion in supported lipid membranes. The model takes into account the influence of the support/substrate on the diffusion of a molecule within supported lipid bilayer or any planer layer within the proximity of a surface. Considering a molecule that can undergo reversible adsorption and desorption to and from the surface that supports the planar bilayer. A similar model for this situation was worked out in refs. [29, 74]. These publications presented a model for three-dimensional diffusion of a molecule above a surface while it can undergo adsorption and desorption kinetics to the surface.
Let us start to consider a kinetic system of two populations represented by A and B and which describe freely diffusing molecules (A) and molecules that are adsorbed on the surface (B). The corresponding kinetic reaction scheme reads

$$A \underset{k_-}{\overset{k_+}{\rightleftharpoons}} B \tag{2.36}$$

Let $a(\mathbf{r}, t)$ be the probability density to find a freely diffusing molecule at position $\mathbf{r}$ and time t, and let $b(\mathbf{r}, t)$ be the corresponding probability density that a molecule is adsorbed at position $\mathbf{r}$ and time t. The evolution equations for these functions $a(\mathbf{r}, t)$ and $b(\mathbf{r}, t)$ are given by

$$\begin{aligned} \frac{\partial a}{\partial t} &= D\Delta a - k_+ a + k_- b \\ \frac{\partial b}{\partial t} &= k_+ a - k_- b \end{aligned} \tag{2.37}$$

where D is the diffusion coefficient, Δ represents the two-dimensional Laplace operator, k_+ and k_- are the rate constants of adsorption and desorption, and we have $a + b = 1$. We are interested in finding the probability density $p(\mathbf{r} - \mathbf{r}_0, t)$ to find *any* molecule at position $\mathbf{r}$ at time t if it was at position $\mathbf{r}_0$ at time zero. This is given by the sum $a(\mathbf{r}, t) + b(\mathbf{r}, t)$ after we have solved eqs. (2.37) with the initial conditions

$$a(\mathbf{r}, t = 0) = \frac{k_-}{k_+ + k_-} \delta(\mathbf{r} - \mathbf{r}_0) \tag{2.38}$$

and

$$b(\mathbf{r}, t=0) = \frac{k_+}{k_+ + k_-}\delta(\mathbf{r} - \mathbf{r}_0)$$

which means that we assume kinetic equilibrium between free and adsorbed molecules at time zero, i.e. $\partial a(\mathbf{r}, t=0)/\partial t = 0$ and $\partial b(\mathbf{r}, t=0)/\partial t = 0$. By applying a Fourier transform to eqs. (2.37), we then obtain the following expression for the Fourier transform $\tilde{p}(\mathbf{q}, t)$ of $p(\mathbf{r}, t)$

$$\begin{aligned}\tilde{p}(\mathbf{q}, t) = &\frac{(k_+ + k_-)(k_+ + k_- + 2\Delta) + (k_+ - k_-)Dq^2}{4(k_+ + k_-)\Delta} e^{-(\lambda+\Delta)t - i\mathbf{q}\mathbf{r}_0} \\ - &\frac{(k_+ + k_-)(k_+ + k_- - 2\Delta) + (k_+ - k_-)Dq^2}{4(k_+ + k_-)\Delta} e^{-(\lambda-\Delta)t - i\mathbf{q}\mathbf{r}_0}\end{aligned} \tag{2.39}$$

where $\mathbf{q}$ is the Fourier coordinate conjugated to $\mathbf{r}$, and λ and Δ are the following abbreviations

$$\lambda = \frac{k_+ + k_- + Dq^2}{2} \tag{2.40}$$

and

$$\Delta = \sqrt{\lambda^2 - Dq^2 k_-}. \tag{2.41}$$

Transforming eq. (2.39) back to real space then yields an explicit expression for $p(\mathbf{r} - \mathbf{r}_0, t)$. Knowing this function, one can then express the spatio-temporal fluorescence correlation function as

$$G(\xi, \tau) = G_\infty + \kappa^2 c_0 \int d\mathbf{r} \int d\mathbf{r}_0 U(\mathbf{r} - \xi\hat{\mathbf{e}}_x) p(\mathbf{r} - \mathbf{r}_0, \tau) U(\mathbf{r}_0) \tag{2.42}$$

where κ is proportional to the molecular brightness of the dye labels, c_0 is the label concentration (molecules per area), G_∞ is an uncorrelated offset for infinity spatial and/or temporal lag, and $U(\mathbf{r})$ is the probability density for exciting and detecting a dye at position $\mathbf{r}$, and which is assumed to be a rotationally symmetric Gaussian distribution,

$$U(\mathbf{r}) = \exp\left(-\frac{2r^2}{w^2}\right) \tag{2.43}$$

where w is the radial size of the two-dimensional excitation/detection spot. In eq. (2.42), the integrations over $\mathbf{r}$ and $\mathbf{r}_0$ extend over the infinite two-dimensional plane, and it is assumed that the scan directions is along the

horizontal x-axis (along unit vector $\hat{\mathbf{e}}_x$). Combining eqs. (2.39) and (2.42), we arrive at the final result for the line-scan FCS curve for two-dimensionally diffusing molecules with adsorption/desorption kinetics

$$\begin{aligned} G(\xi,\tau) = G_\infty + \kappa^2 c_0 \int_0^\infty dq q J_0(q\xi) \exp\left(-\frac{q^2 w^2}{2}\right) \\ + \Big[\frac{(k_+ + k_-)(k_+ + k_- + 2\Delta) + (k_+ - k_-)Dq^2}{4(k_+ + k_-)\Delta} e^{-(\lambda+\Delta)\tau} \\ - \frac{(k_+ + k_-)(k_+ + k_- - 2\Delta) + (k_+ - k_-)Dq^2}{4(k_+ + k_-)\Delta} e^{-(\lambda-\Delta)\tau}\Big] \end{aligned} \tag{2.44}$$

where J_0 is the zeroth Bessel function of the first kind. This expression cannot be simplified further, and when using it for fitting experimental data, the integration over q has to be done numerically, which is straightforward and fast with modern computers.

CHAPTER 3

Lipid diffusion in a supported lipid bilayer

Two-dimensional membrane models have always assumed that the lateral lipid diffusion in the top and bottom leaflets is equal. This has been set as a principle behind all diffusion studies in membranes until now. This is a simplifying assumption of the real membrane system and is due to the difficulties to resolve the diffusion in the two closely spaced leaflets using available techniques such as FCS, FRAP, or SPT.

Especially for supported lipid bilayers where this may not be the case because the bottom leaflet is divided from the substrate by only a ∼1-2 nm thin hydration layer, so that one may expect that the substrate impacts the mobility of lipids in the bottom leaflet. As compared to the top leaflet which has no such direct interactions, the diffusion behavior might be very different. To better understand membranes and their role in various processes, an in-depth three-dimensional picture of membrane fluidity and diffusivity is crucial. MIET/GIET is one methodological approach to gain such knowledge and to study three-dimensional membrane organization and insight into the intricate membrane dynamics.

The core idea is to use MIET/GIET for axially localizing labelled lipids in a SLB, and to use sFLCS to obtain leaflet-dependent lipid diffusion coefficients. For that purpose, a lifetime-specific correlation analysis (FLCS) was applied to the recorded data that results in ACFs for each leaflet. In this thesis, I have

used coverslips coated with the transparent semi-conducting material indium tin oxide (ITO) for inducing the distance-dependent quenching as required for MIET. Later, I have switched to single-sheet graphene for a similar study. Several control experiments were performed to support the FCS results, in particular performing measurements on samples where only the top leaflet is labelled, or where the fluorescence of labels in the top leaflet is quenching by adding the quencher potassium iodide (KI) to the solution. Also, I tried rapid imaging of fluorescent lipid motion and single-molecule burst studies for directly accessing lipid diffusivity.

Part of this work is already published in the publication "Graphene-based metal-induced energy transfer for sub-nanometre optical localization" [45].

1 Methods and Experimental setup

MIET Substrate preparation

Indium Tin Oxide substrate (ITO): Indium Tin Oxide coated glass coverslips, 22 mm x 22 mm, thickness 0.13-0.17 mm were purchased from SPI supplies (West Chester, U.S.A). 4 nm thick SiO_2 spacer was vapour deposited on the ITO substrate.

Graphene substrate : Glass coverslips, 24 mm $\times$ 24 mm, thickness 170 μm (Menzel, Germany) were plasma cleaned and coated with a single sheet of graphene (0.34 nm thickness). The graphene coatings were provided by the Graphene Supermarket, New York, USA. SiO_2 spacer of 10 nm thickness was later deposited on these substrates by evaporation using an electron beam source (Univex 350, Leybold) under high vacuum conditions (10^{-5} mbar). The deposition was performed at the slowest rate (1 $Å s^{-1}$) to obtain maximal homogeneity. The evaporation process was monitored using an oscillating quartz unit. The silica spacer is used to avoid the direct interaction of the dye with the metal/graphene surface. In the case of no spacer, will lead to high quenching of the dye and hence no MIET can be observed. The spacer deposition on the metal/graphene was performed by Arindam Ghosh and Alexey Chizhik.

Chemicals & **reagents :** 1,2-dioleoyl- sn - glycero- 3- phosphocholine (18: 1 (Δ9-Cis) PC (DOPC)), 1- palmitoyl- 2- oleoyl- sn - glycero- 3- phosphocholine (16: 0-18: 1 pc (POPC)) chloroform or 1,2-dilauroyl-sn-glycero-3-phosphocholine (DLPC) and a Mini-Extruder were purchased from Avanti, USA. Headgroup labelled lipids, 1,2- dihexadecanoyl- sn - glycero- 3- phosphoethanolamine (DPPE)- Atto655 and 1,2- dilauroyl- sn- glycero- 3- phosphoethanolamine (DLPE) - Atto655 were bought from ATTO-TEC GmbH, Siegen, Germany. These lipids were stored at -20°C in chloroform and infused with inert gas (Argon) to prevent oxidation at all times. Following combinations of lipids and fluorescent dye attached lipids were taken in SLB preparation are listed in table 3.1.

Phosphate buffered saline (PBS) at a pH of 7.4 using Milli-Q water (filter system by Millipore Corp.,USA) or Tris buffer, 20 mM Tris-Cl, 100 mM NaCl, 10 mM $CaCl_2$, pH 7.4 were used as solvents. The immersion oils

Lipid	headgroup labeled-lipid
DOPC	Atto655-DPPE
POPC	Atto655-DMPE
DLPC	Atto655-DLPE

Table 3.1: Combination of lipids used in this thesis.

for the objectives were used from Zeiss, Germany and the silicon adhesive incubation wells were by Ibidi 80469, Germany.

Supported lipid bilayer preparation

Following are the methods of the bilayer preparation used throughout this thesis.

Vesicle Deposition: Supported lipid bilayers were prepared by fusing vesicles on the solid substrate. DOPC, POPC and DLPC were dissolved in chloroform at a concentration of 10 mg ml^{-1} and the labelled lipids were diluted to 0.01 mg ml^{-1} concentration.

Small unilamellar vesicles (SUVs, diameter ∼50 nm to 100 nm) composed of a mono-component lipid (DOPC, POPC or DLPC) were used. 80 μl of DOPC was mixed with 1 μl of labelled lipid (Atto655-DPPE). The solution was vacuum dried at 30°C for 1 h to evaporate the solvent and obtain a dry lipid film. The film was then rehydrated with 500 μl of buffer solution, followed by 5 min of swelling and 1 min of vortexing. The vial was shaken for 1 h at 1400 rpm at 30°C in a thermomixer (Thermomixer Comfort, Eppendorf). This results in the formation of multilamellar vesicles, which were then extruded through a polycarbonate membrane of pore size 50 nm (Whatman, USA) to obtain SUVs. This process shears off the multiple layers to obtain a clear solution of unilamellar vesicles. Extrusion was performed for a minimum of 31 cycles with a constant force to ensure uniform size distribution of the vesicles of an average diameter equal to the pore size. These vesicles were stored at 4°C for up to 3 days when not used immediately. The resulting vesicle solution was diluted 30 times, and 60 μl of the vesicle solution was then left to incubate on the substrate containing silicon adhesive incubation well. The incubation was allowed for 1 hour so that a sufficient number of vesicles could fuse to form a uniform bilayer. This was followed by carefully rinsing with the buffer solution (PBS or Tris) at least 40 times in opposite

directions to remove unbound vesicles. The protocol was followed for all bilayer preparations using SUVs.

In the case of rapid imaging experiments, the amount of labelled lipids was reduced to 0.3 μl for the SUV preparation which was then used for recording the videos. Single burst experiments were performed with 50 nM dye label concentration.

Langmuir-Blodgett bilayer preparation : DOPC bilayers were prepared using a Langmuir-Blodgett (LB) system from the group of Claudia Steinem in the Chemistry Department of the Georg August University, Göttingen, with the help of technical lab assistant Jutta Gerber-Nolte. The LB trough was thoroughly cleaned with mucasol and several cycles of Milli-Q water. 120 μl of water was filled into the trough and the substrate was immersed into it. The setup was calibrated with the feather suspended in it such that it touches the water surface and the pressure was optimised to 0. The feather suspended in the air was corrected to a value of 72.5 $\mathrm{mNm^{-1}}$ until the setup was stabilised. A lipid solution consisting of DOPC and Atto-655-DPPE was prepared to the final concentration of 2 $\mathrm{mgml^{-1}}$. 25 μl of the lipid solution was taken with a syringe and the predetermined pressure was set to 40 $\mathrm{mNm^{-1}}$ for monolayer formation. A small droplet of the lipid solution was placed on the surface gently such that the lipid spreads on the air-water interface and a thin layer of lipids were formed due to hydrocarbon acyl chains that anchor the molecules to the interface. Droplets were added until the pressure reached a value of 4 $\mathrm{mNm^{-1}}$ and the system was left to equilibrate. After reaching equilibrium, the barriers were allowed to compress to obtain a highly compressed two-dimensional lipid monolayer at the interface. After letting the monolayer reach at a predetermined pressure (40 $\mathrm{mNm^{-1}}$), the substrate was vertically moved out of the water at a constant speed and pressure to obtain a uniformly deposited lipid monolayer. The substrate was dried overnight in a vacuum chamber and a second layer was prepared similarly. The only exception was that this time, the substrate was dipped into the trough after compressed monolayer formation (see figure3.1 [23]).

The formed lipid bilayer was not allowed to dry and the silicon adhesive chamber was stuck onto it while in solution to use it for epi-fluorescence microscopy.

Giant unilamellar vesicles : Giant unilamellar vesicles (>1 μm diameter)

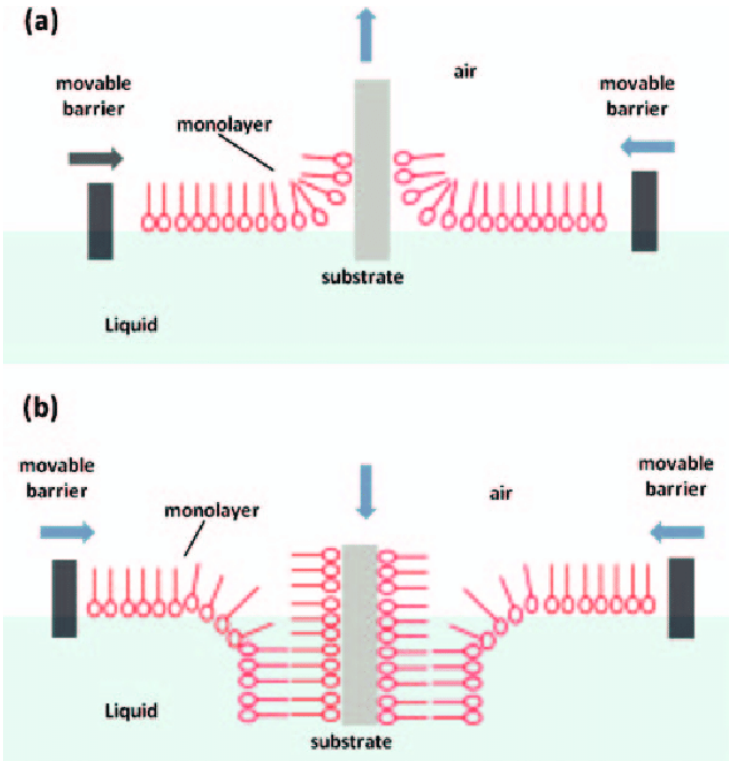

Abb. 3.1: Schematic of SLB preparation with the Langmuir-Blodgett (LB) technique. ***(a)*** *A lipid monolayer is first deposited on the hydrophilic substrate by controlled motion of the substrate through a monolayer formed on the aqueous surface.* ***(b)*** *Second layer is deposited on a hydrophobic surface by dipping the substrate into the aqueous solution. Figure taken from [23]*

were formed using a custom-built electro-formation chamber (see figure 3.2).

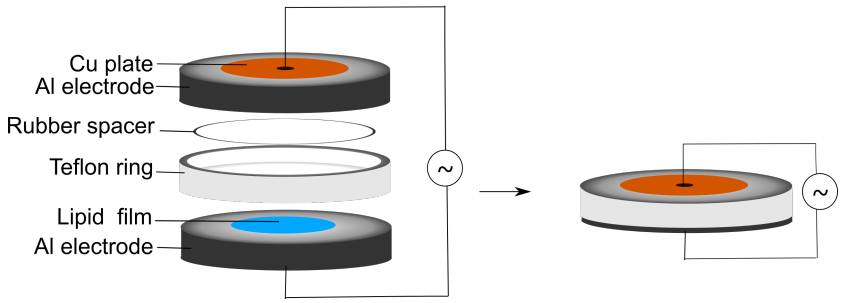

Abb. 3.2: Electro-formation chamber for GUV preparation. The chamber consists of two aluminium electrode surfaces which are placed on a Teflon ring. The electrodes are connected by a copper plate and an aluminium body. A sine-wave AC current of 15 Hz, $V_{pp} = 1.6$ V is applied by a HM 8030-2 function generator (Hameg, Germany).

For the preparation of Atto655-DPPE labelled DOPC GUV's, 98 μl of DOPC

lipid from the stock solution of 10 mgml^{-1} was taken with 2 μl of Atto655-DPPE. The labelled-to-unlabelled ratio (w/w) of the lipids was set to 1:49,000. The solution was dried on the lower aluminium electrode in vacuum at 30°C to obtain a lipid thin film. The film was then rehydrated with 500 μl of a 300 mM sucrose solution. The chamber was closed and connected to 15 Hz alternating current (AC) for 3 h with a peak-to-peak voltage of 1.6 V followed by a lower frequency (8 Hz) for 30 min to detach the formed vesicles from the electrode surface. The resulting GUV solution was then diluted with 500 μl glucose solution while rinsing the electrode surfaces, and the final GUV solution was collected.

ATTO 655 is the preferential dye of choice due to its high fluorescence quantum yield and photo-stability for single-molecule detection experiments.

Experimental setup: All scanning-FLCS measurements in this thesis were performed on a home-built confocal laser scanning microscope shown in figure 3.3. A linearly polarised pulsed excitation laser (LDH-D-C-640, PicoQuant, Germany) of wavelength 640 nm is coupled into a polarization-maintaining single-mode optical fibre (Schäfter + Kirchhoff). The output light from the fibre was collimated and reflected by a dichroic mirror (FITC/ TRITC, Chroma Technology) into the FLIMbee galvo-scanner (PicoQuant, Germany) where three galvo mirrors are used to scan the beam across the lateral xy-plane. The light was then directed to an inverted microscope (IX*71*, Olympus) and focused into the back-focal plane of an oil-immersion objective (UAPON 100× oil, 1.49 NA, Olympus). Using the objective, the light was focused into the sample, and the same objective was also used for collecting the emission light. The collected light was transmitted through the dichroic and focused by a tube lens on a 100 nm pinhole to block out-of-plane light. This largely reduced any background fluorescence. Finally, the fluorescence light was collimated and focused onto a single-photon avalanche diode (τ -SPAD, PicoQuant). A long-pass (F76-649, AHF) and a bandpass (BrightLine HC 692/40, Semrock) filter were placed in the collimated beam path for spectral cleaning. The SPADs were connected to a photon counting unit (HydraHarp 400, PicoQuant). It recorded the photon arrival times in time-tagged time-resolved (TTTR) mode with a resolution of 16 ps. The repetition rate of the laser was controlled by a laser driver (PDL 828 Sepia II, PicoQuant) and was set to 40 MHz for the sFLCS measurements which

were synchronized with the TCSPC electronics.

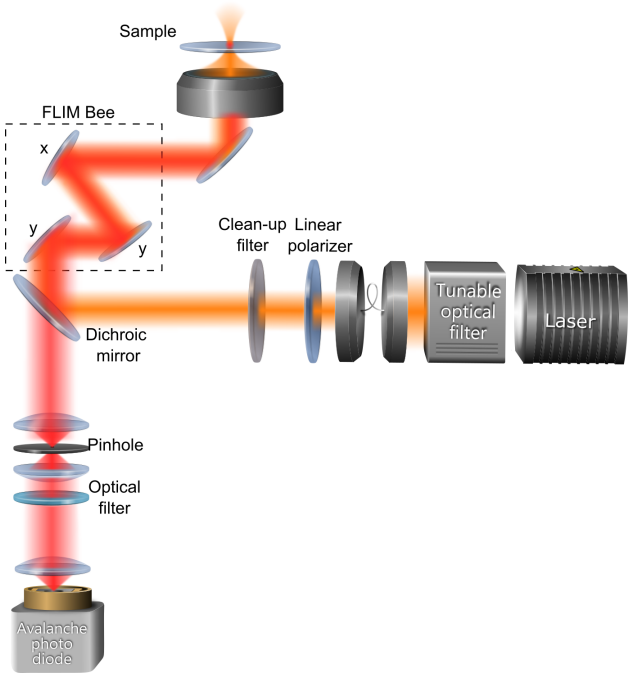

Abb. 3.3: Schematic of the confocal setup used for MIET experiments. The excitation laser path is shown in orange, and the emission from the sample is shown in red. A FLIMbee galvo-scanner (PicoQuant, Germany) was installed in the laser path for scanning the xy-plane.

For scan-FLCS measurement of the lateral lipid diffusion in a bilayer, fluorescence photons were recorded in TTTR mode. The arrival times of all recorded photons were histogrammed with a bin width of 16 ps, resulting in a time-correlated single-photon counting (TCSPC) decay curve. A line of 5 μm length consisting of 100 pixels was scanned along the x-direction (mono-direction). The line scan frequency was set to 2 kHz, and the dwell time was kept at 2.5 μs (demonstrated by figure 3.4). The quality of a bilayer during all measurements was determined by monitoring the FCS diffusion times (range of ≈1-5 ms) along with recording the fluorescence lifetime image (FLIM). The uniformity of the bilayers was checked from the FLIM image, and measurements were taken only in areas where the bilayer was found to be highly uniform. The presence of vesicles on the surface was detected by their lifetime in an FLIM image.

Data evaluation The data analysis was performed by using Matlab routines written by Daja Ruhlandt, Narain Karedla and Sebastian Isbaner. For

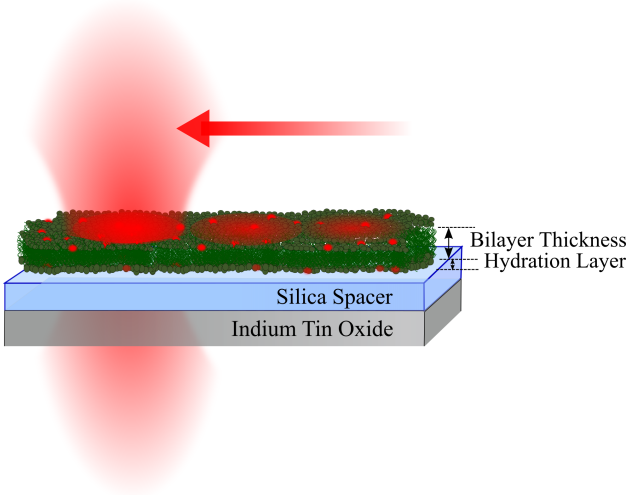

Abb. 3.4: Simple demonstration of laser scanning along x-direction on a SLB. The line scan speed is kept at a maximum of 2 kHz (mono-directional).

error calculations, at least three independent measurements were done on one sample to obtain the standard deviation, or for performing a bootstrap analysis where the data are randomly grouped in bunches of at least 10^6 photons.

2 Lipid diffusion in Supported lipid bilayer on glass

Preliminary experiments were performed on SLBs on glass, where I measured the diffusion of headgroup-labelled Atto655-DPPE lipid in a SLB of DOPC. All the diffusion experiments were performed on a confocal microscope equipped with TCSPC electronics (see chapter 3, section 1, for details). The SLBs were prepared by fusing 50 nm-sized vesicles on the glass surface. After 1 h of incubation, the sample was carefully rinsed with buffer solution to remove excess vesicles from the surface. The quality of the bilayer was checked by a point FCS measurement which resulted in diffusion times that were typically between 1-5 ms (for lipid diffusion in bilayer). An area of 60 μm×60 μm of the sample was scanned to check for surface heterogeneity or the presence of vesicles. Then, a sFCS measurement was started in a homogeneous intensity region as identified in a fluorescence intensity image.

Sufficiently long measurements of at least 2 h were taken to collect sufficient photons.

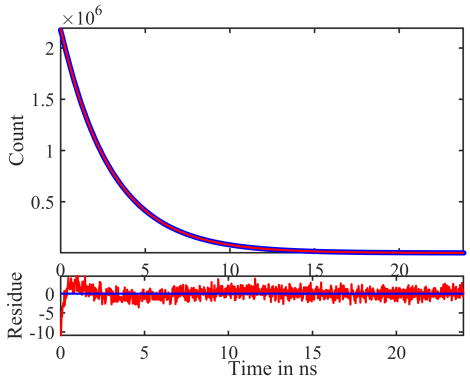

Abb. 3.5: Fluorescent lifetime decay of Atto665-lipid in DOPC bilayer supported on glass. The decay was fitted with a mono-exponential decay function using a maximum likelihood estimator (MLE). Temporal resolution of 16 ps and a cutoff of 0.3 ns were used.

The fluorescence decay was tail-fitted with an mono-exponential decay function using a maximum likelihood estimator (MLE) and a cutoff time of 0.3 ns was. I obtain a lifetime of 3.0±0.1 ns for Atto655-labelled lipid on glass (see figure 3.5). The lifetime of Atto655 in aqueous solution is 1.8 ns, but it shows an increase in lifetime to nearly 3 ns in the SLB due to environmental influence. The long mono-exponential fluorescence decay of Atto655 in SLBs makes this dye a perfect choice for MIET. Moreover, Atto655 is a hydrophilic dye, which reduces the chances that it penetrates the membrane.
One challenge of diffusion measurements with FCS is to obtain absolute diffusion coefficient values, which requires exact knowledge of the size of the scanning Gaussian beam. For determining the beam diameter, we perform a scanning FCS measurement along a 5 μm long line consisting of 100 pixels with a scan speed of 2 kHz. An autocorrelation analysis was then applied to the collected data. The data is spatially and temporally correlated to obtain the 2D spatio-temporal autocorrelation function (ACF) shown in figure 3.6. In a typical FCS experiment, the resulting spatio-temporal ACF yields information about the diffusion of the molecules through the confocal volume as shown along the x-axis of the plot, and the spatial autocorrelation quantifies the confocal volume (along the y-axis of the plot), this eliminates the need for an additional calibration experiment. The correlation plots shown from this

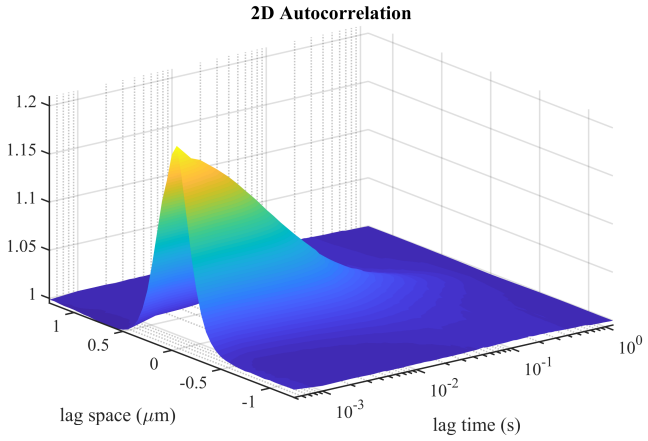

Abb. 3.6: 3D representation of a spatio-temporal autocorrelation function. The x-axis represents the temporal correlation which gives information of the dynamics of a molecule whereas the y-axis represents spatial correlation which is used for quantifying the Gaussian beam profile.

point on will be 2D representations, where the ACF amplitude is represented by color. The resulting ACF is fitted with an appropriate diffusion model to obtain the diffusion coefficient.

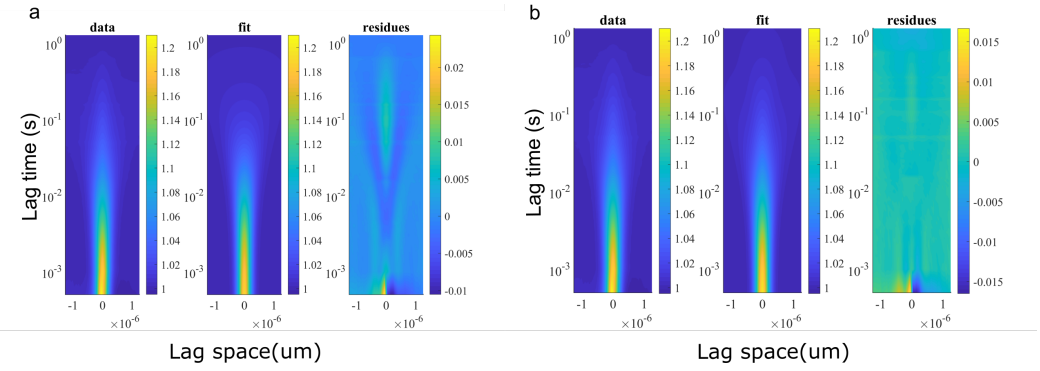

*Abb. 3.7: Comparison of an ACF fit using single-species free diffusion model shown in **a** with two-species free diffusion model in **b**. The ACF for lipid diffusion in DOPC bilayer on glass is best fitted with a two-species free diffusion model.*

I fit the obtained ACF with a two-species free diffusion model. A comparison between the fits using a single-species free diffusion model and two-species free diffusion model is shown in figure 3.7. Using a single-species free diffusion model, the ACF decay at longer lag times cannot be fit properly. Therefore, a two-species free diffusion model was used to fit the data (shown in figure 3.7b).

	sFCS on DOPC bilayer	
D (μm^{2}s^{-1})	2.44 ± 0.34	0.13 ± 0.79
a (%)	87.8	12.2

Table 3.2: Summary of fit results for FCS measurements of lipid diffusion in a DOPC SLB on a glass surface. Shown are the diffusion coefficient D, and amplitude of the corresponding ACF amplitude a.

I find diffusion coefficient values of 2.44 ± 0.34 μm^{2}s^{-1} and 0.13 ± 0.79 μm^{2}s^{-1} for labelled lipid diffusion in a DOPC bilayer on a glass surface (table 3.2). The diffusion coefficient values are in good agreement with the reported value of 2.12 ± 0.89 μm^{2}s^{-1} for a DOPC SLB [7]. However, I also observe slower diffusing component of 0.13 ± 0.79 μm^{2}s^{-1}. The most likely explanations for this slower diffusion value of lipids is that bilayer interaction with the surface slows down the lipid diffusion in the bottom leaflet. Since the measurement times were very long, I was able to see a smaller population corresponding to the slow lipid diffusion associated with the bottom leaflet. Similar studies on supported lipid bilayer have reported a bimodal lipid diffusion that results from lipid interactions with solid support [98, 53, 121]. Another possible explanation is that the slow diffusion could be attributed to trapping by defects or impurities in the bilayer [126]. Thus, quantification of the lipid diffusion in a leaflet-resolving manner will be beneficial to clarify this question.

Another preliminary experiment was done to test the applicability of the technique and its analysis. I took a mixture of two dyes having different lifetimes in glycerol. Glycerol was chosen due to its high viscosity which slows down the diffusion to values similar to those in SLBs. Atto655 ($\tau_{fl} = 1.8$ ns) and Atto647N ($\tau_{fl} = 3.5$ ns) were chosen due to their large difference in fluorescence lifetime. The sample consisted of pure dye dissolved aqueous solution and mixed in a 1:4 concentration ratio with 100 % glycerol. Similar sFCS experiments as described above were performed on this sample. The collected data was analysed in two different ways. In the first analysis, the fluorescence decay was tail-fitted with a bi-exponential decay function using a maximum likelihood estimator. Filter functions over the TCSPC channels were calculated that constitute a dual orthogonal basis to the set of lifetime decay curves. The recorded photons were then weighted with the values of these filter functions. These weighted numbers were then used for calculat-

ing the lifetime-specific fluorescence correlation curves shown in figure 3.8a. In figure 3.8, the ACFs (top) and CCFs (bottom) for Atto655 (dye1) and Atto647N (dye2) are shown. Using the first analysis method, we found a CCF amplitude of ∼6.66 %. As we know, FLCS filtering is based on the difference in TCSPC decay patterns, thus artifacts due to spectral bleed-through as in multi-spectral measurements do not play any role. The second analysis method involves using TCSPC histograms measured on pure dye solutions for computing the FLCS filter functions which were then used to obtain the ACFs/CCFs (3.8b). In this case, as similar CCF amplitude of ∼3.75 % is found.

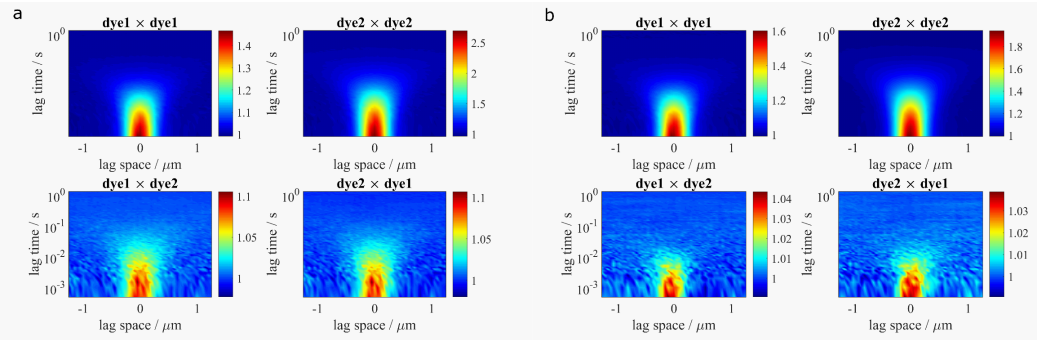

Abb. 3.8: CCFs obtained from a mixture of Atto655 (dye1) and Atto647N (dye2) in glycerol using two different methods of analysis. ***(a)*** *Fluorescence decay was fitted with a bi-exponential decay function, and the resulting two mono-exponential decay were used for calculating the FLCS filter functions. This results in a CCF amplitude of ∼6.66 %.* ***(b)*** *TCSPC histograms measured on pure dye solutions were used for computing FLCS filter functions, resulting in a CCF amplitude of ∼3.75 %.*

A possible explanation for the observed substantial CCF amplitude in both cases could be SPAD afterpulsing, which generates spurious false photon detection event after true photon detection events. The impact of SPAD afterpulsing can be completely avoided by using two SPADs. Therefore, a test measurement of the same dye mixture was recorded using two SPADs. For the analysis, constant background was subtracted from the TCSPC histograms, and additionally a third component that accounts for constant background in a TCSPC histogram was added to the filter functions. Using these three components (dye 1, dye 2 and background) the cross-correlation between the two dye vanishes, see figure 3.9.

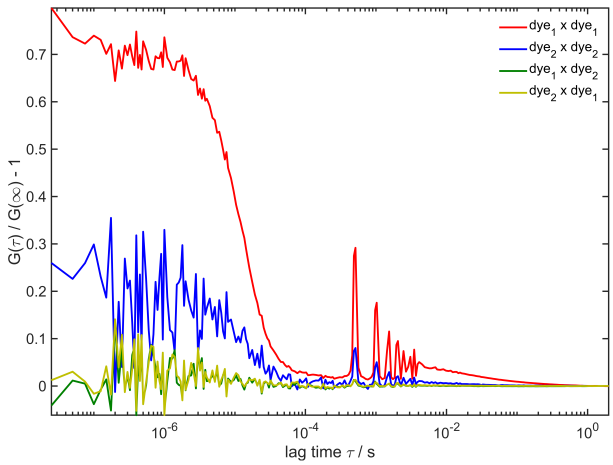

Abb. 3.9: CCF measured on a mixture of Atto655 and Atto647N in glycerol. The CCF amplitude (green and yellow curve) is significantly reduced by removing background from the TCSPC histograms and having a third component for background in the FLCS filter functions. FLCS filtered ACFs of the two dyes are shown in red and blue (analysis by Ingo Gregor).

In summary, FLCS can be efficiently used for separating ACFs of two species having sufficiently different fluorescence decay times. In the next section, I apply MIET that induces a fluorescence lifetime modulation of the dye as function of its distance from the metal surface, and will later use this modulation together with FLCS for obtaining diffusion coefficients in SLBs in a leaflet-resolving manner.

3 Indium Tin Oxide as a MIET substrate

Indium Tin Oxide (ITO) is a perfect example of a transparent but conductive oxide. It has been widely used in nanotechnology owing to its exceptional conductive properties. Robert and co-workers have shown that the near-zero imaginary part of the refractive index of ITO makes it a perfect candidate for applications in microscopy. Due to its ability to quench the fluorescence of an emitter when placed within a distance of ∼20 nm from its surface, ITO can be used for generating an optical ruler [91]. The coupling of an emitter's excited state energy to an absorbing metal layer is modelled in MIET. For a precise conversion of a measured lifetime to a distance, additional knowledge of the free-space lifetime of the fluorescent dye (lifetime in the absence of

metal), its quantum yield, as well as its dipole orientation are required. The calculated MIET curve (see figure 3.10) shows the lifetime and brightness dependence as a function of distance from the ITO surface. To prevent complete fluorescence lifetime quenching for dyes directly on the surface, a silicon dioxide layer with a thickness of 4 nm and a refractive index of 1.46 was deposited on the ITO surface. This has been taken into account in the calculations of the MIET curve. The SiO_2 layer does also provide a hydrophilic support, in contrast to the hydrophobic ITO surface. MIET calibration curves for different SiO_2 spacer thickness values are shown in figure 3.11b. When increasing the spacer thickness, the lifetime-to-distance dependence becomes less steep. Therefore, 4 nm SiO_2 deposition is adequate to prevent fluorescence quenching but ensures a steep lifetime-to-distance dependence.

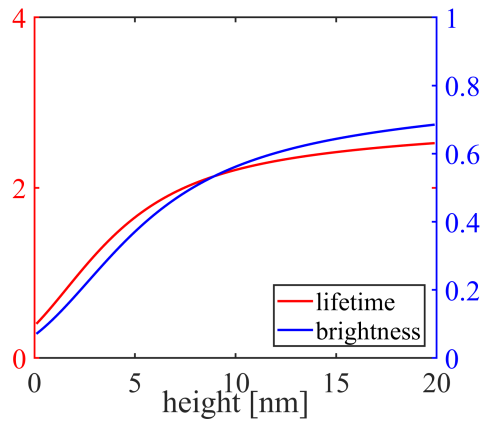

Abb. 3.10: MIET calculation of an emitting dipole's distance from the ITO surface, showing lifetime and brightness as a function of distance. Note that the substrate includes a 4 nm thick SiO_2 layer deposited on the ITO surface.

For performing MIET experiments, prior knowledge of the fluorescent dye's properties is mandatory. Atto66-DPPE was used for most of the SLB measurements in this thesis. The lifetime of the dye was determined in the bilayer environment and used as the free-space lifetime (τ_0). We found an Atto655 free-space lifetime in the bilayer to be 3 ns (see figure 3.5). Thus, lipid analogues labelled with Atto655 show a huge deviation from the dye's lifetime of 1.8 ns in aqueous solution. The anchoring of the lipid to the dye results in a huge environmental change that leads to this increase in lifetime to 3 ns. The dye's quantum yield value was calculated by comparing the known quantum

yield of the free dye (QY_0 and τ_{fl}) to the determined free-space lifetime (τ_0) in the SLB, and it was found to be 0.5. This calculation assumes that only the non-radiative rate k_{nr} is changed. The expression for the calculation of the quantum yield is

$$QY = \frac{n}{n_0}\frac{\tau_{fl}}{\tau_0}QY_0 \tag{3.1}$$

Additionally, I take into account the presence of the bilayer of thickness 5 nm, having a refractive index of 1.46, and I assume a random dye orientation. Unfortunately, the refractive index of ITO does strongly depend on the manufacturing process used by the supplier, and it is also sensitive to diffusion of oxygen from the atmosphere into the ITO material, which can result in further changes. The refractive index values for ITO were taken from Falk Schneider's master thesis where he measured the refractive index using ellipsometry.

The MIET model calculation takes into account the ITO layer thickness of 281 ± 8 nm and assumes a refractive index of $1.85 + 0.012i$ at an emission wavelength of 690 nm. The small complex value of 0.012 of this index, which is much smaller than for metals, results in the steep lifetime-to-axial-distance dependency of the MIET curve.

Figure 3.10 emphasises that the ITO-induced fluorescence modulation takes place over a distance range up to ∼20 nm. Thus, ITO-based MIET is much suitable for short distances, such as found in a DOPC-SLB with bilayer thickness of about ∼5 nm. For example, for the axial distance of 5 nm between the two leaflets, a lifetime change of nearly 1 ns is expected. This strong distance dependence of the lifetime is exploited to extract distance values from the measured lifetime. However, the dye dipole orientation in the given system affects its fluorescence lifetime, see to figure 3.11.

The calculation considers parallel, vertical, and random dipole orientations with respect to the bilayer interface. Figure 3.12 displays a 50 μm×50 μm atomic force microscopic image of an ITO substrate. It shows an inhomogeneous surface that is most likely due to the sputtering deposition process. These inhomogeneities could not be eliminated by washing with isopropanol. The root-mean-square roughness was found to be nearly 2.33 nm, and peak heights of nearly 6 nm were found throughout the surface.

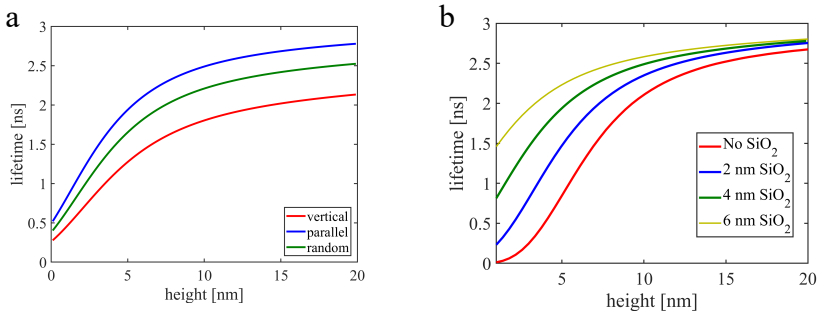

Abb. 3.11: **a**: *MIET calibration curve for Atto655-labelled SLB on an ITO substrate covered with a 4 nm SiO_2 spacer as a function of dipole orientation with respect to the membrane surface at an emission wavelength of 690 nm.* **b**: *MIET calibration curve for different SiO_2 spacer thickness values. In the absence of a spacer, the fluorescence lifetime a dye molecule on the surface is zero.*

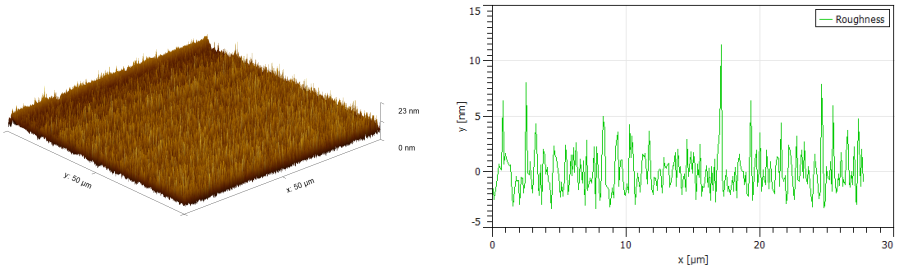

Abb. 3.12: AFM image of 50 µm×50 µm surface of ITO coated with a SiO_2 spacer (left). The right plot shows the surface roughness having a RMS value of 2.33 nm. The AFM image was measured by Bastian Brueckner from the group of Andreas Janshoff.

3.1 Leaflet-dependent lipid diffusion using sFLCS on SLB

A DOPC bilayer with a very low percentage of headgroup-labelled DPPE-Atto655 was prepared on the ITO substrate. Fluorescence decay curves were recorded with a standard confocal microscope equipped with a TCSPC electronics (see chapter 3, section 1, for details). These fluorescence decay curves were fitted with a bi-exponential decay function using a MLE. The fitted decay times of the dye on the DOPC bilayer were $\tau_1 = 1.7 \pm 0.06$ ns and $\tau_2 = 2.5 \pm 0.01$ ns, respectively. Longer measurement times were employed to ensure the collection of at least one million photons.

The amplitudes of the lifetime components were about 20 % and 80 %, while

the shorter lifetime component contributed lesser to the fit than the longer lifetime component. I associate the shorter lifetime to labelled lipids in the bottom leaflet, and the longer lifetime to labelled lipids in the top leaflet of the SLB. The lower amplitude of the shorter lifetime component suggest larger fluorescence quenching due to the larger proximity of the dyes in the bottom leaflet to ITO. After converting the lifetime values to height values using the MIET calibration curve (Figure 3.11a), I found the end-to-end distance between Atto655-labelled lipids in the bottom and top leaflets to be 7.05 ± 0.14 nm.

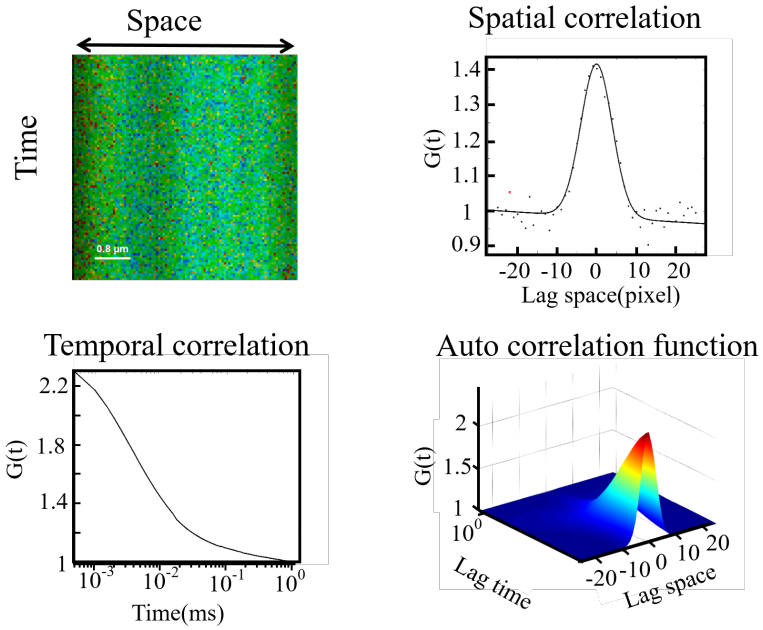

Abb. 3.13: Schematic of line scan-FCS: Top-left figure shows a stack of i lines stacked vertically to obtain an image where the y-axis represents the line number corresponding to time iT, and the x-axis gives the scan position in pixels. I applied an ACF analysis to obtain the spatio-temporal correlation depicted at top-right and bottom-left. Shown at bottom-right is the combined three-dimensional ACF, where the spatial correlation is along the x-axis, and the temporal correlation is along the y-axis of the plot.

Using the fluorescence decay fits, FLCS filter functions over the TCSPC channels were calculated which constitute a dual orthogonal basis to the set of lifetime decay curves. Three components were used for computing the filter functions, where the third component accounts for constant background.

Recorded photons were then weighted with the values of these filter functions according to their TCSPC channel number. These weighted values were then used for calculating lifetime-specific fluorescence correlation curves.

An additional challenge in these measurements is to obtain a precise quantitative diffusion coefficient, which depends on the exact knowledge of the Gaussian intensity profile of the laser focus on the bilayer plane. The absolute diffusion coefficients are obtained by employing a scanning confocal microscope where we are sequentially scanning along parallel lines. A schematic of the experiment is shown in figure 3.13, where a line of 5 μm length containing 100 pixels was scanned with a scan speed of 2 kHz. We apply a correlation analysis to the recorded data that results in a so-called ACF. We do not only obtain a characteristic temporal decay (bottom-left) due to diffusion, but also a spatial correlation (top-right) which gives us the size of the Gaussian beam profile of the excitation spot. This intrinsic knowledge of the beam profile makes this technique calibration-free, thus eliminating the requirement for an additional calibration experiment. Additionally, we avoid artifacts due to photobleaching, vertical focus misalignment on the bilayer, and long measurement times that may be problematic due to the opto-mechanical (in)stability of the setup.

In figure 3.14, I show the ACF and CCF for the diffusion of labelled lipids in the bottom and top leaflet of a DOPC-SLB. The ACF of the top leaflet is fitted using a two-species free diffusion model from which the beam waist size (ω_0) is extracted. This ω_0-value was then used to fit the ACF of the bottom leaflet. The observed correlation for the bottom leaflet (top-left) at longer lag times suggests a diffusion of the lipids that is slower than that in the bottom leaflet (compare with top-leaflet ACF at top-right). This could also explain the observed smaller amplitude of the lifetime component corresponding to the bottom leaflet. The slower lipid diffusion in the bottom leaflet could be attributed to interactions of the labelled lipids with the solid substrate, or it could be due to bilayer nano-defects that were generated during the SLB preparation. The surface roughness as observed with AFM (figure 3.12) could also be accounted by the presence of these defects in a SLB [11]. Several studies have also shown that hindered diffusion in SLBs may explain the slower diffusion observed in our measurements [34, 125, 107]. Erdinc and coworkers have shown the presence of brief interactions

between the support and the SLB-constituting lipids, and suggested that they originate from nanoscale surface perturbations due to the surface roughness [8]. Please note that the negligible cross-correlation (bottom) is matching our expectation. Since the labelling concentrations were kept low, direct interactions (and thus correlations) between labelled lipids in both leaflets should be negligible.

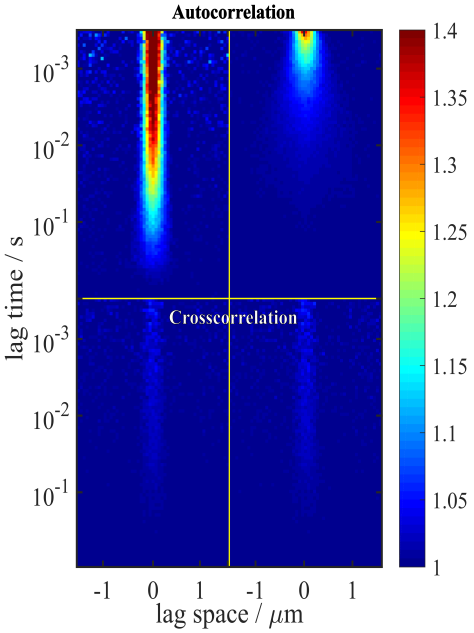

Abb. 3.14: ACF corresponding to lipid diffusion in the bottom leaflet (top-left) indicates a slower diffusion as that of lipids in the top leaflet (top-right) of a SLB. We see negligible cross-correlation between the two leaflets.

A kinetic adsorption/desorption diffusion model is used to fit the diffusion in the bottom leaflet. This model considers reversible adsorption and desorption (so-called sticking and unsticking) of labelled lipid to the substrate. It is found that the data can be best fitted when taking into account a partial sticking of the labelled lipids to the bilayer support as shown in figure 3.15. The bottom leaflet is fit with a adsorption/desorption model as described in the theory section 5.3 where we consider reversible transitions from freely diffusing to an immobile state (sticking) and back (unsticking). We determine the sticking k_+ and unsticking k_- rates constants of the lipids in the bottom leaflet. The ACF corresponding to the top leaflet was fitted using a two-species free diffusion model, the fits are shown in figure 3.16. Table 3.3

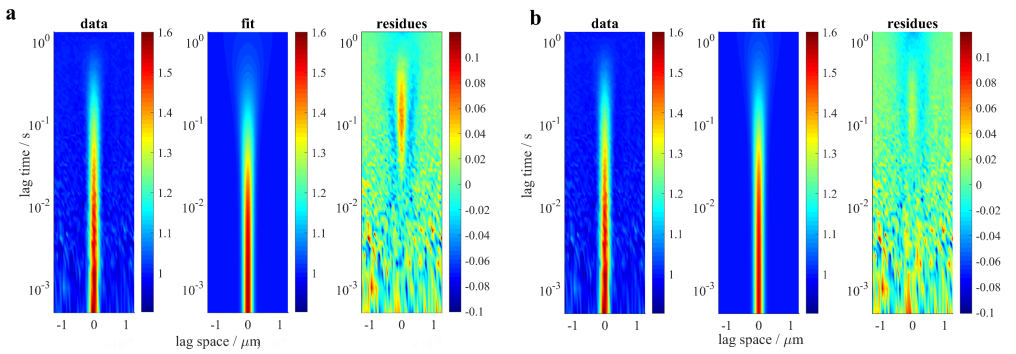

Abb. 3.15: ACF corresponding to lipid diffusion in the bottom leaflet of a SLB was fitted with two different models. ***(a)*** *Data fitting without the adsorption/desorption model. The data was fitted with a single-component diffusion model. The high residues observed at longer lag times show that the model is unsuitable for this case.* ***(b)*** *Data fitted with an adsorption/desorption model 5.3 shows comparatively better fit residues.*

summarises the fit results of the FCS experiment on DOPC-SLBs on ITO.

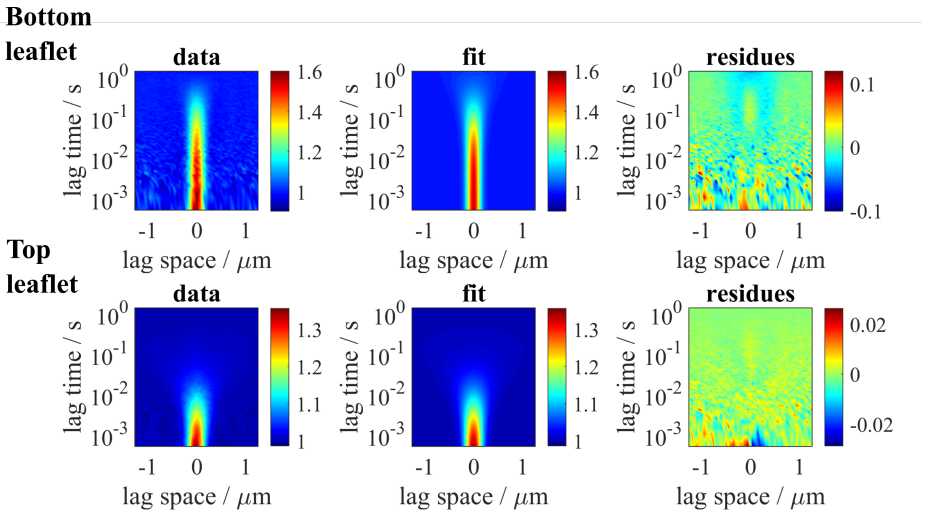

Abb. 3.16: The ACF of the lipid diffusion in the bottom leaflet (above) is fitted using an adsorption/desorption model as discussed in detail in section 5.3. Shown in the middle are the fit and its residues (right). The lipid diffusion in the top leaflet, see ACF below, was fitted with a two-species free diffusion model. The fit result and the residues are shown in the middle and far-right, respectively.

It should be emphasised that our results are in excellent agreement with reported diffusion coefficients of 0.091 ± 0.002 $\mu m^2 s^{-1}$ and 4.82 ± 0.02 $\mu m^2 s^{-1}$ associated with lipid diffusion in the bottom and top leaflets of a DOPC-

	bottom leaflet	**top leaflet**	
D (μm^{2}s$^-$1)	0.79 ± 0.40	2.50 ± 0.03	0.60 ± 0.10
a (%)	100	92.4	7.6
k_+ (s^{-1})	15.72		
k_- (s^{-1})	53.15		

Table 3.3: Fit results for FCS measurements of lipid diffusion in the bottom and top leaflets of a DOPC-SLB on an ITO substrate. Displayed are the diffusion coefficient D, corresponding FCS amplitude a, rate constant k_+ for transitions from freely diffusing to immobile state (sticking), and reverse rate constant k_- for transitions from immobile to freely diffusing state (unsticking).

SLB, and with similar studies on these bilayers using single-particle tracking [121, 89, 122] or fluorescence correlation spectroscopy [9]. However, to date no slow population has been identified using FCS, and I present the first such experiments where I have successfully been able to observe the slow-diffusing population. I found that the lateral lipid diffusion in the bottom leaflet is nearly two times slower than the faster diffusing component in the top leaflet, having a diffusion coefficient of 0.79 ± 0.40 μm^{2}s^{-1}. The sticking and unsticking rate constants for the labelled lipids in the bottom leaflet to the substrate are found to be 15.72 s^{-1} and 53.15 s^{-1}, respectively. The ACF associated with lipid diffusion in the top leaflet was best fitted using a two-species free diffusion model. I found faster lipid diffusion in the top leaflet as compared to the lipid diffusion in the bottom leaflet with a 2.50 ± 0.03 μm^{2}s^{-1} diffusion coefficient. I find slow lipid diffusion in the top leaflet with a diffusion coefficient of 0.60 ± 0.10 μm^{2}s^{-1}. The amplitude a of the slow diffusing population in the top leaflet is 7.6 %. Interestingly, the slower lipid diffusion in the top leaflet is comparable with the bottom leaflet lipid diffusion, indicating that there could be a possible interaction of the top leaflet with the bottom leaflet. However, there is a possibility that the slow diffusion in the top leaflet originates from defects in the top leaflet. Some reports suggest that the slow lipid diffusion in top leaflet could be due to inter-leaflet drag (influence of bottom leaflet) [58, 138] or due to bilayer defects [147]. Many studies have supported the concept of inter-leaflet coupling, along with others that speak against this hypothesis.

Some recent studies have also provided insight into lipid dynamics, where

authors have used fluorescence quenching to differentiate between the two leaflets [150, 121]. However, they have assigned the two diffusing populations to the respective leaflets, but the question of the exact cause of these two populations or their effect on each other remains elusive. In my study, I have presented a more precise distinction between lipid diffusion in each leaflets of a SLB and I did observe both slow and fast diffusing components in the top leaflet.

3.2 Top leaflet labelling of DOPC SLB

To support the FCS results described above, I performed a simple control experiment where I labelled only the top leaflet by adding dye to the solution above an unlabelled SLB. I added bulky dye-labeled lipids to avoid their penetration to the bottom leaflet. The measurements were started instantly after dye addition to avoid further penetration of dye to the bottom leaflet through defects.

A DOPC-SLB was prepared by fusing unlabelled vesicles of 50 nm size on an ITO substrate. 20 μl of 50 nM headgroup-labelled Atto655-DPPE was added to the SLB sample. The sample was let to settle for few minutes and line-scan FCS data was acquired immediately afterwards. The fluorescence decay was tail fitted with a mono-exponential decay function using a maximum likelihood estimator and a cutoff time of 0.3 ns. Figure 3.17 shows the decay fit yielding a fluorescence lifetime of 2.49 ± 0.05 ns. This fluorescence lifetime value is similar to the lifetime seen for the top leaflet of a DOPC-SLB in my previous experiments.

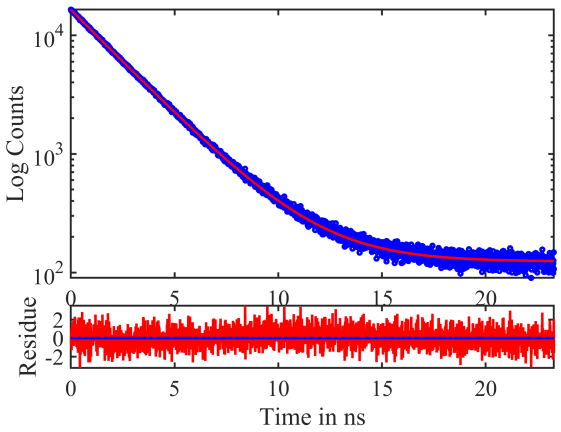

Abb. 3.17: Fluorescence decay (blue) was fitted using a mono-exponential decay function (red). Maximum likelihood estimator was used and a cutoff of 0.3 ns was employed.

An ACF analysis was applied to the recorded data and the obtained ACF associated with the lipid diffusion in the top leaflet was fitted with the two-species free diffusion model, similar to the previous experiments. Figure 3.18 shows the ACF along with the fit. The fit shows residues of $\sim$1 %. We found diffusion coefficients of 2.37 ± 0.13 $\mu m^2 s^{-1}$ and 0.38 ± 0.40 $\mu m^2 s^{-1}$ with

amplitudes of nearly 88 % and 12 %, respectively (see table 3.4). It must be emphasized that the diffusion coefficients are comparable with previously reported values of 2.50 ± 0.03 $\mu m^2 s^{-1}$ and 0.60 ± 0.10 $\mu m^2 s^{-1}$ of lipid diffusion in the top leaflet of a DOPC-SLB.

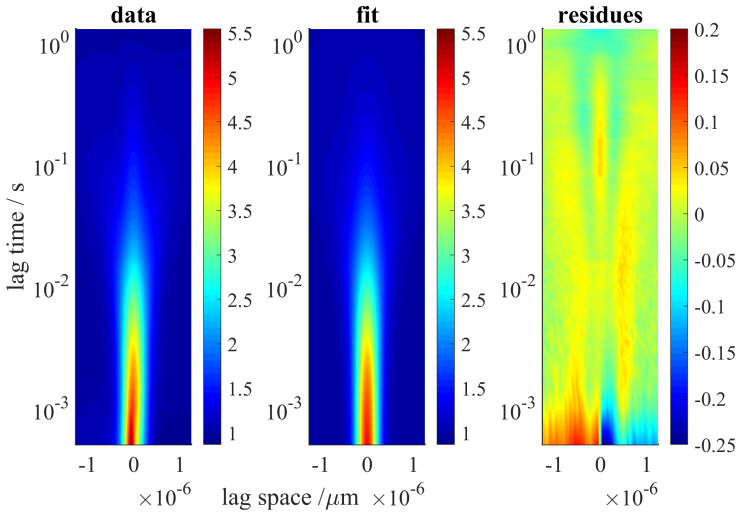

Abb. 3.18: ACF of lipid diffusion in the top leaflet of a DOPC-SLB. The ACF is fitted with a two-species free diffusion model. Fit residues of ∼1 % are negligible.

	top leaflet	
D ($\mu m^2 s^{-1}$)	2.37 ± 0.13	0.38 ± 0.40
a (%)	88.32	11.68

Table 3.4: Summary of fit results of sFCS experiments on top-leaflet labelled DOPC bilayer. Reported here are diffusion coefficient D of lipid diffusion associated with the top leaflet, and the corresponding ACF amplitudes a.

3.3 Lateral lipid diffusion in POPC supported lipid bilayer

The method was further applied to SLBs of different lipid bilayer composition. SLBs composed of POPC and a low concentration of Atto655-DMPE were prepared on ITO substrates. SLB quality was checked with FLIM as well as with point FCS measurements. Similar line-scan FCS measurements as before were performed on a homogeneous region of the bilayer sample.

Data analysis was done in a similar way. The obtained fluorescence decay was fitted with a bi-exponential decay function. I obtain lifetime values of 2.10 ± 0.01 ns and 2.59 ± 0.02 ns with amplitudes of 21 % and 79 %, respectively. These lifetimes were converted into distance values using the MIET calibration curve shown in figure 3.11. This gives us an end-to-end axial distance of 6.36 ± 0.38 nm for the labelled lipids in the bottom and top leaflet of the DOPC-SLB. This value is smaller than that for the end-to-end axial distance of labelled lipids in a DOPC-SLB which is 7.05 ± 0.14 nm. A significant difference of $\sim$0.7 nm is observed. Longer axial distance between labelled lipids in DOPC-SLB as compared to that in POPC-SLB is due to the different chain lengths of the fatty acids of DOPC and POPC, which differs by 2 carbon atoms. The DOPC lipid has 18 carbon atom chains with 2 unsaturated bonds, whereas POPC consists of 16 carbon atom chains with one unsaturated bond [70].

However, it is unlikely that the observed distance difference of $\sim$0.7 nm between DOPC and POPC is due to this difference in fatty acid chain length. Despite the two extra carbon atoms in the DOPC lipid, the observations of John and coworkers have shown that the double bond in DOPC induces sufficient disorder in an SLB that reduces its thickness to that of a DMPC-SLB, even though the latter has 4 fewer carbon atoms [94].

Moreover, there could be additional errors in the calculation due to inaccurate knowledge of the ITO refractive index, or uncertainties in dye dipole orientation which was assumed to be totally random in the MIET calculations.

Data analysis was performed in a similar way as in the previous section 3.1. The ACF associated with labelled lipid diffusion in the bottom leaflet of a POPC-SLB was fitted using the adsorption/desorption model, and the ACF of lipid diffusion in the top leaflet was fitted using a two-species free diffusion model. Shown in table 3.5 are the sFCS fit results.

I observe faster lipid diffusion in the bottom leaflet of POPC-SLB with a diffusion coefficient of 2.03 ± 0.58 $\mu m^2 s^{-1}$ as compared to that of a DOPC SLB with a diffusion coefficient of 0.79 ± 0.40 $\mu m^2 s^{-1}$. The large difference in lipid diffusion in the bottom leaflets of the two bilayer systems can possibly be explained by assuming that bilayer formation on the rough surface could lead to regions where a bilayer is in close contact with the surface than in

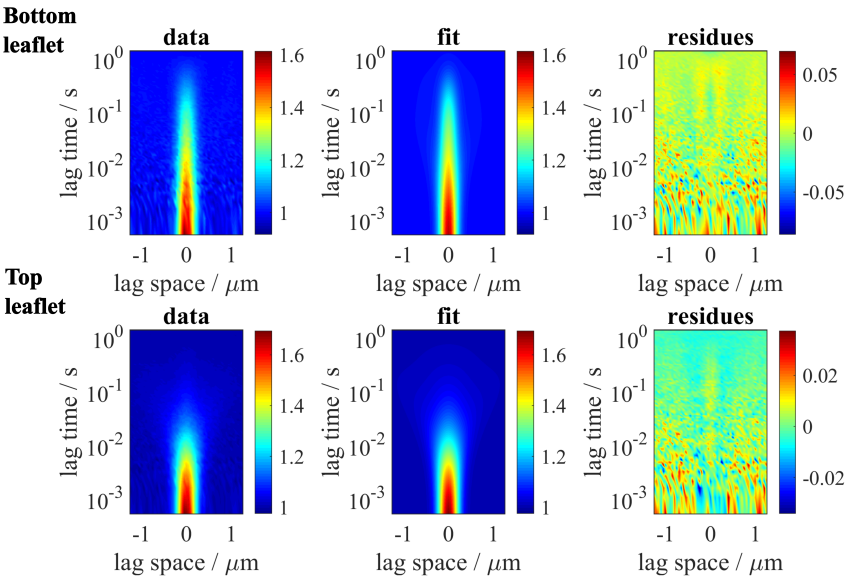

Abb. 3.19: ACF of lipid diffusion in the bottom leaflet (above) is fitted with an adsorption/desorption model as discussed in detail in section 5.3. Shown in the middle are the fit, and on the far-right the fit residues. For lipid diffusion in the top leaflet of a POPC-SLB, the ACF (below) was fitted with a two-species free diffusion model.

	bottom leaflet	**top leaflet**	
D (μm^{2}s^{-1})	2.03 ± 0.58	2.67 ± 0.16	0.27 ± 0.13
a (%)	100	92.0	8.0
k_+ (s^{-1})	2.93		
k_- (s^{-1})	3.68		

Table 3.5: Summary of fit results of sFCS experiments on POPC-SLB. Reported are the diffusion coefficients D for labelled lipids in the bottom and top leaflets of the SLB, with their corresponding FCS amplitudes a, and the rate constants of adsorption (sticking) k_+ and desorption (unsticking) k_- of lipids to/from the ITO substrate.

other regions. Peak heights of nearly 6 nm were observed in AFM images of ITO (see figure 3.12). I find reduced sticking/unsticking rates of labelled lipid to the substrate, from 15.72/53.15 s^{-1} in DOPC-SLBs to 2.93/3.68 s^{-1} in POPC-SLBs, which supports my above assumption. Lipid diffusion in the top leaflet shows diffusion coefficients of 2.67$\pm$0.16 μm^{2}s^{-1} and 0.27$\pm$0.13 μm^{2}s^{-1} having amplitudes of 92 % and 8 %, similar to the diffusion coefficient of

lipid diffusion in a DOPC-SLB. The slow-diffusing population found in the top leaflet indicates that defects in the top leaflet are the possible cause of this observation.

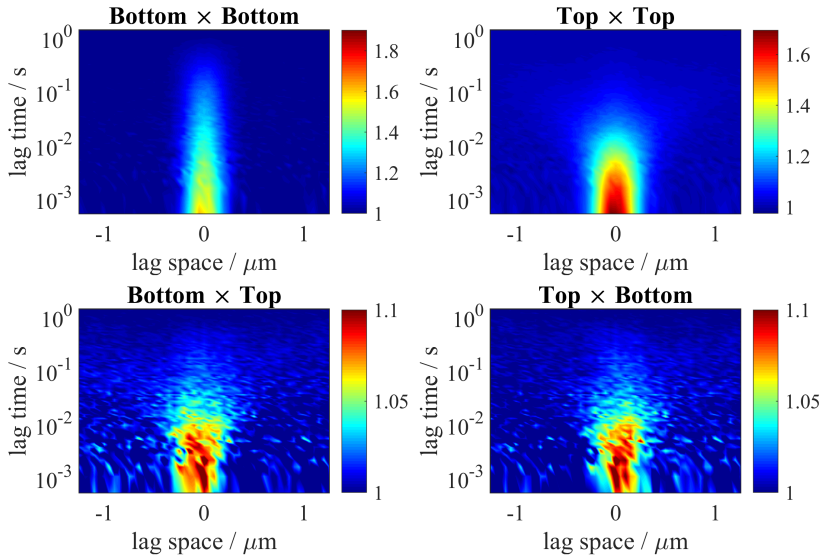

Abb. 3.20: Auto-correlation function of lipid diffusion in the bottom leaflet of a POPC-SLB shows slow lipid diffusion as compared to that of the top leaflet. The CCF between the two leaflets (bottom leaflet versus top leaflet and top leaflet versus bottom leaflet) shows a ∼ 12 % CCF amplitude.

Moreover, a cross-correlation amplitude of ∼ 12 % was found (figure 3.20). All results were reproducible after multiple POPC bilayer preparations. The ∼ 12 % CCF amplitude suggests possible interactions (co-diffusion) between labelled lipids in the bottom and top leaflets, which is highly unlikely since the labelling concentrations were low. However, hindered diffusion due to defects or surface heterogeneity could explain the results, but no clear quantitative estimate can be given for the cross-correlation amplitude.

3.4 Rapid Imaging of labelled lipids in SLB

The core idea behind rapid imaging experiments on SLBs is to distinguish the leaflets based on the brightness of dye molecules at different distances from the ITO surface. When labelled lipids are located at different distances from the surface, they experience different fluorescence quenching and hence exhibit different brightness, see also figure 3.22c. With the help of advanced

cameras such as EMCCDs, it is possible to directly image fast diffusing single molecules. Each detected molecule is seen on the camera a wide spot corresponding to the point spread function (PSF) of the microscope. A molecule's positions can then be obtained by fitting the center position of this PSF, and the accuracy of this fit does largely depend on the collected number of photons from a molecule, but also on background level and how fast a molecule diffuses. For example, to properly locate a single molecule in a an image with 1 ms exposure time, a minimum of 100 photons are required. Hence, the count rate should be larger than 10^5 counts/s. To meet this photon requirement, a high excitation power is needed. When performing quantitative studies (molecular brightness in our case), a homogeneous excitation is ensured by pre-processing recorded videos.

3.4.1 Experimental Method

Movies were recorded on a wide-field microscope (Olympus IX71), aligned with a $\lambda = 638$ nm laser (638L-11A Matchbox 2). The laser was guided through an AOTF (AOTFnC-400.650-TN with driver AA.MDS4C-B65-22-74.158, AA Optoelectronic) and was coupled into a single-mode fiber (SMC-E-400Si-2.6-NA012-3-APC.EC, Schäfter and Kirchhoff) which guided the light into the microscope. A 100X UApoN TIRF-objective (NA = 1.49) and an EMCCD (ANDOR iXon 897D) with an effective pixel size of 160 nm were used.

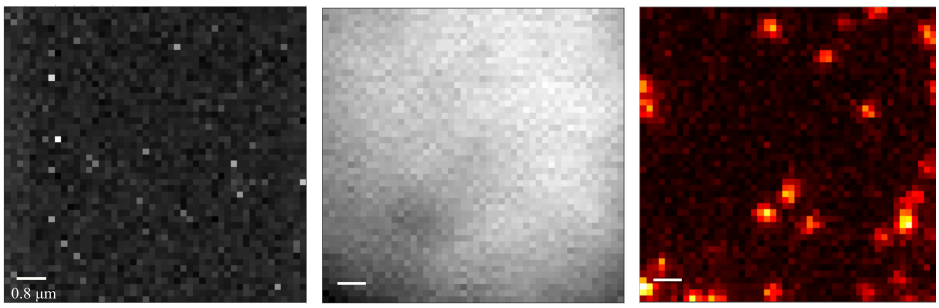

Abb. 3.21: Examples of a dark image, flat field image and recorded raw image (left to right).

A sparsely labelled DOPC bilayer was prepared on an ITO substrate (see section 1 of this chapter) and 100k frames were recorded. The signal-to-noise ratio was improved by using a high-power laser of 140 mW in full field

of view. Uniform excitation intensity was ensured in the region of detection, and a small aperture was used to avoid fluorescence bleaching of the whole sample region. The exposure times were reduced to 3.26 ms, and the camera's EM gain was set to 300.
A dark video was recorded without laser excitation by keeping the shutter closed, and the excitation intensity profile was determined by recording a flat field video in the same region using a droplet of 1 μM Atto655 dye. Averaged intensity images were obtained from the recorded dark video and flat field video (see figure 3.21).

3.4.2 Data analysis

Recorded videos were first flat-field corrected [39] using the equation

$$C = \frac{R - D}{F - D} \times m \tag{3.2}$$

where R is a raw image (see far-right in figure 3.21), F is the flat-field image, and D is the dark-field image, and m is the image-averaged value of $(F - D)$. The output C gives us the corrected image.
The flat-field corrected movies were then analysed with the 'TrackNTrace' Matlab GUI developed by Simon Stein and Jan Thiart [137]. Wavelet filter and TNT fit plugins were used for candidate detection, see Jan Thiart's PhD thesis. Obtained positions were then used in the nearest-neighbour tracker, and parameters such as particle size, maximum allowed frame gap and minimum trajectory length were optimised until a satisfactory result was obtained. These settings were then used in u-Track where these parameters are optimised and visualised as shown in figure 3.22a. I observe hindered diffusion for some molecules, one such example is shown by the circle marking. The molecule was seen in 105 frames (3.26 ms frame exposure time) before it photobleached. The mean brightness values of tracks longer than 20 frames were plotted in a histogram. The obtained histogram was fitted with two Gaussian functions (see in figure 3.22b). I associate the two populations to labelled lipid in the bottom and top leaflets of the DOPC bilayer. The intensity ratio of the populations is found to be 0.42. Figure 3.22c shows the MIET calculations for the molecular brightness as a function of distance from the ITO surface. The calculations take into account a SiO_2 spacer

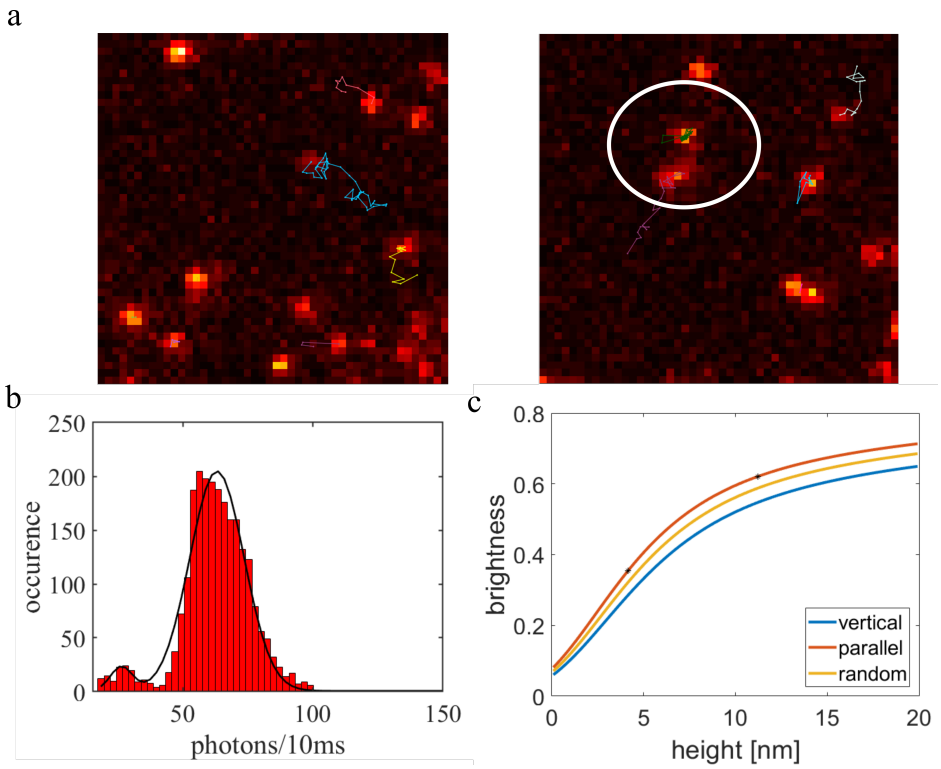

Abb. 3.22: Single particle tracking of labelled lipids in DOPC-SLB. ***(a)*** *Example of Atto655-DPPE diffusing in SLB with tracked positions. Encircled is an example of hindered diffusion, the molecule was observed in 105 frames before photobleaching.* ***(b)*** *The histogram of the mean photon number per 10 ms obtained from each track shows two populations associated with each leaflet.* ***(c)*** *MIET calibration curve for brightness. The corresponding height value obtained from the lifetime measurement on DOPC-SLB is marked. This value is taken as theoretical value.*

thickness of 4 nm. The heights of the DOPC bilayer found from the lifetime experiments are marked in the calibration curve, and the theoretical relative brightness values were extracted. The brightness ratio of an emitter in the bottom to the top leaflet is found to be 0.56.

Tracks corresponding to the two populations in the histogram 3.22b were separated by a threshold value of 42 and were then analyzed with a mean-square-displacement (MSD) routine. For each trajectory's N position vectors $\mathbf{r}_i = (x_i, y_i)$, $i = 1, 2.., N$, all possible frame increments $\mathbf{r}_{ij} = \mathbf{r}_j - \mathbf{r}_i$, $1 \leq i < j \leq N$, were calculated, where the frame increment time is $\Delta t_{ij} = (j - i)t_{ex}$. Here, t_{ex} is the exposure time of the camera. The displacements $|\mathbf{r}_{ij}|$ for each frame interval Δt_{ij} were histogrammed and then fitted (figure 3.23a and c). In figure 3.23, the plots at top correspond to the dimmer population,

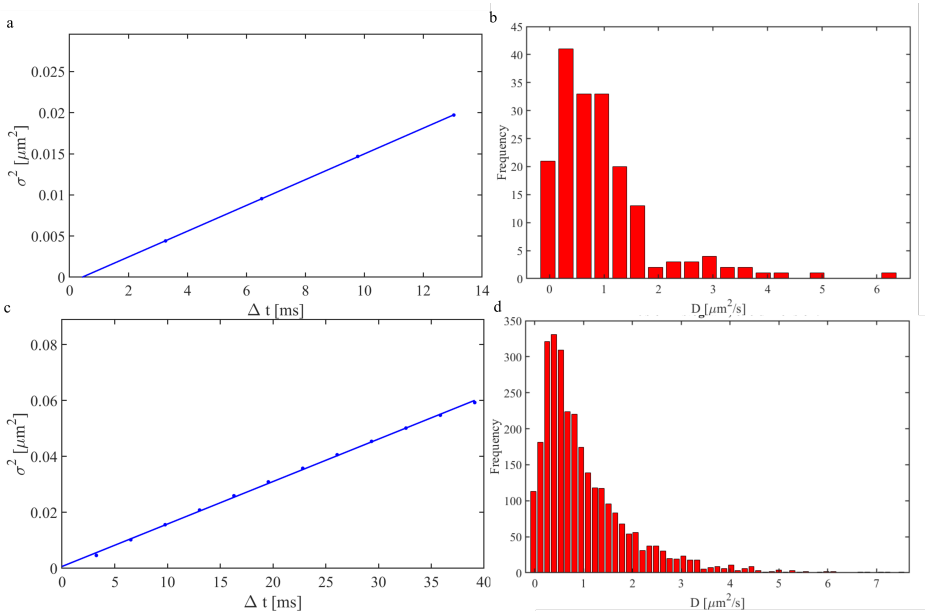

Abb. 3.23: Mean-square-displacement (MSD) fit for the dimmer (top-row) and brighter (bottom-row) populations. I associate the dimmer population to dye molecules in the bottom leaflet, and the brighter population to the dye molecules in the top leaflet of the SLB. ***(a)*** *and* ***(c)****: Average MSD of molecules for the two populations corresponding to bottom and top leaflet, respectively.* ***(b)*** *and* ***(d)****: Histogram of diffusion coefficient values obtained from each trajectory of the two populations.*

whereas the bottom plots are for the brighter population. We associate the less bright population to labelled lipids in the bottom leaflet, and the brighter population to labelled lipids in the top leaflet of a SLB. The MSD-derived diffusion coefficient for the dimmer population is 0.783 ± 0.004 μm^{2}s^{-1} which is in excellent agreement with earlier FCS results for the bottom leaflet of a DOPC-SLB (see table 3.3). The brighter population has a diffusion coefficient value of 0.759 ± 0.007 μm^{2}s^{-1}. It shows a slower lipid diffusion for the brighter population as compared to the FCS result for the top leaflet. Additionally, I calculated and fitted the MSD curve for each trajectory and created a diffusion histogram shown in figure 3.23b and d. The obtained diffusion coefficients show a broad range of values. The diffusion histogram shows an almost similar trend for both populations of the bottom and top leaflet of the SLB. Based on these results, I surmise that both leaflets do possibly have slowly and rapidly diffusing lipid populations.

3.5 Quenching of top leaflet labelled lipids in SLB

Additional control experiments were performed to support the FCS diffusion results. The idea is to quench dye in the top leaflet of an SLB to reduce their contributions to the fluorescence signal and to observe the resulting changes in diffusion. It is one of the commonly used method for leaflet-dependent studies in membranes [121]. Different volumes (1 μl and 2 μl) of a saturated solution of potassium iodide (KI) were added to Atto655-labelled DOPC-SLBs. The measured fluorescence decay was globally fitted with four lifetime components while keeping the lifetime values fixed (see figure 3.24). I find a low amplitude for the lifetime component of 1.72 ns that is associated with the bottom leaflet in absence of KI 3.6. Fit results are summarized in table 3.6, and they show a mono-exponential fluorescence lifetime decay in the absence of KI. However, I do see a reduced lifetime of 2.5 ns as compared to the free-space lifetime of 3 ns. Multiple experiments performed on different ITO substrate resulted in a mono-exponential fluorescence decay of Atto655 dye in SLBs. The deviation from previous bilayer experiments on ITO was found to be due to faulty ITO coverslips.

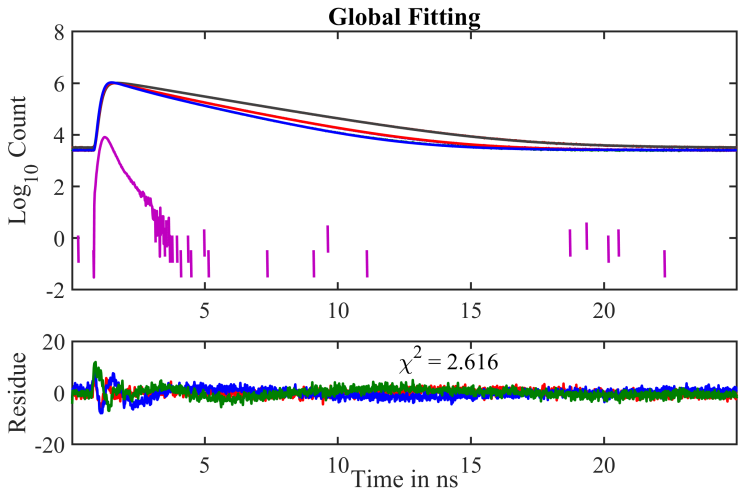

Abb. 3.24: Fluorescence decay of Atto655 labelled DOPC bilayer in three different conditions : Absence of quencher (green), 1 μl of KI quencher (red) and 2 μl of KI quencher (blue). The data was globally fitted using four lifetime components (analysis by Narain Karedla).

	Amplitudes		
lifetimes (ns)	**without KI**	**1 μl**	**2 μl**
0,09	0,01	0,02	0,04
0,55	0,01	0,06	0,12
1,72	**0,02**	0,54	0,69
2,50	**0,96**	0,36	0,13

Table 3.6: In the absence of quencher, the fluorescence decay of Atto655 in DOPC-SLB is mono-exponential. The mono-exponentiality of the fluorescence decay of labelled lipids in SLBs on ITO was due to faulty ITO coverslips.

3.6 Conclusion

In summary, for DOPC-SLBs I found relatively slow lipid diffusion in the bottom leaflet that I attribute to lipid-surface interactions. Additionally, my results show a slow lipid diffusion in the top leaflet as well, which could be due to bilayer defects or inter-leaflet coupling. However, in the case of POPC-SLBs, I find less interaction of lipids in the bottom leaflet with the ITO substrate. Additionally, the slow lipid diffusion of lipids in the top leaflet indicate that the possible cause of the slow lipid diffusion in the top leaflet is due to bilayer defects. Moreover, similar results were produced in single-particle tracking experiments, where I find a slow lipid diffusion associated with the top leaflet of a SLB. By calculating MSD-curves for each trajectory, I find a broad range of diffusion coefficients for both leaflets of a SLB. Unfortunately, due to product faults of the purchased ITO coverslips, I had to switch to a better alternative. In the next section, I replace ITO with single-sheet graphene for performing similar experiments.

4 Graphene as a MIET substrate

Similar to ITO, the metal layer in MIET can be substituted with a single sheet of graphene, which induces a similar near-field electromagnetic coupling with a fluorescent emitter as seen for metals or ITO. Graphene is a two-dimensional (2D) sheet of covalently bonded carbon atoms having π-conjugation. The intriguing properties of graphene have been thoroughly researched [96, 148]. The zero-band gap electronic energy spectrum makes it a suitable for an effect similar to MIET, which I will call graphene-induced energy transfer (GIET) in this thesis. Similar to MIET, calibration calculations were performed, assuming a graphene layer thickness of 0.34 nm and a complex-valued refractive index of $2.77 + 1.41i$ for an emission wavelength of 680 nm. A SiO_2 spacer (refractive index $n_{SiO_2} = 1.46$) with a thickness of 5 nm was deposited on the graphene. The calculated GIET curve shows that efficient lifetime modulation takes place in a distance range up to 30 nm away from the graphene surface 3.25. The calculations show the two cases of an emitter with its dipole orientated parallel and orthogonal to the surface, and for quantum yield values ranging from 0.1 and 1.0.

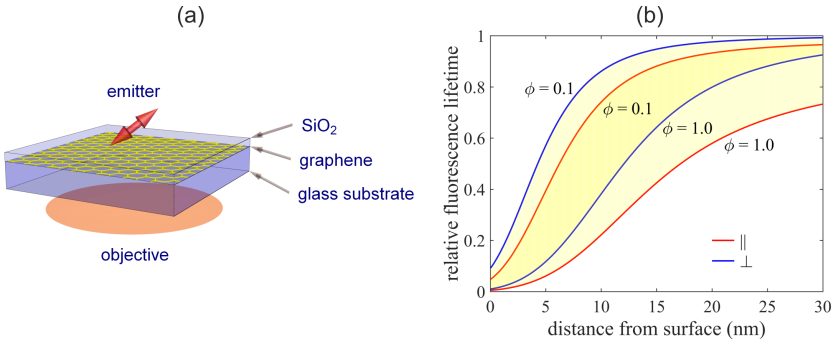

Abb. 3.25: ***(a)*** *Schematic of a GIET substrate. A silicon dioxide spacer is vapour-deposited on a single sheet of graphene to prevent complete quenching of an emitter.* ***(b)*** *GIET calibration curve shows the fluorescence lifetime modulation of an emitter as a function of its distance from the graphene layer, both for a dipole orientation perpendicular and parallel to the surface, and for quantum yield values between 0.1 and 1.0.*

Prior Knowledge of the QY was obtained by Alexey Chizhik with a nanocavity method [20]. Proof-of-principle experiments were performed by Arindam Ghosh using single dye molecules spin-coated on graphene substrates with

different SiO_2 spacer thickness values of 10 nm, 15 nm and 20 nm. Fluorescence lifetime images of the samples were taken. In these images, single molecules were identified and their single-molecule fluorescence decay curves were calculated. Absolute height values of the identified molecules from the surface were then extracted using the GIET calibration curves. The average number of detected photons for molecules on substrates with spacer thickness of 10 nm, 15 nm and 20 nm were 1,489, 4,786 and 6,033, respectively, showing the expected decrease in fluorescence due to quenching by graphene with increasing distance. Single molecule-fluorescence decay curves were tail-fitted with a mono-exponential decay function using a cutoff of 0.5 ns.
Fitted decay curves are shown in figure 3.26a along with histograms of all determined lifetime values for all three samples (see figure 3.26b). In all previously shown calculations, we assumed a fully random dipole orientation, which is usually correct for most samples where dye molecules are attached to their targets by highly flexible carbon linkers. In that case, dye molecules can rapidly rotating on timescales much smaller than the fluorescence decay time. However, for the immobilized molecules, this assumption is no longer valid. To determine the dipole orientation of the immobilized molecules, we used defocused imaging of single molecules [12, 103]. In figure 3.26c, measured defocused images of molecules on the graphene substrate are shown. From these images, a distribution $p(\theta)$ of emission dipole inclination angles θ with respect to the optical axis is extracted 3.26d. Using this distribution, one can calculate an orientation-averaged GIET curve using the equation

$$\langle \tau_f(z_0) \rangle = \int_0^{\pi/2} d\theta \sin\theta p(\theta) \tau_f(z_0, \theta) \tag{3.3}$$

The parameters used for the calculation of the GIET curve are the free-space lifetime $\tau_0 = 2.9$ ns and the quantum yield $\Phi = 0.2$. The resulting GIET calibration curve for the two dipole orientations parallel and vertical to the surface are shown in figure 3.26e. The yellow shaded region represents the corresponding polar angle distributions of θ shown in 3.26d, where the shading intensity represents the values of $p(\theta)$. The lifetime values of each molecule were converted into corresponding height values using the orientation-averaged GIET curve. In figure 3.26f, the histograms of the height values have mean values of 11 ± 3 nm, 16 ± 3 nm, and 21 ± 6 nm for the respective spacer thickness values of 10 nm, 15 nm, and 20 nm. As can be

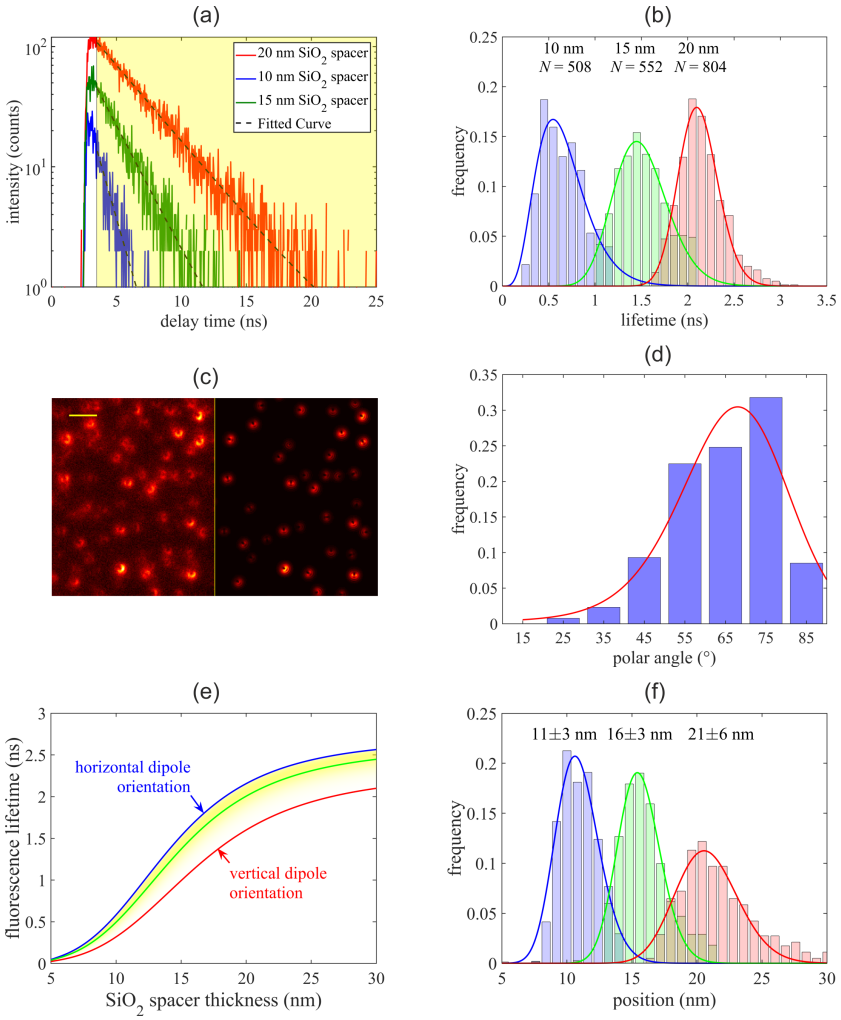

Abb. 3.26: ***(a)****Fluorescence decay curves of molecules on three different SiO_2 spacers with thickness values of 10 nm, 15 nm and 20 nm, on top of the graphene layer. For decay time determination, a maximum likelihood estimator was used with a cutoff time of 0.3 ns, as shown by the yellow shaded region.* ***(b)*** *Histogram of the tail-fitted lifetime values obtained by fitting the fluorescence decay curves of individual molecules. In the figure, N denotes the number of molecules that contributed to the histogram. The average number of detected photons per molecule increased with increasing spacer thickness, from 10 nm to 20 nm, showing the expected quenching by graphene. The histograms were fitted using a Γ-distribution.* ***(c)*** *shows the experimental wide-field defocused images of single Atto655 molecules spin-coated on a glass surface (left), and theoretical fits of the defocused images (right). Scale bar is 1 μm.* ***(d)*** *Histogram of the orientation distribution of immobilized molecules obtained from the defocused images in (c). Polar angle is the angle between the dipole and the vertical axis* *(continued on next page).*

Abb. 3.26: (Continuation from previous page) ***(e)*** *Calculated GIET curve for the two limiting dipole orientations, horizontal (blue) and vertical (red). The yellow shading represents a density plot of the orientation distribution from (d). The green curve is the orientation-averaged GIET curve which is then used for converting lifetime values to distance values.* ***(f)*** *Distance distributions obtained from converting each molecule's lifetime in (b) into a distance using the green GIET calibration curve in (e) (experiments and analysis by Arindam Ghosh).*

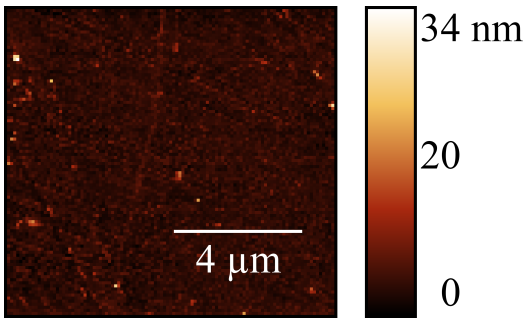

Abb. 3.27: AFM image of a graphene substrate with a 15 nm SiO_2 spacer vapour-deposited on it. The obtained root-mean-square value of roughness is 1.8 nm. The experiments were performed by Bastian from the lab of Andreas Janshoff.

seen, there exists a systematic bias of ∼1 nm towards larger distance values as compared to the values expected from the sample preparation. This deviation could be caused by two effects. The first is the surface roughness of the samples. We used atomic force microscopy to estimate the surface topology of the substrates and we found a significantly rough surface with root-mean-square values of surface roughness ranging from 1.5 nm to 2.1 nm (see figure 3.27). This could explain the observed broad dipole orientation distribution, which is much broader than seen in similar experiments for molecules deposited on flatter glass surfaces [63]. A second cause of the seen bias could be surface-induced heterogeneity of the photophysical parameters of the immobilized molecules. Previous studies have shown that surface-immobilized molecules can exhibit a broad range of quantum yield values [19].
Such a spread in QY values would further result in a broadening of the distance value distributions in figure 3.26f and could lead to a slight systematic bias of the average distance values as compared to the actual ones. However, it should emphasized that the relative distance increase from sample to sample (5 nm) is obtained correctly. Therefore, we can aptly use GIET for axial

co-localisation of emitters in the leaflets of an SLB.

4.1 Axial localization of labelled lipids in SLBs

SLBs were prepared on graphene substrates by vesicle fusion. SLBs composed of pure DOPC and DLPC were chosen. The alkyl chain length of DOPC is 18 carbon atoms, whereas that of DLPC is 12 carbon atoms. A low percentage of lipids fluorescently labelled with Atto655 were incorporated into the SLBs (see section 1 of this chapter). Fluorescence decay curves were acquired by scanning a 5 μm$\times$5 μm area.

The measurements were done in SLB regions showing a homogeneous fluorescence intensity in scan images taken prior to the GIET measurements (see figure 3.28a). For this purpose, a 60 μm$\times$60 μm area was scanned to check the quality of the bilayer. High-intensity spots seen in the scan image correspond to non-disrupted vesicles adsorbed to the surface.

Figure 3.28b shows the fluorescence decay curves for DOPC-SLBs prepared on graphene substrates with SiO_2 spacers of different thickness. The decay curves show an increasing fluorescence lifetime as when increasing the SiO_2 spacer thickness from 6 nm to 10 nm, due to the stronger fluorescence quenching by graphene surface for smaller spacer thickness values. For all bilayer experiments on graphene, the SiO_2 thickness was set to 10 nm, unless mentioned otherwise. Fluorescence decay curves of labelled lipids in DOPC- and DLPC-SLBs were fitted using a bi-exponential decay function as shown in figure 3.28. Fitting was done using the full measured decay curve and applying a deconvolution with the measured instrument response function (IRF). For the DOPC-SLB, we find lifetime values of 0.95 ± 0.07 ns and 1.81 ± 0.03 ns. The shorter lifetime component contributes 21 % to the full curve, while the longer component contributes 79 %. It should be mentioned that the amplitude ratio is in accordance with our expectation based on the previous results obtained for SLBs on ITO. Theoretically, in the case of the DLPC-SLB, the fluorescently labeled lipids in the bottom and top leaflets with lifetime values of 0.86 ± 0.14 ns and 1.56 ± 0.10 ns should have relative brightness amplitudes of 36 % and 64 %, respectively.

Additionally, fluorescence decay times were plotted as a function of the number N of recorded photons per TCSPC curve (see figure 3.29c for DOPC-SLB,

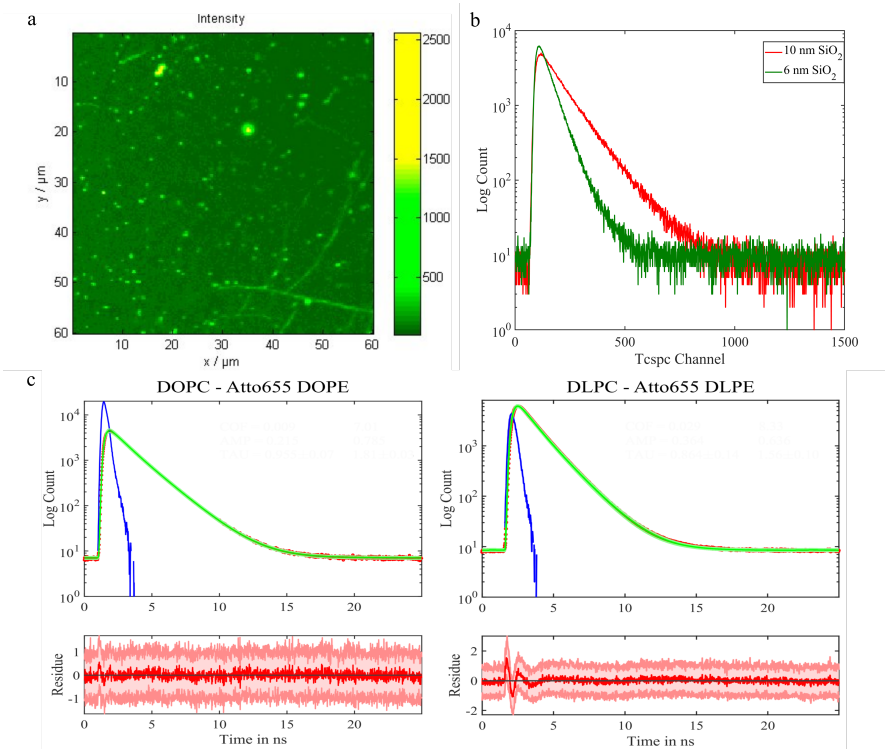

Abb. 3.28: ***(a)*** *Fluorescence intensity image of a SLB prepared on a graphene substrate, showing a homogeneous quality of the bilayer prepared by vesicle fusion. Few bright intensity spots are attributed to non-disrupted vesicles adsorbed to the surface.* ***(b)*** *Fluorescence decay curves recorded on a DOPC-SLB on a graphene substrate with SiO_2 spacers of 6 nm and 10 nm thickness. The 6 nm spacer shows a shorter fluorescence lifetime than the 10 nm spacer, demonstrating the strong quenching of the dye's fluorescence by graphene.* ***(c)*** *Fluorescence decay curves for a DOPC-SLB (left) and for a DLPC-SLB (right) on a graphene substrate with a 10 nm SiO_2 spacer. The decays were fitted with a bi-exponential fit function using a deconvolution with the instrument response function (IRF).*

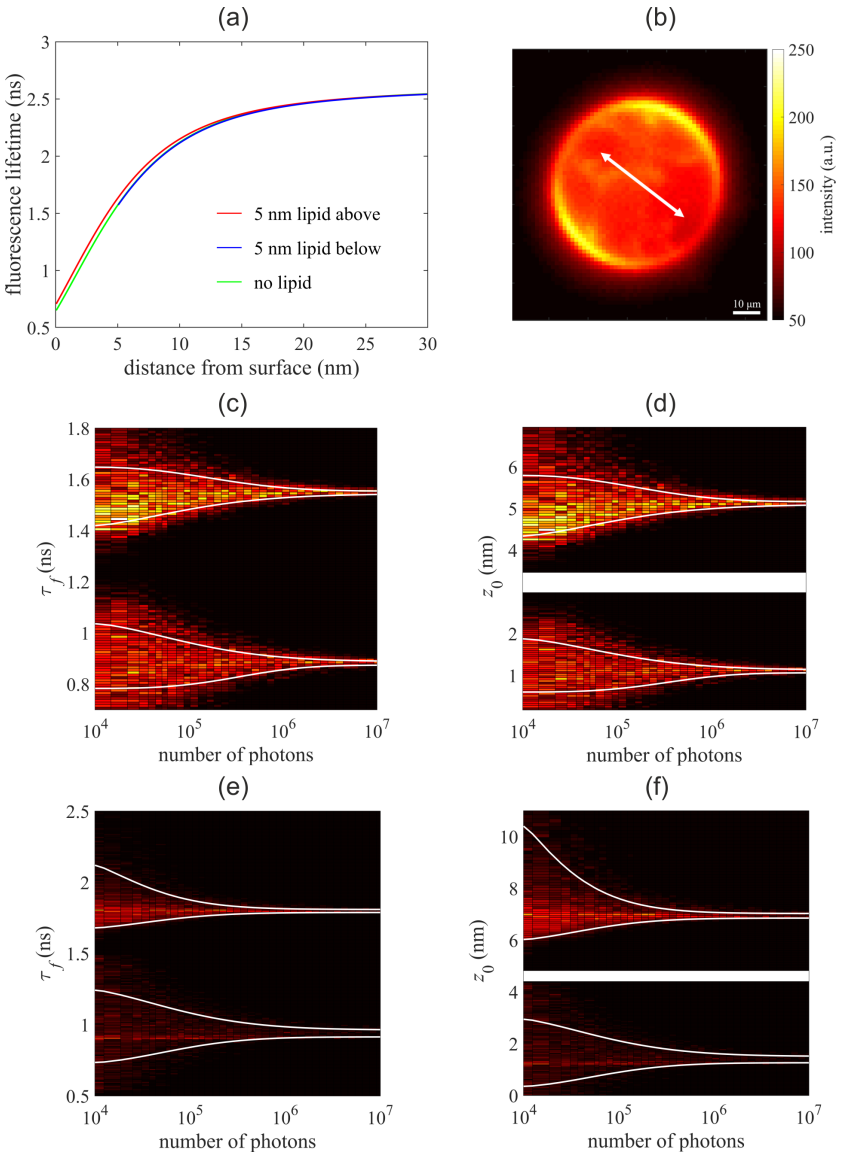

Abb. 3.29: ***(a)*** *Calculated GIET calibration curve, which takes into account the presence of a ∼5 nm thick bilayer having refractive index of 1.46. The GIET curve was calculated for three cases: (i) no bilayer present, (ii) with bilayer present above a dye, and (iii) with bilayer present below a dye.* ***(b)*** *A GUV imaged under linearly polarized excitation, with a polarization direction as indicated by the double arrow.* ***(c)*** *Lifetime distributions for a DLPC-SLB, plotted as a function of the number of photons per TCSPC curve. The white lines indicate standard deviations.* ***(d)*** *Distance distributions as a function of number of photons per TCSPC curve, obtained from (c) by converting lifetime values into distance values using the GIET curve from (a). All lifetime values longer than 1.25 ns were converted using the blue curve* *(continued on next page).*

Abb. 3.29: (Continuation from previous page) All shorter lifetime values were converted using the red curve. ***(e),(f)*** *Lifetime and distance distributions similar to those in (c) and (d) for a DOPC-SLB. For lifetime-to-distance conversion, we used the blue curve for lifetimes longer than 1.5 ns and the red curve for lifetimes shorter than 1.5 ns.*

and 3.29e for DLPC-SLB). The distributions were obtained by chopping the full measurement into bunches of N photons, and then fitting the obtained TCSPC curves. Similar to the previous experiments, to convert the obtained lifetime values into distance values, a GIET calibration curve had to be calculated for the specific substrate and sample geometry. In these model calculations, the presence of a bilayer with refractive index of 1.46 and an estimated thickness of 5 nm was taken into account.

However, additional information such as dye orientation and quantum yield had to be acquired from accompanying experiments. For this purpose, we prepared giant unilamellar vesicles (GUVs) with the same lipid compositions as used for the SLBs, and imaged them using linearly polarised excitation (λ =637 nm) on a wide-field microscope. Imaging was done with an EMCCD camera (Ixon Ultra 897, Andor Technology, Ireland), with an image exposure time of 1 s and an EM-gain of 30. The core idea of this experiment was to determine the fluorescence intensity distribution around the circumference of the GUV with respect to polarization direction. This intensity distribution contains information about the fluorescent dye orientation with respect to the GUV surface. Figure 3.29b clearly shows highest intensity for surface patches parallel to the excitation polarization (double arrow) which indicates that dyes are orientated parallel to the bilayer plane.

Nanocavity measurements by Alexey Chizhik were used to obtain the free-space lifetime and QY of labelled lipids in the SLBs. For Atto655-labelled DOPC-SLBs, a free-space lifetime of $\tau_0 = 2.6$ ns and a QY value $\Phi = 0.36$ were found. These values were then also used for DLPC-SLBs. The resulting GIET curve is shown in figure 3.29a, and this curve was then used to convert the lifetime values into distance values, see figure 3.29d and f, respectively. The shorter lifetime component is attributed to molecules in the bottom leaflet, and the corresponding lifetime values were converted using the GIET curve labelled as '5 nm lipid above.' Similarly, for the long lifetime component

(top leaflet), we used the GIET curve '5 nm lipid below.' As can be seen from figure 3.29(d,f), the relative width of the lifetime distributions becomes very small for a large number of photons per TCSPC measurement. The values for the dye positions were obtained from the highest photon numbers (right edge of figures at 10^7 photons), and we found dye distance values of 1.09 ± 0.04 nm and 5.13 ± 0.04 nm for the bottom and top leaflets of a DLPC-SLB, respectively. For a DOPC-SLB, the corresponding values were 1.4 ± 0.1 nm and 6.9 ± 0.1 nm. The distance between the top and bottom leaflets are 4.04 ± 0.06 nm for the DLPC-SLB, and 5.5 ± 0.2 nm for the DOPC-SLB. These values are in excellent agreement with literature values of 3.3 ± 0.07 nm for the head-group-to-head-group distance of a DLPC-SLB, and of 4.6 ± 0.2 nm for a DOPC-SLB [5, 69]. It should be noted that our values are slightly larger due to extra size of the fluorophores and the linker length between dye and lipid headgroup. Finally, the thickness of the hydration layer between the substrate and the bottom leaflet does also agree well with the DOPC literature value of 1.79 nm [142], when compared with our value of 1.4 ± 0.1 nm.

In summary, graphene shows a steeper lifetime-to-distance dependence which enhances the axial resolution of MIET from a few nanometers to the Å level. Moreover, graphene has demonstrated to be an excellent alternative to ITO for lifetime-dependent diffusion studies on SLBs. Moreover, the stability of graphene substrates is much better as compared to ITO which makes it a much better choice for further MIET experiments.

4.2 Lateral lipid diffusion in DOPC-SLBs

4.2.1 SLB preparation by vesicle fusion

I performed sFCS experiments for DOPC-SLBs on graphene substrates, similar to the previously reported ones using ITO-substrates. The used graphene substrate was covered with 10 nm thick SiO_2 spacer that was deposited on the graphene with chemical vapour deposition (CVD). SLBs were prepared using vesicle fusion. A FLIM image of a 60 μm$\times$60 μm area shows a heterogeneous SLB formation where the red region of $\sim$ 2.5 ns corresponds to intact vesicles (figure 3.30). A homogeneous region in the sample was carefully cho-

sen for sFCS measurement, and an autocorrelation analysis was applied to the recorded data.

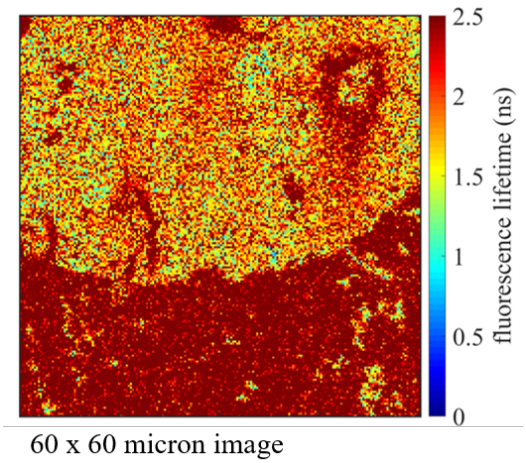

Abb. 3.30: FLIM image of a DOPC-SLB prepared by fusing 50 nm-sized vesicles on a graphene substrate. Larger lifetime values (red) in the image correspond to intact vesicles.

To avoid contributions from long-lifetime vesicles, I performed tail-fitting of the TCSPC curves, and the fitted curves were then used for the calculation of the FLCS filter functions. A third lifetime component (zero decay time) was added to account for constant background. Lifetime-specific ACFs were calculated using the FLCS algorithm and pre-determined filter functions.
The ACF associated to lipid diffusion in the bottom leaflet was fitted with the adsorption/desorption model while the ACF of lipid diffusion in the top leaflet was fitted using a two-species free diffusion model 3.31. The fit results are summarized in table 3.7. I find a value of 2.10 ± 0.17 $\mu m^2 s^{-1}$ for the diffusion coefficient in the bottom leaflet. A comparison of this value with the previously found diffusion coefficient of 0.79 ± 0.40 $\mu m^2 s^{-1}$ on ITO shows that the value measured on graphene is faster that than measured on ITO. This suggests a strong dependence of lipid diffusion in the bottom leaflet on interactions with the substrate. As I had found, the surface roughness on ITO is much larger than that on graphene substrates (see 3.12 and 3.27), so the different diffusion measurement results could be attributed to this roughness difference. For the top leaflet, fitting of the ACF with a two-species free diffusion model yields diffusion coefficient values of 4.38 ± 0.09 $\mu m^2 s^{-1}$ and 2.78 ± 0.70 $\mu m^2 s^{-1}$. These values are larger than the ones measured on ITO.

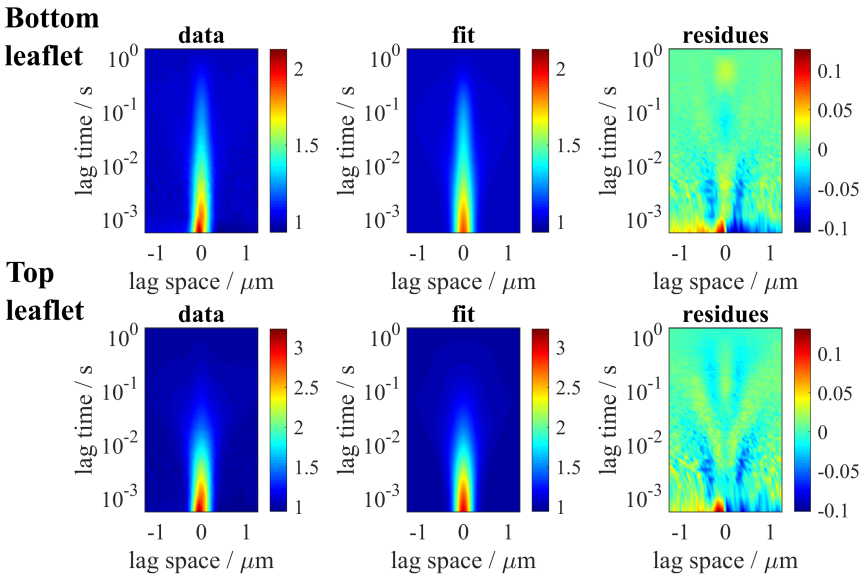

Abb. 3.31: 2D spatio-temporal ACF of lipid diffusion in a DOPC-SLB on a graphene substrate. The ACF associated with the bottom leaflet (top) is fitted using the adsorption/desorption model as discussed in detail in section 5.3. The fit is shown in the middle, and fit residues on the far-right. The top-leaflet ACF (below) was fitted with a two-species free diffusion model.

	bottom leaflet	**top leaflet**	
D (μm^{2}s^{-1})	2.10 ± 0.17	4.38 ± 0.09	2.78 ± 0.70
a (%)	100	77.3	22.7
k_+ (s^{-1})	1.05		
k_- (s^{-1})	2.96		

Table 3.7: Summary of fit results for the ACF associated with the bottom and top leaflets of a DOPC-SLB on a graphene substrate. The SLB was prepared using vesicle fusion. Given here are the diffusion coefficient D, FCS amplitudes a for each diffusion component, and adsorption k_+ and desorption k_- rate constants for the interaction between labelled lipid and the substrate.

A possible explanation for this larger diffusion coefficient value on graphene can be again the smaller surface roughness of the graphene sample, see figure 3.27. This results in a decrease of lipid interaction with the surface and will subsequently lead to less defects during SLB formation. Furthermore, the increase of the diffusion coefficient in the top leaflet indicates a possible

interaction between the two leaflets. Interestingly, the adsorption/desorption rates (k_+/k_-) per second are now reduced to 1.05/2.96 s^{-1} while I found a value of 15.72/53.15 s^{-1} on ITO.

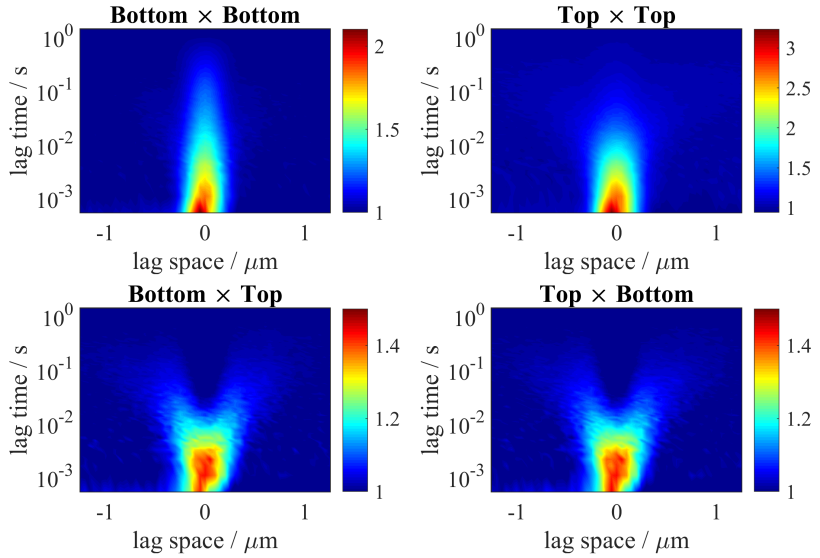

Abb. 3.32: ACFs associated with labelled lipid diffusion in bottom leaflet (bottom x bottom) and top leaflet (top x top). CCFs (bottom x top and top x bottom) show nearly ∼25 % cross-correlation amplitude.

Significant cross-correlation was found in all SLB experiments on graphene. CCF amplitudes of ∼25 % are seen. This could be an artifact due to improper sample preparation. The possibility that two labelled lipids in to the different leaflets do co-diffuse, thus leading to a non-zero CCF amplitude, is highly improbable for such a sparsely labelled samples. However, one possibility is inter-leaflet coupling or hindered diffusion (by defects that extend over both leaflets) as observed in SPT. Unfortunately, with the available data, I cannot make any conclusive statement about the validity of these assumptions. To ensure that SLB preparation is free from artifacts, I tried a different preparation technique, namely preparing SLBs using the Langmuir-Blodegtt (LB) method.

4.2.2 Supported lipid bilayer preparation by Langmuir-Blodgett

The Langmuir-Blodgett method has long been used for the preparation of high-quality lipid monolayers or bilayers. The method is described in detail in section 1. A prepared bilayer was first checked by FLIM, see figure 3.33, and there it can be seen that the formation of the top leaflet was incomplete, based on the known lifetimes of 0.95 ± 0.07 ns and 1.81 ± 0.03 ns that correspond to the bottom and top leaflets of a DOPC bilayer on graphene. This experiment can be used for control of complete SLB formation. Finally, sFCS experiments and analysis was performed on intact SLBs. As summarized in

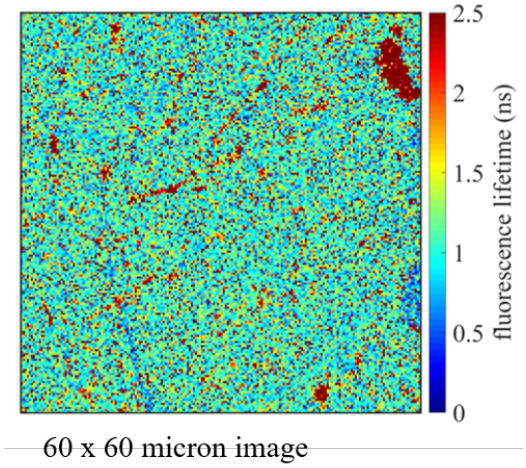

Abb. 3.33: FLIM image of DOPC-SLB prepared by the Langmuir-Blodgett method on a graphene substrate. The fluorescence lifetime image shows incomplete formation of top leaflet (red).

table 3.8, I obtain a value of 2.35 ± 0.50 $\mu m^2 s^{-1}$ for the diffusion coefficient of labelled lipids in the bottom leaflet of the DOPC-SLB. Lipid diffusion in the bottom leaflet shows similar diffusion coefficient values for both preparation techniques on graphene.

Fitting of the ACFs associated with the lipid diffusion in the top leaflet yields diffusion coefficients of 3.73 ± 0.04 $\mu m^2 s^{-1}$ and 0.26 ± 0.02 $\mu m^2 s^{-1}$. The presence of a slow lipid diffusion component in the top leaflet is expected from the FLIM image: Due to the partial formation of the top leaflet, I expect hindered lipid diffusion due to an increased number of defects in the top leaflet.

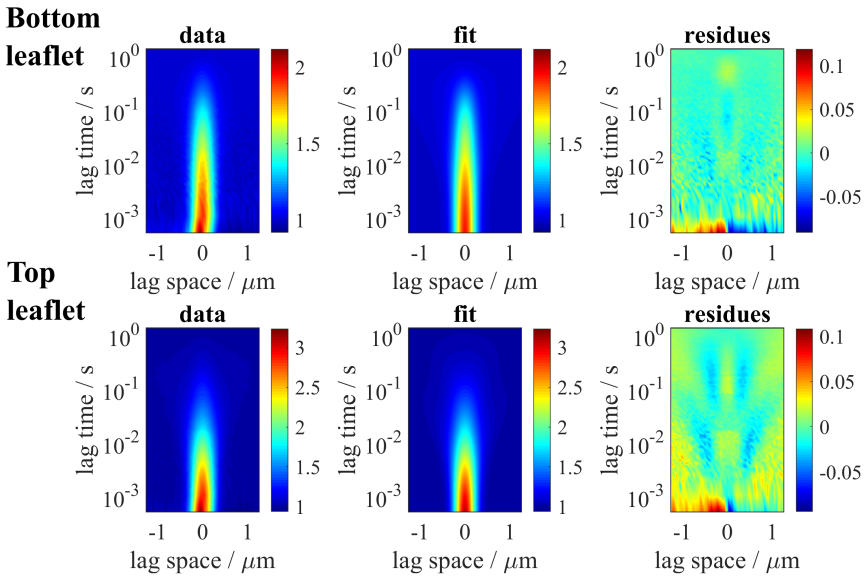

Abb. 3.34: ACF associated with labelled lipid diffusion in the top and bottom leaflets of a DOPC-SLB prepared by the Langmuir-Blodgett method. The ACF of the bottom leaflet (above) is fitted using an adsorption/desorption model as discussed in detail in section 5.3. The middle panel shows the fit, and the residues are shown in the right panel. The top-leaflet ACF (bottom) was fitted with two-species free diffusion model.

	bottom leaflet	**top leaflet**	
D ($\mu m^2 s^{-1}$)	2.35 ± 0.50	3.73 ± 0.04	0.26 ± 0.02
a (%)	100	68.5	31.5
k_+ (s^{-1})	6.71		
k_- (s^{-1})	6.37		

Table 3.8: Summary of fit results for FCS experiments of lipid diffusion in bottom and top leaflets of a DOPC-SLB. A Langmuir-Blodgett method was used for bilayer preparation on a graphene substrate. Given are the diffusion coefficient D, amplitude a of the corresponding diffusion component, and the rate constants k_+ and k_- for sticking and unsticking of labelled lipids to the substrate, respectively.

Additionally, I found a cross-correlation amplitude of ∼6 %. This amplitude is drastically smaller than the ones observed in my previous experiments on graphene, which implies that it is not significantly influenced by the presence of defects in the top leaflet. The absence of strong evidence for co-diffusion of lipids in different leaflets in a SLB does not support the notion of strong

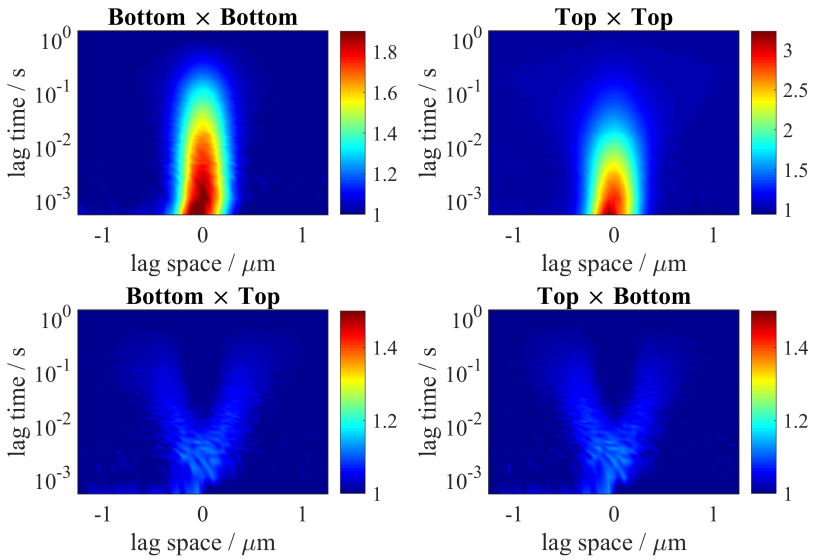

Abb. 3.35: ACFs and CCFs from FCS experiments on a DOPC-SLB on graphene. Shown here are the ACFs associated to the labelled lipid diffusion in bottom leaflet (bottom x bottom) and top leaflet (top x top). The CCFs (Bottom x top and top x bottom) show negligible ∼6 % cross-correlation amplitude.

inter-leaflet coupling.

4.3 Axial localization of single-molecules

SLBs were investigated at single molecule label concentrations. I prepared sparsely labelled SLB samples with such a low label density that individual single-molecule photon bursts could be identified and analyzed. The idea is to sort these photon bursts resulting from the diffusion of fluorescently labelled lipids through the detection area in a leaflet-resolving manner by using GIET. Axial localization of molecules in GIET is based on the conversion of the fluorescence lifetime into a spatial distance. For this purpose, the fluorescent lifetime of each bursts is determined and sorted into two populations corresponding to each leaflet of a SLB.

SLB composed of DOPC and headgroup-labelled-DPPE was prepared on graphene topped with a silicon dioxide spacer of 10 nm thickness. Point FCS measurements were performed on a homogeneous region of the sample by using a confocal microscope equipped with TCSPC electronics (see 1 for details). Recorded data was analysed using a Matlab routine written by Narain

Karedla. Only bursts containing a minimum of 50 photons were used for analysis (figure 3.36a). The combined fluorescence decay from all bursts was fitted with a bi-exponential decay function using a maximum likelihood estimator. From these fits, we extracted the exponential decay times for the two lifetime components corresponding to each leaflet. These decays were then compared with the fluorescence decay of each bursts using a pattern matching algorithm (non-negative Poisson iteratively reweighted least squares aka non-negative PIRLS) to obtain the amplitudes of the lifetime components in each burst. Using these amplitudes, each burst was then sorted into three populations: bursts with more than 75% amplitude of lifetime component 1, bursts with more than 75 % amplitude of lifetime component 2, and bursts in which the amplitudes of both lifetime components are less than 75 %.

The three populations are attributed to labelled lipids in the bottom leaflet, top leaflet, and a mixed population. The most likely explanation for the mixed population is the presence of more than one molecule in the focus. This could happen When labelled lipids in different leaflets are co-diffusing (inter-leaflet coupling), or when labelled lipids in different leaflets transit through the focus by chance independently. However, since the labelling concentrations were very low, the probability of finding several molecules transiting through the focus at the same time was extremely low.

Fluorescence decays of bursts associated with labelled lipids in the bottom leaflet are combined and fit with a mono-exponential decay function, and similarly for bursts attributed to labelled lipids in the top leaflet. For the mixed population, the combined fluorescence decay was fitted with a bi-exponential decay function as shown in figure 3.36c. The fit results yield a fluorescence lifetime of 0.96 ns for the bottom leaflet, 2.08 ns for the top leaflet, and the two values of 1.20 ns and 2.11 ns for the mixed population. These values are in good agreement with the previously found lifetime values of 0.95 ± 0.07 ns and 1.81 ± 0.03 ns for DOPC-SLB at higher labelling concentration.

Additionally, we calculated the average countrate of these three populations shown in figure 3.36d. The mixed population shows higher countrates as compared to the other two, the bottom and top leaflet populations, which supports our assumption that the mixed population comprises bursts that were generated by more than a single molecule.

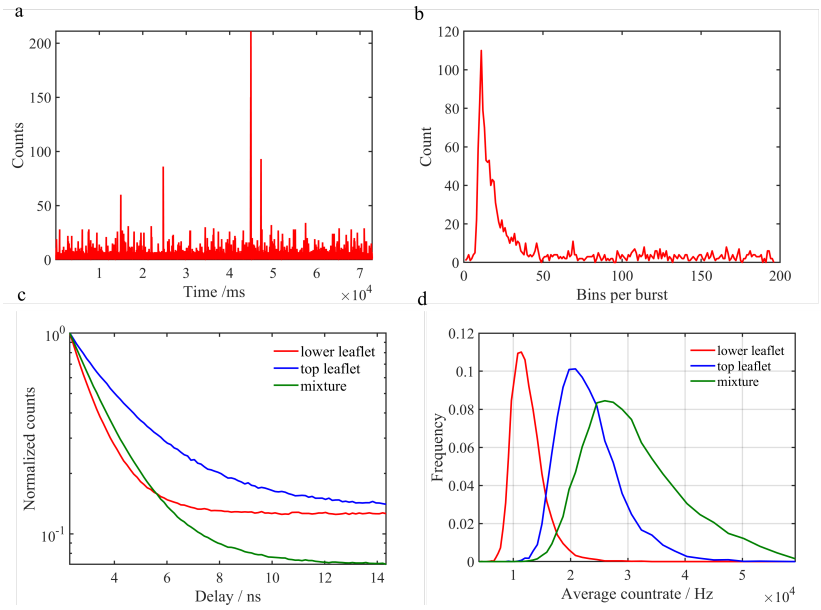

Abb. 3.36: ***(a)*** *Single-molecule bursts were identified from intensity-time traces.* ***(b)*** *Fluorescence decay of a single burst. Only bursts having a minimum of 50 photons were used for analysis.* ***(c)*** *Combined fluorescence decay of all bursts attributed to the bottom leaflet, top leaflet, and a mixed population.* ***(d)*** *Average countrate for the three populations (bottom leaflet, top leaflet, mixed). The higher countrate of bursts in the mixed population supports our assumption of having more than one molecule in these bursts.*

4.4 Conclusion

In summary, I found higher lipid diffusion coefficients in the bottom leaflet of SLBs on graphene as compared to those on ITO. I complemented this observation with AFM measurements of ITO 3.12 and graphene 3.27 samples. The graphene sample surface has a roughness root-mean-square value of 1.8 nm, while ITO has 2.3 nm. The difference in lipid diffusion in the bottom leaflet shows a strong influence on surface topology. The diffusion of labelled lipids in the top leaflet was best fit using a two-component free diffusion model. For SLBs with a top leaflet formation containing many defects, I found a slow diffusing component of nearly $\sim 0.2-0.7\ \mu\mathrm{m}^2\mathrm{s}^{-1}$, which implies that the slow lipid diffusion in the top leaflet mainly originate from the defects. Moreover, I observed significant CCF amplitudes which indicate the possibility of lipid co-diffusion (inter-leaflet coupling) across the leaflets. Due to sparse labelling, the probability that two labelled lipids co-diffuse through

the detection area by chance is low. Therefore, the origin of the observed cross-correlation is not fully clear. Additionally, I found a mixed population from single-molecule burst experiments which imply the simultaneous transit of several molecules through the focus. This could hint at lipid co-diffusion across the two leaflets.

CHAPTER 4

Transmembrane β-peptide at membrane surface

Double stranded DNA has found many applications as a molecular ruler due to the high order of its repetitive sequence in a double-stranded helix, high rigidity of its secondary backbone structure, and the available of side chain functionalizations [88, 135]. A similar system with only one helical strand are β-peptide helices that can serve as an interesting alternative for molecular rulers [41]. β-peptides are well known for their stability, highly rigid secondary structure, large helical persistence length, well-defined spacing, and options for side chain functionalization [114, 100, 113]. The secondary structure of β-peptides can be modified by using different combinations of amino acids. The possibility to precisely localise probes on the nanometer length scale has opened the window for many studies of physiological processes in model systems and in cells [59, 42]. A spatially well-defined probe opens the possibility of exploring defined distances reachable by the probe [33, 2]. In this section, I describe a membrane-proximal molecular ruler that can potentially be used for defining distances from a membrane interface. This molecular ruler can have significant importance for revealing proton or calcium ion gradients along a membrane surface, which play a crucial role in SNARE protein-mediated membrane fusion [77] or in distance-dependant membrane studies along the membrane surface and its immediate environment.

In my study, the β-peptide helices were anchored in model SLBs, and their distances to the membrane surface were determined using GIET. This work has been done in collaboration with the group of Ulf Diederichsen and was published in the Journal of Peptide Science [66].

1 Molecular structure

Membrane proteins are crucial for all vital processes of life, and membrane proteins constitute almost a third of all human proteins [99]. The functionality of membrane proteins is mainly governed by their structural conformation. Different secondary structures for native peptides are well known, among them are α-helices and β-sheets the most common ones [67].

Due to the low stability of α-peptides, a well-established class of peptidic model systems was introduced. β-peptides are examples of such model systems. In general, β-peptides are artificial mimetics of α-peptides. The structural difference between the two is an additional methylene (-CH_2) group in the amino acid backbone of β-peptides [18]. Well-defined β-peptide structures can be obtained by modulating the amino acid sequence along the peptide chain, but a 14-helix structure of β-peptides has shown to be most suitable for applications as molecular ruler. The 14-helix structure is a highly stable conformation consisting of three amino acid residues per turn which results in a length increase per residue of 1.56 Å.

Earlier studies by the group of Ulf Diederichsen have reported about the potential use of β-peptide 14-helices with nonpolar homovaline amino acid residue sequences for forming transmembrane domains in model lipid bilayers [113, 114, 100]. These studies showed clear evidence for the incorporation of these β-peptide helices into a lipid bilayer, while the 14-helix conformation remains intact which was shown by X-ray and CD spectroscopy. The anchoring of these β-peptides was supported with two β^3-D-homotryptophan residues on the side chains that interact with the lipid head groups of a membrane [26, 65, 27]. For a successful incorporation of the synthesized peptides into a membrane, 19 amino acid long β^3-D-homovaline (Val) was chosen for forming the hydrophobic core, and two hydrophilic β^3-D-homolysines (Lys) were added to the ends to ensure general solubility for better handling of these

peptides (figure 4.1). The structural synthesis and analysis was performed by Martin Kloos.

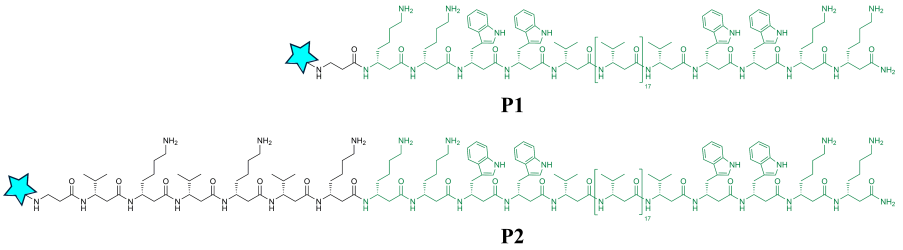

Abb. 4.1: Chemical structure of transmembrane β-peptides P1 and P2. Regions incorporated into the membrane are shown in green and the covalently attached Atto643 dye is shown in blue.

Two transmembrane β-peptides P1 and P2 of different lengths were synthesized and incorporated into large unilamellar vesicles (LUVs) composed of DOPC. Structural analysis of the peptide was done with X-ray and EPR spectroscopy showed a tilt angle of 16 ° in for a bilayer thickness of 27-29 Å. The conformational structure of β-peptides is assumed to remain highly stable even outside the membrane. This assumption was supported by CD spectroscopy of β-peptides in water, suggesting an elongated 14-helix structure [100].

The 14-helical β-peptides P1 and P2 were incorporated into supported lipid bilayers. These two peptides differ in the length of the regions that extend out of the membrane. I used GIET for measuring the position of the peptide termini with respect to the membrane.

Materials and methods

Giant unilamellar vesicles (GUVs) were obtained by drying 59 μl of peptide/lipid mixture (59 μl of 10 mg/ml DOPC in chloroform, P/L 1:25000) at 30 °C on an aluminum electrode under reduced pressure. The resulting lipid film was rehydrated with 300 mM of 500 μl sucrose solution and treated with 15 Hz alternating current for 3 h with a peak-to-peak voltage of 1.6 V in a custom build elctroformation chamber. Later the frequency of the AC is reduced to 8 Hz, 30 min. The resulting GUV solution was diluted with PBS buffer (500 μl). GUVs were spread by 30-fold dilution of the vesicle solution and added to a graphene substrate (Graphene Supermarket, New

York, USA). After 1 h, the resulting bilayer was washed carefully with PBS buffer to remove excess vesicles from the surface.

2 Results and discussion

P1 and P2 transmembrane peptides were designed to investigate the membrane environment at different heights with respect to the bottom leaflet. In the P1 peptide, only one β-alanine and Atto643 dye are outside the membrane, while the P2 transmembrane peptide extends by six β-amino acid plus a β-alanine and Atto643 dye above the membrane surface (as demonstrated in figure 4.2a). The P2 transmembrane peptide contains an alternating sequence of β^3-D-homovalines and β^3-D-homolysines that extends above the membrane. This combination of amino acid promotes solubility along with 14-helix formation [100]. Considering the 14-helix structure and the X-ray result of the 16 ° tilt angle, we calculate the theoretical height of the dye in P1 in DOPC to be 4.42 nm, whereas it is for P2 5.36 nm [113, 114, 17].

I applied GIET to localize the fluorescent dyes in labelled peptides incorporated into an SLB. Low concentrations of Atto643-peptide were used in DOPC-SLBs on a graphene substrate. Fluorescence decay curves were recorded by scanning an area of 5 μm×5 μm with a custom-build laser scanning confocal microscope (see 1). The setup is equipped with a 640-nm wavelength pulsed excitation laser, a single-photon avalanche photodiode detector (SPAD), and a time-correlated single-photon counting (TCSPC) electronics unit. The pulsed laser repetition rate was 20 MHz, the laser pulse width was ∼50 ps, and the temporal resolution of TCSPC electronics was 16 ps. The total scan time for each image was 400 ms, and each image consisted of 200×200 pixels. Images were taken with total excitation power of 20 W. The measurements were repeated three time for three different sample areas to obtain sufficiently precise lifetime data. These repetitions were then used for calculating measurement errors. The fluorescence decay curves were fitted with a three-exponential decay function using a maximum likelihood estimator, where the third component takes in account the free-space lifetime of the dye in solution, see figure 4.2b. Using the GIET curve shown in figure 4.2d, the lifetime values were converted into distance values. For

the calculation of the GIET curve, knowledge of the free-space lifetime and QY of the dye bound to peptide in the membrane environment was required. An independent TCSPC measurement was done to determine the free-space lifetime of the dye-peptide construct in the membrane supported on glass, yielding a free-space lifetime value of 4 ns. I calculated the QY value of peptide-Atto643 to be 0.71, by comparing the obtained free-space lifetime with the known lifetime of 3.5 ns and QY value of 0.62 for the dye in aqueous solution, assuming again that lifetime and QY are inversely proportional. Additionally, for the calculation of the GIET curve, I took into account the presence of the bilayer, assuming that it has a refractive index value of 1.46 and a thickness of $\sim$5 nm. The model calculation do also take into account that the graphene layer thickness is 0.34 nm and that its complex-valued refractive index of $2.77 + 1.42i$ at the fluorescence emission wavelength of 690 nm. A 10 nm thick silicon dioxide layer with a refractive index of 1.46 on top of the graphene was also taken in account. I assumed that the dye is randomly oriented in the sample, which was supported by images of the peptide incorporated into GUVs that were recorded by using linear polarized excitation. These images show a homogeneous fluorescence emission throughout the whole ring (figure 4.2c).

The calculated GIET curve is shown in Figure 4.2d, and it was used for converting the experimentally measured fluorescence lifetime values into axial distance values. Measured fluorescence decay curves together with their fits are shown in 4.2b. Assuming a fully random dye orientation, I found the following values for dye axial positions: For the P1 transmembrane peptide in a DOPC-SLB, the dye axial positions were found to be 2.90 ± 0.30 nm and 8.40 ± 0.10 nm, corresponding to the two possible positions of the dye below and above the bilayer. For the P2 transmembrane peptide, I found the corresponding values of 1.70 ± 0.03 nm and 7.90 ± 0.27 nm. The difference of the positions for the dye in P1 and P2 below the membrane is probably caused by the different lengths of P1 and P2, although it is not fully clear how such a difference arises, when both fluorophores were attached to the N-terminal of the peptides. Nonetheless, from the obtained distance values, I find an axial end-to-end distance between dye positions at both ends of a peptide of 5.5 ± 0.4 nm for P1 and 6.2 ± 0.2 nm for P2. These results are in agreement with reported end-to-end axial distance values of 5.5 ± 0.2 nm

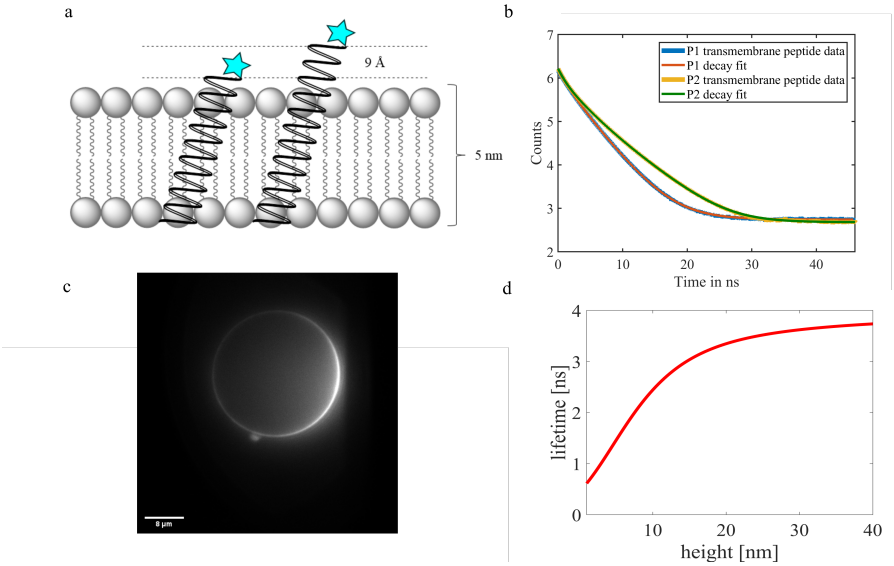

Abb. 4.2: ***(a)*** *Schematic representation of the transmembrane β-peptides P1 and P2 differing in their helix extension outside the membrane's hydrophobic core. The rigid 14-helix structure guarantees a fixed distance of the fluorophore (blue star) to the membrane surface.* ***(b)*** *Measured TCSPC decay curves and fits for the P1 and P2 peptides.* ***(c)*** *Fluorescence image of a GUV with P1 peptide incorporated under linear polarized excitation. This image supports the assumption of a random orientation of dyes in the sample.* ***(d)*** *Calculated GIET curve that was used to convert the measured fluorescence decay times, see panel (b), into axial distance values.*

in a DOPC-SLB [45]. I compared my results with the theoretically expected values of 4.42 nm for P1 and 5.36 nm for P2 that take the tilt angle of 16 ° into account. My measurements show slightly larger values due to the additional linker and the size of the dye, but are in excellent agreement with the theoretical estimates. These results indicate that the P2 peptide retains its rigidity in the aqueous environment above the DOPC bilayer.

3 Conclusion

In this work, I performed GIET measurement to determine the axial distances of the fluorophore Atto643 attached to the N-terminus of two transmembrane peptides above and below the membrane. I could show that these β-peptides are anchored in a well-defined manner into the model SLBs. The results indicate that the membrane-external parts of the β-peptides retain their conformational rigidity even in the hydrophilic outer-membrane environment.

This study recommends the use of β-peptide helices as molecular rulers in model membrane systems. The highly rigid 14-helix backbone structure allows to probe locations at well-defined distances from a membrane surface. These molecular rulers will have potential applications for studies where the membrane surface and its immediate environment require investigation. For example, one application could be the determination of proton or calcium ion flux along a membrane as a function of distance from the membrane surface, or pH-based analysis of healthy and diseased cell *in vivo* or *ex vivo* [3]. These rulers open vast application possibilities due to the possibility to functionalize their side chains.

CHAPTER 5

Localization of Gb_3-PEG3/13-dye near a membrane surface

Biological membranes contain hundreds of different kinds of lipids. Among them is the class of glycosphingolipids (GSL). They are preferentially found in the outer leaflet of the plasma membrane and have the tendency to form raft domains in biological membranes [144, 132]. These domains are usually formed by glycosphingolipids together with cholesterol and sphingomyelin. These rafts have sizes of typically 10-200 nm and exhibit a tighter lipid packing. Studies of these domains mainly use artificial membrane models that comprise mixtures of low-melting glycerophospholipid, sphingomyelin and cholesterol. These model membranes mimic the lipid phases found in the outer leaflet of plasma membranes, where one observes liquid-disordered (L_d) and liquid-ordered (L_o) phases. In the (L_d) phase, the lipid molecules are loosely packed due to predominance of unsaturated acyl chains, resulting in a fast lateral lipid diffusion. In contrast, the L_o phase has a tighter lipid packing.

Glycosphingolipids serve as receptors for antigen/microbial recognition and cell adhesion. They exhibit specific interactions with Cholera toxins and Shiga toxins, with receptors GM1 and Gb_3. Therefore, they act as gateways in the membrane epithelial cells due to their specific interactions with pathogen-generated proteins. These interactions have serious consequences

for infectious diseases [146]. Thus, in-depth characterisation of glycosphingolipids is of high interest. Although the headgroups of glycosphingolipids show specific interaction with proteins like Shiga toxin, some recent studies suggest that labelling of Glycosphingolipids with bulky fluorophores either at their headgroup or in the fatty acid chain influences the position of these fluorescent analogues in a membrane [92, 124, 54]. These fluorescent analogues are prevented from entering the tightly packed L_o phase as a result of their large size, while naturally occurring Gb_3 is anchored in the L_o phase. Thus, shifting the bulky fluorophore away from the membrane surface becomes crucial.

Labelling these molecules with fluorophores via long PEG linker should reduce fluorophore-membrane interactions. In this study, I use GIET for investigating two fluorescently labelled Gb_3 analogues with different PEG linkers between Gb_3 and the fluorophore. I determine the axial distances of the fluorescent dye molecules from the supported lipid bilayer interface.

1 Molecular structure

Glycosphingolipids are a class of membrane lipids that are composed of a glycan structure attached to a ceramide molecule. The basic structure does usually have a glucose or galactose attached to the sphingolipid ceramide, which can also be extended by additional monosaccharides, thus resulting in an amphiphilic molecule. The ceramide tail can also vary considerably, the fatty acid chain length does usually range from C_{14} to C_{24} and shows a diversity in degree of saturation and hydroxylation.

Gb_3 (C_{24}:0) molecules conjugated to bodipy-FL fluorescent dye with PEG linkers of different lengths were obtained from the group of Daniel B. Werz (Figure 5.1). A 24 carbon long fatty acid chain was chosen to mimic the naturally occurring Gb_3 molecule [85]. The PEG linker length was chosen in such a way to reduce the interaction of the dye with the membrane and thus improve the L_o phase partitioning of Gb_3.

These headgroup-labelled Gb_3 glycosphingolipids were designed in such way that the attached fluorophore does not influence their binding properties to STxB. To ensure this, the fluorophore is attached to the 2'-OH group of the

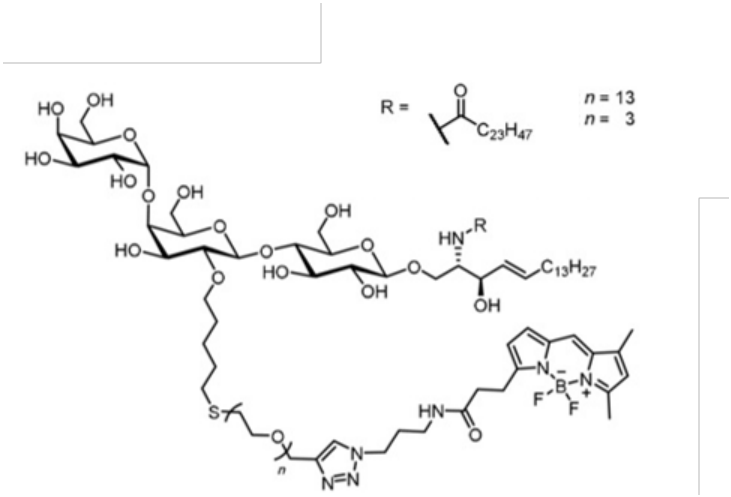

Abb. 5.1: Chemical structure of Gb_3 (C_{24}:0) labelled with bodipy-FL fluorescent dye.

middle galactose of the Gb_3 moiety with an oligoethylene glycol (PEG) linker [131].

Methods and materials

Giant unilamellar vesicles (GUVs) composed of DOPC and 5 % fluorescently labelled Gb_3 molecules were prepared using electroformation in a custom-build chamber, similar to the preparation mentioned in the previous section (see 1 of chapter 4). The obtained GUVs were spread on a graphene substrate (Graphene Supermarket, New York, USA) after 30-fold dilution with PBS buffer. The sample was incubated at 50 °C to initiate fusion. After 1 h, the sample was washed carefully with PBS buffer to remove intact GUVs. Some bilayers for the experiments were prepared by Larissa Socrier from the group of Claudia Steinem.

2 Results and discussion

Gb_3 (C_{24}:0)-PEG3-bodipy-FL and Gb_3 (C_{24}:0)-PEG13-bodipy-FL were designed to investigate possible interactions of the bulky headgroup label with the membrane interface which might alter the phase partitioning of these fluorescently labelled molecules. Using GIET, we determine the distances of bodipy-FL molecules incorporated into DOPC-SLB. Fluorescent decay curves were obtained by scanning an area of 5 μm×5 μm with a custom-built laser

scanning confocal microscope equipped with TCSPC electronics. A 488 nm wavelength pulsed excitation source and a single-photon avalanche photodiode detector (SPAD) were used for the measurement. Laser repetition rate was 20 MHz, laser pulse width was ∼50 ps. The TCSPC temporal resolution was 16 ps. A total scan time of 400 ms was used for each image, consisting of 200×200 pixels. The total excitation power on the sample was 20 W. More than a million photons were collected to obtain precise lifetime data. Error calculations were done using three independent measurements on a sample. Fluorescence decay curves were first time-gated and then tail-fitted (cutoff of 0.3 ns) with a bi-exponential decay function using a maximum likelihood estimator. For the calculation of the GIET curve, knowledge of the free-space lifetime and QY of the dye-labelled Gb_3 was required, for which independent TCSPC measurements were done. We obtained free-space lifetime of 4.9 ns for dye-Gb_3 in an SLB on glass. The QY value was calculated to be 0.82, by comparing the measured free-space lifetime with the known lifetime (5.7 ns) and QY (0.95) of the dye in aqueous solution. For the calculation of the GIET curve, the presence of the bilayer with refractive index of 1.46 and a thickness of ∼5 nm was taken into account. The thickness and refractive index of single-sheet graphene was 0.34 nm and $2.77 + 1.42i$ at the fluorescence emission wavelength of 520 nm. the presence of a 9 nm thick silicon dioxide layer with 1.46 refractive index on the surface of the graphene was also included in the calculation. Finally, we assumed a fully random orientation of the dye molecules.

Using the calculated GIET curve shown in figure 5.2b, the experimental lifetime values were converted into axial distance values. For the Gb_3-PEG3 in DOPC-SLB, the found dye distances were 2.28 ± 0.12 nm and 7.82 ± 0.25 nm, corresponding to the two possible positions of the dye below and above the bilayer. For the construct with PEG13 linker, the axial dye positions were found to be 2.04 ± 0.24 nm and 9.01 ± 0.29 nm, again corresponding to the two possible positions of the dye below and above the bilayer. The difference in distance values for the dye below and above the bilayer was 5.5 ± 0.1 nm for Gb_3-PEG3, and 6.9 ± 0.04 nm for Gb_3-PEG13. The axial distance for Gb_3-PEG3 is in excellent agreement with a reported value of 5.36 nm for headgroup-labelled DOPC. This suggests that for the PEG3-linker the dye molecule lies close to the membrane surface. However, for the

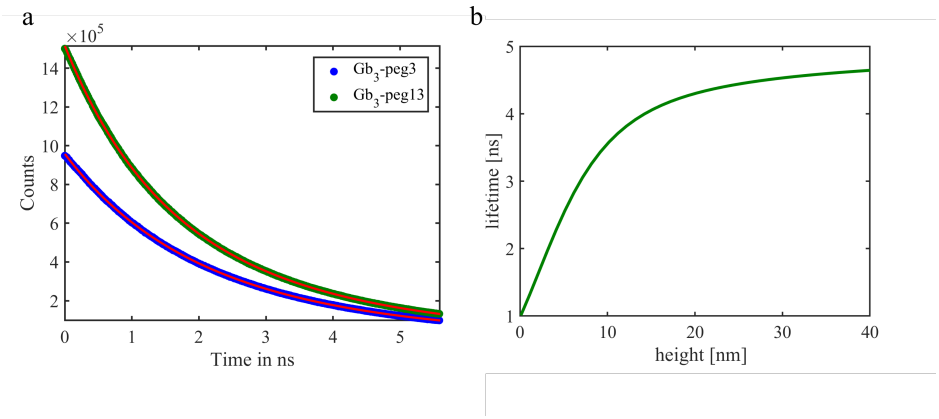

Abb. 5.2: ***(a)*** *Fluorescence decay curve fitted with a bi-exponential decay function using MLE.* ***(b)*** *Calculated GIET curve. The calculation takes into account the presence of a bilayer of ∼5 nm thickness and refractive index 1.46. The presence of the single-sheet graphene with thickness 0.34 nm and complex-valued refractive index of* $2.77+1.42i$ *as well as the* SiO_2 *spacer with thickness of 9 nm and refractive index of 1.46 at the fluorescence emission wavelength of 520 nm was also included in the calculation.*

PEG13 construct, the results indicate that the dye molecule is by ∼1.4 nm away from the membrane surface. This supports previous studies that found that a shorter PEG linker influences the partition of Gb_3 in the different membrane phases (L_o/L_d), while a longer PEG linker leads to less interaction with the membrane [131].

3 Conclusion

I used GIET to localize fluorescent bodipy-FL labels on Gb_3 molecules that were attached to Gb_3 via PEG linkers of 3 and 13 molecules. My results indicate that dyes attached via PEG13 linkers cause minimum perturbation to a membrane. This makes Gb_3-PEG13 analogues a suitable candidate for phase separation studies, or for investigations of the interaction between Gb_3 and Shiga toxin.

CHAPTER 6

Conclusion

In this work, I investigated the leaflet-dependent localization and diffusion of molecules in supported lipid bilayers using metal-induced energy transfer. In Chapter 3, I used metal/graphene-induced energy transfer (MIET/GIET) to localize fluorescently labelled lipid in the bottom and top leaflet of supported lipid bilayers. The axial resolution of a conventional confocal fluorescence microscope (ca. 500 nm) is usually smaller than its lateral resolution (ca. 200 nm, and this relation of axial to lateral resolution still remains at this value of $\sim$3 even for super-resolution techniques like STED, STORM or PALM. With GIET, we achieve sub-nanometer axial resolution which allowed me to resolve the ~ 5 nm thickness of a single lipid bilayer.

I determined the end-to-end distance of headgroup-labelled lipids in the bottom and top leaflets of a bilayer. I found a distance of 4.04 ± 0.06 nm for DLPC-SLBs, and of 5.5 ± 0.2 nm for DOPC-SLBs. We combined MIET/GIET with scanning-FCS to study lipid diffusion in SLBs in a leaflet-resolving manner. I performed sFCS experiments on two different substrates, ITO and graphene. My results indicate a strong influence of the substrate on lipid diffusion in the bottom leaflet. I attribute this to adsorption and desorption of labelled lipids to/from the substrate. I fitted measured FCS curves of lipid diffusion in the bottom leaflet with a model that takes this adsorption/desorption into account, and I determined the rate constants for

the adsorption and desorption. I found that the slow diffusion of lipids in the top leaflet does mainly originate from bilayer defects. Although the method allowed me to investigate SLB systems in-depth, the observation of significant cross-correlation between fluorescence signals coming from different leaflets requires additional experiments. Using single molecule burst detection, I found a mixed population of single molecule events associated with both leaflets, although the results do not substantiate the observed cross-correlation.

In chapter 4, I incorporated highly stable and rigid 14-helix transmembrane β-peptides into SLBs and determined the axial distance of dye molecules attached to the N-terminal of the peptide in the bottom and top leaflet of the SLB using GIET spectroscopy. The transmembrane peptides P1 and P2 were designed to investigate the membrane environment at different heights with respect to the bottom leaflet. I found that the peptides retain their conformational rigidity even outside membrane, thus being potentially useful as molecular rulers in membrane studies.

In chapter 5, I determined the axial distance of the Gb_3 molecules in the bottom and top leaflets of an SLB using GIET spectroscopy. Gb_3 molecules were labelled with bodipy-FL dyes via PEG linkers of 3 and 13 carbon atom length. Previous studies of these molecules showed that the close proximity of the dye to the membrane molecule hinders the partitioning of Gb_3 into the L_o phase of a membrane. Using GIET, I determine the dye-membrane distance of dye molecules conjugated to Gb_3 via a PEG13-linker and found that their distance was significantly larger than for dye conjugation with PEG3 linkers.

Bibliography

[1] E. Abbe. Contributions to the theory of the microscope and microscopic perception. *Archive for microscopic anatomy*, 9(1):413–468, 1873.

[2] F. Abendroth, A. Bujotzek, M. Shan, R. Haag, M. Weber, and O. Seitz. Dna-controlled bivalent presentation of ligands for the estrogen receptor. *Angewandte Chemie International Edition*, 50(37):8592–8596, 2011.

[3] M. Anderson, A. Moshnikova, D. M. Engelman, Y. K. Reshetnyak, and O. A. Andreev. Probe for the measurement of cell surface ph in vivo and ex vivo. *Proceedings of the National Academy of Sciences*, 113(29):8177–8181, 2016.

[4] D. Aquino, A. Schönle, C. Geisler, C. v Middendorff, C. A. Wurm, Y. Okamura, T. Lang, S. W. Hell, and A. Egner. Two-color nanoscopy of three-dimensional volumes by 4pi detection of stochastically switched fluorophores. *Nature methods*, 8(4):353–359, 2011.

[5] S. J. Attwood, Y. Choi, and Z. Leonenko. Preparation of dopc and dppc supported planar lipid bilayers for atomic force microscopy and atomic force spectroscopy. *International journal of molecular sciences*, 14(2):3514–3539, 2013.

[6] K. Bacia, S. A. Kim, and P. Schwille. Fluorescence cross-correlation spectroscopy in living cells. *Nature methods*, 3(2):83–89, 2006.

[7] N. Bag, J. Sankaran, A. Paul, R. S. Kraut, and T. Wohland. Calibration and limits of camera-based fluorescence correlation spectroscopy: a supported lipid bilayer study. *ChemPhysChem*, 13(11):2784, 2012.

[8] D. Beckers, D. Urbancic, and E. Sezgin. Impact of nanoscale hindrances on the relationship between lipid packing and diffusion in model membranes. *The Journal of Physical Chemistry B*, 124(8):1487–1494, 2020.

[9] A. Benda, M. Beneš, V. Marecek, A. Lhotskỳ, W. T. Hermens, and M. Hof. How to determine diffusion coefficients in planar phospholipid systems by confocal fluorescence correlation spectroscopy. *Langmuir*, 19(10):4120–4126, 2003.

[10] E. Betzig, G. H. Patterson, R. Sougrat, O. W. Lindwasser, S. Olenych, J. S. Bonifacino, M. W. Davidson, J. Lippincott-Schwartz, and H. F. Hess. Imaging intracellular fluorescent proteins at nanometer resolution. *Science*, 313(5793):1642–1645, 2006.

[11] F. Blachon, F. Harb, B. Munteanu, A. Piednoir, R. Fulcrand, T. Charitat, G. Fragneto, O. Pierre-Louis, B. Tinland, and J.-P. Rieu. Nanoroughness strongly impacts lipid mobility in supported membranes. *Langmuir*, 33(9):2444–2453, 2017.

[12] M. Böhmer and J. Enderlein. Orientation imaging of single molecules by wide-field epifluorescence microscopy. *JOSA B*, 20(3):554–559, 2003.

[13] M. Böhmer, M. Wahl, H.-J. Rahn, R. Erdmann, and J. Enderlein. Time-resolved fluorescence correlation spectroscopy. *Chemical Physics Letters*, 353(5-6):439–445, 2002.

[14] M. S. Bretscher. Asymmetrical lipid bilayer structure for biological membranes. *Nature New Biology*, 236(61):11–12, 1972.

[15] E. T. Castellana and P. S. Cremer. Solid supported lipid bilayers: From biophysical studies to sensor design. *Surface Science Reports*, 61(10):429–444, 2006.

[16] R. Chance, A. Prock, and R. Silbey. Lifetime of an emitting molecule near a partially reflecting surface. *The Journal of Chemical Physics*, 60(7):2744–2748, 1974.

[17] R. P. Cheng and W. F. DeGrado. De novo design of a monomeric helical β-peptide stabilized by electrostatic interactions. *Journal of the American Chemical Society*, 123(21):5162–5163, 2001.

[18] R. P. Cheng, S. H. Gellman, and W. F. DeGrado. β-peptides: from structure to function. *Chemical reviews*, 101(10):3219–3232, 2001.

[19] A. Chizhik, A. M. Chizhik, D. Khoptyar, S. Bär, A. J. Meixner, and J. Enderlein. Probing the radiative transition of single molecules with a tunable microresonator. *Nano letters*, 11(4):1700–1703, 2011.

[20] A. I. Chizhik, I. Gregor, B. Ernst, and J. Enderlein. Nanocavity-based determination of absolute values of photoluminescence quantum yields. *ChemPhysChem*, 14(3):505–513, 2013.

[21] A. I. Chizhik, J. Rother, I. Gregor, A. Janshoff, and J. Enderlein. Metal-induced energy transfer for live cell nanoscopy. *Nature Photonics*, 8(2):124–127, 2014.

[22] P. Cicuta, S. L. Keller, and S. L. Veatch. Diffusion of liquid domains in lipid bilayer membranes. *The journal of physical chemistry B*, 111(13):3328–3331, 2007.

[23] D. Correa, E. Medeiros, J. Oliveira, L. Paterno, and L. H. Mattoso. Nanostructured conjugated polymers in chemical sensors: synthesis, properties and applications. *Journal of nanoscience and nanotechnology*, 14(9):6509–6527, 2014.

[24] R. F. de Almeida, L. M. Loura, A. Fedorov, and M. Prieto. Lipid rafts have different sizes depending on membrane composition: a time-resolved fluorescence resonance energy transfer study. *Journal of molecular biology*, 346(4):1109–1120, 2005.

[25] C. De Los Santos, C.-W. Chang, M.-A. Mycek, and R. A. Cardullo. Frap, flim, and fret: Detection and analysis of cellular dynamics on a molecular scale using fluorescence microscopy. *Molecular reproduction and development*, 82(7-8):587–604, 2015.

[26] M. R. de Planque, B. B. Bonev, J. A. Demmers, D. V. Greathouse, R. E. Koeppe, F. Separovic, A. Watts, and J. A. Killian. Interfacial

anchor properties of tryptophan residues in transmembrane peptides can dominate over hydrophobic matching effects in peptide- lipid interactions. *Biochemistry*, 42(18):5341–5348, 2003.

[27] M. R. de Planque, J. A. Kruijtzer, R. M. Liskamp, D. Marsh, D. V. Greathouse, R. E. Koeppe II, B. de Kruijff, and J. A. Killian. Different membrane anchoring positions of tryptophan and lysine in synthetic transmembrane α-helical peptides. *Journal of Biological Chemistry*, 274(30):20839–20846, 1999.

[28] T. Dertinger, V. Pacheco, I. von der Hocht, R. Hartmann, I. Gregor, and J. Enderlein. Two-focus fluorescence correlation spectroscopy: A new tool for accurate and absolute diffusion measurements. *ChemPhysChem*, 8(3):433–443, 2007.

[29] T. Dertinger, I. von der Hocht, A. Benda, M. Hof, and J. Enderlein. Surface sticking and lateral diffusion of lipids in supported bilayers. *Langmuir*, 22(22):9339–9344, 2006.

[30] K. Drexhage. Influence of a dielectric interface on fluorescence decay time. *Journal of luminescence*, 1:693–701, 1970.

[31] K. Drexhage, H. Kuhn, and F. Schäfer. Variation of the fluorescence decay time of a molecule in front of a mirror. *Berichte der Bunsengesellschaft für physikalische Chemie*, 72(2):329–329, 1968.

[32] Y. Ebara and Y. Okahata. A kinetic study of concanavalin a binding to glycolipid monolayers by using a quartz-crystal microbalance. *Journal of the American Chemical Society*, 116(25):11209–11212, 1994.

[33] H. Eberhard, F. Diezmann, and O. Seitz. Dna as a molecular ruler: Interrogation of a tandem sh2 domain with self-assembled, bivalent dna–peptide complexes. *Angewandte Chemie*, 123(18):4232–4236, 2011.

[34] C. Eggeling, C. Ringemann, R. Medda, G. Schwarzmann, K. Sandhoff, S. Polyakova, V. N. Belov, B. Hein, C. Von Middendorff, A. Schönle, et al. Direct observation of the nanoscale dynamics of membrane lipids in a living cell. *Nature*, 457(7233):1159–1162, 2009.

[35] J. Eisenblätter and R. Winter. Pressure effects on the structure and phase behavior of dmpc-gramicidin lipid bilayers: a synchrotron saxs and 2h-nmr spectroscopy study. *Biophysical journal*, 90(3):956–966, 2006.

[36] J. Enderlein and M. Sauer. Optimal algorithm for single-molecule identification with time-correlated single-photon counting. *The Journal of Physical Chemistry A*, 105(1):48–53, 2001.

[37] A. Eremin, S. Baumgarten, K. Harth, R. Stannarius, Z. Nguyen, A. Goldfain, C. Park, J. E. Maclennan, M. Glaser, and N. Clark. Two-dimensional microrheology of freely suspended liquid crystal films. *Physical review letters*, 107(26):268301, 2011.

[38] A. Filippov, G. Orädd, and G. Lindblom. Influence of cholesterol and water content on phospholipid lateral diffusion in bilayers. *Langmuir*, 19(16):6397–6400, 2003.

[39] Flat-field correction. `https://en.wikipedia.org/wiki/Flat-field_correction/`.

[40] M. Forgac. Vacuolar atpases: rotary proton pumps in physiology and pathophysiology. *Nature reviews Molecular cell biology*, 8(11):917–929, 2007.

[41] J. Frackenpohl, P. I. Arvidsson, J. V. Schreiber, and D. Seebach. The outstanding biological stability of β-and γ-peptides toward proteolytic enzymes: an in vitro investigation with fifteen peptidases. *ChemBioChem*, 2(6):445–455, 2001.

[42] A. Gandhi, D. Lakshminarasimhan, Y. Sun, and H.-C. Guo. Structural insights into the molecular ruler mechanism of the endoplasmic reticulum aminopeptidase erap1. *Scientific reports*, 1(1):1–6, 2011.

[43] A. J. García-Sáez and P. Schwille. Single molecule techniques for the study of membrane proteins. *Applied microbiology and biotechnology*, 76(2):257–266, 2007.

[44] A. Ghosh, N. Karedla, J. C. Thiele, I. Gregor, and J. Enderlein. Fluorescence lifetime correlation spectroscopy: Basics and applications. *Methods*, 140:32–39, 2018.

[45] A. Ghosh, A. Sharma, A. I. Chizhik, S. Isbaner, D. Ruhlandt, R. Tsukanov, I. Gregor, N. Karedla, and J. Enderlein. Graphene-based metal-induced energy transfer for sub-nanometre optical localization. *Nature Photonics*, 13(12):860–865, 2019.

[46] D. Goswami, K. Gowrishankar, S. Bilgrami, S. Ghosh, R. Raghupathy, R. Chadda, R. Vishwakarma, M. Rao, and S. Mayor. Nanoclusters of gpi-anchored proteins are formed by cortical actin-driven activity. *Cell*, 135(6):1085–1097, 2008.

[47] J. T. Groves, N. Ulman, P. S. Cremer, and S. G. Boxer. Substrate-membrane interactions: Mechanisms for imposing patterns on a fluid bilayer membrane. *Langmuir*, 14(12):3347–3350, 1998.

[48] B. Gruenewald, W. Frisch, and J. F. Holzwarth. The kinetics of the formation of rotational isomers in the hydrophobic tail region of phospholipid bilayers. *Biochimica et Biophysica Acta (BBA)-Biomembranes*, 641(2):311–319, 1981.

[49] N. C. Hartman and J. T. Groves. Signaling clusters in the cell membrane. *Current opinion in cell biology*, 23(4):370–376, 2011.

[50] S. W. Hell and J. Wichmann. Breaking the diffraction resolution limit by stimulated emission: stimulated-emission-depletion fluorescence microscopy. *Optics letters*, 19(11):780–782, 1994.

[51] R. Henderson and P. N. T. Unwin. Three-dimensional model of purple membrane obtained by electron microscopy. *Nature*, 257(5521):28–32, 1975.

[52] S. T. Hess, T. P. Girirajan, and M. D. Mason. Ultra-high resolution imaging by fluorescence photoactivation localization microscopy. *Biophysical journal*, 91(11):4258–4272, 2006.

[53] M. Hetzer, S. Heinz, S. Grage, and T. Bayerl. Asymmetric molecular friction in supported phospholipid bilayers revealed by nmr measurements of lipid diffusion. *Langmuir*, 14(5):982–984, 1998.

[54] A. Honigmann, V. Mueller, S. W. Hell, and C. Eggeling. Sted microscopy detects and quantifies liquid phase separation in lipid membranes using a new far-red emitting fluorescent phosphoglycerolipid analogue. *Faraday Discussions*, 161:77–89, 2013.

[55] J. Hu, R. Lipowsky, and T. R. Weikl. Binding constants of membrane-anchored receptors and ligands depend strongly on the nanoscale roughness of membranes. *Proceedings of the National Academy of Sciences*, 110(38):15283–15288, 2013.

[56] B. Huang, W. Wang, M. Bates, and X. Zhuang. Three-dimensional super-resolution imaging by stochastic optical reconstruction microscopy. *Science*, 319(5864):810–813, 2008.

[57] S. Isbaner, N. Karedla, I. Kaminska, D. Ruhlandt, M. Raab, J. Bohlen, A. Chizhik, I. Gregor, P. Tinnefeld, J. Enderlein, et al. Axial colocalization of single molecules with nanometer accuracy using metal-induced energy transfer. *Nano letters*, 18(4):2616–2622, 2018.

[58] P. Jonsson, J. P. Beech, J. O. Tegenfeldt, and F. Hook. Mechanical behavior of a supported lipid bilayer under external shear forces. *Langmuir*, 25(11):6279–6286, 2009.

[59] B. Joseph, A. Sikora, E. Bordignon, G. Jeschke, D. S. Cafiso, and T. F. Prisner. Distance measurement on an endogenous membrane transporter in e. coli cells and native membranes using epr spectroscopy. *Angewandte Chemie*, 127(21):6294–6297, 2015.

[60] M. F. Juette, T. J. Gould, M. D. Lessard, M. J. Mlodzianoski, B. S. Nagpure, B. T. Bennett, S. T. Hess, and J. Bewersdorf. Three-dimensional sub–100 nm resolution fluorescence microscopy of thick samples. *Nature methods*, 5(6):527–529, 2008.

[61] R. Kaldenhoff, L. Kai, and N. Uehlein. Aquaporins and membrane diffusion of co2 in living organisms. *Biochimica et Biophysica Acta (BBA)-General Subjects*, 1840(5):1592–1595, 2014.

[62] P. Kapusta, R. Macháň, A. Benda, and M. Hof. Fluorescence lifetime correlation spectroscopy (flcs): concepts, applications and outlook. *International journal of molecular sciences*, 13(10):12890–12910, 2012.

[63] N. Karedla, A. I. Chizhik, I. Gregor, A. M. Chizhik, O. Schulz, and J. Enderlein. Single-molecule metal-induced energy transfer (smmiet): Resolving nanometer distances at the single-molecule level. *ChemPhysChem*, 15(4):705–711, 2014.

[64] N. Karedla, A. M. Chizhik, S. C. Stein, D. Ruhlandt, I. Gregor, A. I. Chizhik, and J. Enderlein. Three-dimensional single-molecule localization with nanometer accuracy using metal-induced energy transfer (miet) imaging. *The Journal of chemical physics*, 148(20):204201, 2018.

[65] J. A. Killian and G. von Heijne. How proteins adapt to a membrane–water interface. *Trends in biochemical sciences*, 25(9):429–434, 2000.

[66] M. Kloos, A. Sharma, J. Enderlein, and U. Diederichsen. Transmembrane β-peptide helices as molecular rulers at the membrane surface. *Journal of Peptide Science*, page e3355, 2021.

[67] U. Koert. β-peptides: Novel secondary structures take shape. *Angewandte Chemie International Edition in English*, 36(17):1836–1837, 1997.

[68] B. W. König, S. Krueger, W. Orts, C. F. Majkrzak, N. F. Berk, J. Silverton, and K. Gawrisch. Neutron reflectivity and atomic force microscopy studies of a lipid bilayer in water adsorbed to the surface of a silicon single crystal. *Langmuir*, 12(5):1343–1350, 1996.

[69] N. Kučerka, M.-P. Nieh, and J. Katsaras. Fluid phase lipid areas and bilayer thicknesses of commonly used phosphatidylcholines as a function of temperature. *Biochimica et Biophysica Acta (BBA)-Biomembranes*, 1808(11):2761–2771, 2011.

[70] N. Kučerka, S. Tristram-Nagle, and J. F. Nagle. Structure of fully hydrated fluid phase lipid bilayers with monounsaturated chains. *The Journal of membrane biology*, 208(3):193–202, 2006.

[71] H. Kuhn. Classical aspects of energy transfer in molecular systems. *The Journal of Chemical Physics*, 53(1):101–108, 1970.

[72] M. Kühner, R. Tampe, and E. Sackmann. Lipid mono-and bilayer supported on polymer films: composite polymer-lipid films on solid substrates. *Biophysical journal*, 67(1):217–226, 1994.

[73] B. Liang and L. K. Tamm. Nmr as a tool to investigate the structure, dynamics and function of membrane proteins. *Nature structural & molecular biology*, 23(6):468, 2016.

[74] A. M. Lieto, R. C. Cush, and N. L. Thompson. Ligand-receptor kinetics measured by total internal reflection with fluorescence correlation spectroscopy. *Biophysical journal*, 85(5):3294–3302, 2003.

[75] W.-C. Lin, C. D. Blanchette, and M. L. Longo. Fluid-phase chain unsaturation controlling domain microstructure and phase in ternary lipid bilayers containing galcer and cholesterol. *Biophysical journal*, 92(8):2831–2841, 2007.

[76] J. Lippert and W. Peticolas. Raman active vibrations in long-chain fatty acids and phospholipid sonicates. *Biochimica et Biophysica Acta (BBA)-Biomembranes*, 282:8–17, 1972.

[77] J. T. Littleton, J. Bai, B. Vyas, R. Desai, A. E. Baltus, M. B. Garment, S. D. Carlson, B. Ganetzky, and E. R. Chapman. synaptotagmin mutants reveal essential functions for the c2b domain in ca2+-triggered fusion and recycling of synaptic vesicles in vivo. *Journal of Neuroscience*, 21(5):1421–1433, 2001.

[78] L. Loura and M. J. Prieto. Fret in membrane biophysics: An overview. *Frontiers in physiology*, 2:82, 2011.

[79] W. Lukosz and R. Kunz. Fluorescence lifetime of magnetic and electric dipoles near a dielectric interface. *Optics Communications*, 20(2):195–199, 1977.

[80] W. Lukosz and R. Kunz. Light emission by magnetic and electric dipoles close to a plane interface. i. total radiated power. *JOSA*, 67(12):1607–1615, 1977.

[81] S. E. Lux. Anatomy of the red cell membrane skeleton: unanswered questions. *Blood*, 127(2):187–199, 2016.

[82] R. Macháň and M. Hof. Lipid diffusion in planar membranes investigated by fluorescence correlation spectroscopy. *Biochimica et Biophysica Acta (BBA)-Biomembranes*, 1798(7):1377–1391, 2010.

[83] D. Magde, E. Elson, and W. W. Webb. Thermodynamic fluctuations in a reacting system-measurement by fluorescence correlation spectroscopy. *Physical review letters*, 29(11):705, 1972.

[84] M. D. Mager, B. Almquist, and N. A. Melosh. Formation and characterization of fluid lipid bilayers on alumina. *Langmuir*, 24(22):12734–12737, 2008.

[85] R. Mahfoud, A. Manis, B. Binnington, C. Ackerley, and C. A. Lingwood. A major fraction of glycosphingolipids in model and cellular cholesterol-containing membranes is undetectable by their binding proteins. *Journal of Biological Chemistry*, 285(46):36049–36059, 2010.

[86] G. Majer and J. P. Melchior. Characterization of the fluorescence correlation spectroscopy (fcs) standard rhodamine 6g and calibration of its diffusion coefficient in aqueous solutions. *The Journal of chemical physics*, 140(9):094201, 2014.

[87] D. Marquardt, F. A. Heberle, D. V. Greathouse, R. E. Koeppe, R. F. Standaert, B. J. Van Oosten, T. A. Harroun, J. J. Kinnun, J. A. Williams, S. R. Wassall, et al. Lipid bilayer thickness determines cholesterol's location in model membranes. *Soft Matter*, 12(47):9417–9428, 2016.

[88] R. S. Mathew-Fenn, R. Das, J. A. Silverman, P. A. Walker, and P. A. Harbury. A molecular ruler for measuring quantitative distance distributions. *PloS one*, 3(10):e3229, 2008.

[89] A. Matysik and R. S. Kraut. Preparation of mica supported lipid bilayers for high resolution optical microscopy imaging. *JoVE (Journal of Visualized Experiments)*, 88(88):e52054, 2014.

[90] H. M. McConnell and R. D. Kornberg. Inside-outside transitions of phospholipids in vesicle membranes. *Biochemistry*, 10(7):1111–1120, 1971.

[91] R. J. Moerland and J. P. Hoogenboom. Subnanometer-accuracy optical distance ruler based on fluorescence quenching by transparent conductors. *Optica*, 3(2):112–117, 2016.

[92] V. Mueller, C. Ringemann, A. Honigmann, G. Schwarzmann, R. Medda, M. Leutenegger, S. Polyakova, V. Belov, S. Hell, and C. Eggeling. Sted nanoscopy reveals molecular details of cholesterol- and cytoskeleton-modulated lipid interactions in living cells. *Biophysical journal*, 101(7):1651–1660, 2011.

[93] H. M. Munnelly, D. A. Roess, W. F. Wade, and B. G. Barisas. Interferometric fringe fluorescence photobleaching recovery interrogates entire cell surfaces. *Biophysical journal*, 75(2):1131–1138, 1998.

[94] J. F. Nagle and S. Tristram-Nagle. Structure of lipid bilayers. *Biochimica et Biophysica Acta (BBA)-Reviews on Biomembranes*, 1469(3):159–195, 2000.

[95] Z. H. Nguyen, M. Atkinson, C. S. Park, J. Maclennan, M. Glaser, and N. Clark. Crossover between 2d and 3d fluid dynamics in the diffusion of islands in ultrathin freely suspended smectic films. *Physical review letters*, 105(26):268304, 2010.

[96] K. S. Novoselov, A. K. Geim, S. V. Morozov, D. Jiang, Y. Zhang, S. V. Dubonos, I. V. Grigorieva, and A. A. Firsov. Electric field effect in atomically thin carbon films. *science*, 306(5696):666–669, 2004.

[97] A. Olivera-Couto, V. Salzman, M. Mailhos, M. A. Digman, E. Gratton, and P. S. Aguilar. Eisosomes are dynamic plasma membrane domains showing pil1-lsp1 heteroligomer binding equilibrium. *Biophysical journal*, 108(7):1633–1644, 2015.

[98] T. Otosu and S. Yamaguchi. Quantifying the diffusion of lipids in the proximal/distal leaflets of a supported lipid bilayer by two-dimensional fluorescence lifetime correlation spectroscopy. *The Journal of Physical Chemistry B*, 122(45):10315–10319, 2018.

[99] J. P. Overington, B. Al-Lazikani, and A. L. Hopkins. How many drug targets are there? *Nature reviews Drug discovery*, 5(12):993–996, 2006.

[100] D. M. Pahlke and U. Diederichsen. Synthesis and characterization of β-peptide helices as transmembrane domains in lipid model membranes. *Journal of Peptide Science*, 22(10):636–641, 2016.

[101] E. H. Pap, P. I. Bastiaens, J.-W. Borst, P. A. Van den Berg, A. Van Hoek, G. T. Snoek, K. W. Wirtz, and A. J. Visser. Quantitation of the interaction of protein kinase c with diacylglycerol and phosphoinositides by time-resolved detection of resonance energy transfer. *Biochemistry*, 32(48):13310–13317, 1993.

[102] H. B. Park, Y. C. Lam, J. P. Gaffney, J. C. Weaver, S. R. Krivoshik, R. Hamchand, V. Pieribone, D. F. Gruber, and J. M. Crawford. Bright green biofluorescence in sharks derives from bromo-kynurenine metabolism. *Iscience*, 19:1291–1336, 2019.

[103] D. Patra, I. Gregor, and J. Enderlein. Image analysis of defocused single-molecule images for three-dimensional molecule orientation studies. *The Journal of Physical Chemistry A*, 108(33):6836–6841, 2004.

[104] S. R. P. Pavani, M. A. Thompson, J. S. Biteen, S. J. Lord, N. Liu, R. J. Twieg, R. Piestun, and W. E. Moerner. Three-dimensional, single-molecule fluorescence imaging beyond the diffraction limit by using a double-helix point spread function. *Proceedings of the National Academy of Sciences*, 106(9):2995–2999, 2009.

[105] Z. Petrášek and P. Schwille. Precise measurement of diffusion coefficients using scanning fluorescence correlation spectroscopy. *Biophysical journal*, 94(4):1437–1448, 2008.

[106] E. P. Petrov and P. Schwille. Translational diffusion in lipid membranes beyond the saffman-delbrück approximation. *Biophysical journal*, 94(5):L41–L43, 2008.

[107] M. Przybylo, J. Sýkora, J. Humpolícková, A. Benda, A. Zan, and M. Hof. Lipid diffusion in giant unilamellar vesicles is more than 2 times faster than in supported phospholipid bilayers under identical conditions. *Langmuir*, 22(22):9096–9099, 2006.

[108] M. Quick and J. A. Javitch. Monitoring the function of membrane transport proteins in detergent-solubilized form. *Proceedings of the National Academy of Sciences*, 104(9):3603–3608, 2007.

[109] S. Ramadurai, A. Holt, V. Krasnikov, G. van den Bogaart, J. A. Killian, and B. Poolman. Lateral diffusion of membrane proteins. *Journal of the American Chemical Society*, 131(35):12650–12656, 2009.

[110] J. Ries, S. Chiantia, and P. Schwille. Accurate determination of membrane dynamics with line-scan fcs. *Biophysical journal*, 96(5):1999–2008, 2009.

[111] R. Rigler, Ü. Mets, J. Widengren, and P. Kask. Fluorescence correlation spectroscopy with high count rate and low background: analysis of translational diffusion. *European Biophysics Journal*, 22(3):169–175, 1993.

[112] J. Rohrbough and K. Broadie. Lipid regulation of the synaptic vesicle cycle. *Nature Reviews Neuroscience*, 6(2):139–150, 2005.

[113] U. Rost, C. Steinem, and U. Diederichsen. β-glutamine-mediated self-association of transmembrane β-peptides within lipid bilayers. *Chemical science*, 7(9):5900–5907, 2016.

[114] U. Rost, Y. Xu, T. Salditt, and U. Diederichsen. Heavy-atom labeled transmembrane β-peptides: Synthesis, cd-spectroscopy, and x-ray diffraction studies in model lipid multilayer. *ChemPhysChem*, 17(16):2525–2534, 2016.

[115] J. E. Rothman and J. Lenard. Membrane asymmetry. *Science*, 195(4280):743–753, 1977.

[116] R. Roy, S. Hohng, and T. Ha. A practical guide to single-molecule fret. *Nature methods*, 5(6):507–516, 2008.

[117] M. J. Rust, M. Bates, and X. Zhuang. Sub-diffraction-limit imaging by stochastic optical reconstruction microscopy (storm). *Nature methods*, 3(10):793–796, 2006.

[118] P. Saffman and M. Delbrück. Brownian motion in biological membranes. *Proceedings of the National Academy of Sciences*, 72(8):3111–3113, 1975.

[119] J. Sankaran and T. Wohland. Fluorescence strategies for mapping cell membrane dynamics and structures. *APL bioengineering*, 4(2):020901, 2020.

[120] M. J. Saxton and K. Jacobson. Single-particle tracking: applications to membrane dynamics. *Annual review of biophysics and biomolecular structure*, 26(1):373–399, 1997.

[121] R. L. Schoch, I. Barel, F. L. Brown, and G. Haran. Lipid diffusion in the distal and proximal leaflets of supported lipid bilayer membranes studied by single particle tracking. *The Journal of chemical physics*, 148(12):123333, 2018.

[122] G. J. Schütz, H. Schindler, and T. Schmidt. Single-molecule microscopy on model membranes reveals anomalous diffusion. *Biophysical journal*, 73(2):1073–1080, 1997.

[123] C. Scomparin, S. Lecuyer, M. Ferreira, T. Charitat, and B. Tinland. Diffusion in supported lipid bilayers: Influence of substrate and preparation technique on the internal dynamics. *The European Physical Journal E*, 28(2):211–220, 2009.

[124] E. Sezgin, I. Levental, M. Grzybek, G. Schwarzmann, V. Mueller, A. Honigmann, V. N. Belov, C. Eggeling, Ü. Coskun, K. Simons, et al. Partitioning, diffusion, and ligand binding of raft lipid analogs in model and cellular plasma membranes. *Biochimica et Biophysica Acta (BBA)-Biomembranes*, 1818(7):1777–1784, 2012.

[125] E. Sezgin, F. Schneider, S. Galiani, I. Urbančič, D. Waithe, B. C. Lagerholm, and C. Eggeling. Measuring nanoscale diffusion dynamics in cellular membranes with super-resolution sted–fcs. *Nature protocols*, 14(4):1054–1083, 2019.

[126] A. Sharonov, R. Bandichhor, K. Burgess, A. D. Petrescu, F. Schroeder, A. B. Kier, and R. M. Hochstrasser. Lipid diffusion from single

molecules of a labeled protein undergoing dynamic association with giant unilamellar vesicles and supported bilayers. *Langmuir*, 24(3):844–850, 2008.

[127] A. Sharonov and R. M. Hochstrasser. Wide-field subdiffraction imaging by accumulated binding of diffusing probes. *Proceedings of the National Academy of Sciences*, 103(50):18911–18916, 2006.

[128] Q. She, R. Wang, A. G. Fane, and C. Y. Tang. Membrane fouling in osmotically driven membrane processes: A review. *Journal of Membrane Science*, 499:201–233, 2016.

[129] S. Shenoy, R. Moldovan, J. Fitzpatrick, D. J. Vanderah, M. Deserno, and M. Lösche. In-plane homogeneity and lipid dynamics in tethered bilayer lipid membranes (tblms). *Soft matter*, 6(6):1263–1274, 2010.

[130] G. Shtengel, J. A. Galbraith, C. G. Galbraith, J. Lippincott-Schwartz, J. M. Gillette, S. Manley, R. Sougrat, C. M. Waterman, P. Kanchanawong, M. W. Davidson, et al. Interferometric fluorescent superresolution microscopy resolves 3d cellular ultrastructure. *Proceedings of the National Academy of Sciences*, 106(9):3125–3130, 2009.

[131] J. Sibold, K. Kettelhoit, L. Vuong, F. Liu, D. B. Werz, and C. Steinem. Synthesis of gb3 glycosphingolipids with labeled head groups: Distribution in phase-separated giant unilamellar vesicles. *Angewandte Chemie International Edition*, 58(49):17805–17813, 2019.

[132] K. Simons and E. Ikonen. Functional rafts in cell membranes. *nature*, 387(6633):569–572, 1997.

[133] S. J. Singer and G. L. Nicolson. The fluid mosaic model of the structure of cell membranes. *Science*, 175(4023):720–731, 1972.

[134] A. S. Smith, R. B. Nowak, S. Zhou, M. Giannetto, D. S. Gokhin, J. Papoin, I. C. Ghiran, L. Blanc, J. Wan, and V. M. Fowler. Myosin iia interacts with the spectrin-actin membrane skeleton to control red blood cell membrane curvature and deformability. *Proceedings of the National Academy of Sciences*, 115(19):E4377–E4385, 2018.

[135] C. Sönnichsen, B. M. Reinhard, J. Liphardt, and A. P. Alivisatos. A molecular ruler based on plasmon coupling of single gold and silver nanoparticles. *Nature biotechnology*, 23(6):741–745, 2005.

[136] B. L. Sprague and J. G. McNally. Frap analysis of binding: proper and fitting. *Trends in cell biology*, 15(2):84–91, 2005.

[137] S. C. Stein and J. Thiart. Trackntrace: A simple and extendable open-source framework for developing single-molecule localization and tracking algorithms. *Scientific reports*, 6(1):1–7, 2016.

[138] S. R. Tabaei, J. J. Gillissen, and N.-J. Cho. Probing membrane viscosity and interleaflet friction of supported lipid bilayers by tracking electrostatically adsorbed, nano-sized vesicles. *Small*, 12(46):6338–6344, 2016.

[139] K.-H. Tews, O. Inacker, and H. Kuhn. Variation of the luminescence lifetime of a molecule near an interface between differently polarizable dielectrics. *Nature*, 228(5268):276–278, 1970.

[140] A. Tian, C. Johnson, W. Wang, and T. Baumgart. Line tension at fluid membrane domain boundaries measured by micropipette aspiration. *Physical review letters*, 98(20):208102, 2007.

[141] H. Träuble and H. Eibl. Electrostatic effects on lipid phase transitions: membrane structure and ionic environment. *Proceedings of the National Academy of Sciences*, 71(1):214–219, 1974.

[142] S. Tristram-Nagle, H. I. Petrache, and J. F. Nagle. Structure and interactions of fully hydrated dioleoylphosphatidylcholine bilayers. *Biophysical journal*, 75(2):917–925, 1998.

[143] S. Van de Linde, A. Löschberger, T. Klein, M. Heidbreder, S. Wolter, M. Heilemann, and M. Sauer. Direct stochastic optical reconstruction microscopy with standard fluorescent probes. *Nature protocols*, 6(7):991, 2011.

[144] G. van Meer and A. I. de Kroon. Lipid map of the mammalian cell. *Journal of cell science*, 124(1):5–8, 2011.

[145] G. Van Meer, D. R. Voelker, and G. W. Feigenson. Membrane lipids: where they are and how they behave. *Nature reviews Molecular cell biology*, 9(2):112–124, 2008.

[146] A. Varki, R. D. Cummings, J. D. Esko, P. Stanley, G. W. Hart, M. Aebi, A. G. Darvill, T. Kinoshita, N. H. Packer, J. H. Prestegard, et al. Essentials of glycobiology. In *Essentials of Glycobiology [internet]*. Cold Spring Harbor Laboratory Press, 2015.

[147] G. A. Venkatesan, G. J. Taylor, C. M. Basham, N. G. Brady, C. P. Collier, and S. A. Sarles. Evaporation-induced monolayer compression improves droplet interface bilayer formation using unsaturated lipids. *Biomicrofluidics*, 12(2):024101, 2018.

[148] P. R. Wallace. The band theory of graphite. *Physical review*, 71(9):622, 1947.

[149] A. C. Woodka, P. D. Butler, L. Porcar, B. Farago, and M. Nagao. Lipid bilayers and membrane dynamics: insight into thickness fluctuations. *Physical review letters*, 109(5):058102, 2012.

[150] L. Zhang and S. Granick. Lipid diffusion compared in outer and inner leaflets of planar supported bilayers, 2005.

List of Figures

Glossary of Acronyms

fPALM Fluorescence photoactivation localization microscopy

STED stimulated emission depletion microscopy

STORM Stochastic optical reconstruction microscopy

FRET Förster resonance energy transfer

SAXS Small-angle X-ray scattering

NMR Nuclear magnetic resonance

SLB Supported lipid bilayer

MIET Metal-induced energy transfer

FLCS Fluorescence lifetime correlation spectroscopy

FCS Fluorescence correlation spectroscopy

AFM Atomic force microscopy

QCM Quartz crystal microbalance

SPT Single particle tracking

MSD mean-squared displacement

FRAP fluorescence recovery after photobleaching

2fFCS Dual Focus Fluorescence Correlation Spectroscopy

ACF Autocorrelation Function

CCF Cross-Correlation Function

MDF molecule detection function

TCSPC Time correlated single photon counting

TTTR Time-Tagged Time-Resolved

GIET Graphene-induced energy transfer

ITO Indium tin oxide

SMLM single-molecule localization microscopy

FLIM Fluorescence Lifetime Imaging

DOPC 1,2-dioleoyl- sn - glycero- 3- phosphocholine

POPC 1- palmitoyl- 2- oleoyl- sn - glycero- 3- phosphocholine

DLPC 1,2-dilauroyl-sn-glycero-3-phosphocholine

DPPE 1,2-dihexadecanoyl-sn-glycero-3-phosphoethanolamine

DLPE 1,2- dilauroyl- sn- glycero- 3- phosphoethanolamine

GUV Gaint unilamellar vesicle

SUV Small unilamellar vesicle

PEG Polyethylene glycol

PBS Phosphate buffered saline

SPAD Single-photon avalanche diode

PSF Point spread function

Gb3 Globotriaosylceramide